Marek, Przemyslaw Lech (2008) *Design, optimization and flight testing of a micro air vehicle.* MSc(R) thesis.

http://theses.gla.ac.uk/259/

Design, Optimization and Flight Testing
of a Micro Air Vehicle

by

Przemyslaw Marek

A thesis submitted to the Faculty of Engineering,

University of Glasgow in

fulfillment of the requirements of

the degree of Master of Science

DEPARTMENT OF AEROSPACE ENGINEERING
Supervisor: Dr. Ladislav Smrcek
December 2007

Acknowledgements

Abstract

Micro Air Vehicles (MAVs) are a new type of aircraft maturing every year. The first mission-capable MAVs are already available on the market. Similarly to larger UAVs, MAVs may be used in a variety of applications, both military and civilian, such as situational awareness, reconnaissance, data relay, air sampling etc. This study describes the development of a method for rapid design and optimization based on some basic preliminary design parameters.

Low aspect ratio (LAR) wing theory and experimental data by Mueller and Torres have been used to analytically predict the performance of the MAV. This has also been validated by the author's wind tunnel experiments, also described in this thesis. The results of the wind tunnel experiments are presented. Performance of the propulsion system (motor, propeller, battery, speed controller) was evaluated using other commercially available tools.

The design optimization concerns the wing geometry under certain constraints applied by the user. The design optimization code, which is based on Genetic Algorithms, was written in MATLAB.

As a conclusion to the project, a prototype was built and successfully test flown, which proved the feasibility of the developed method. A detailed description of the manufacture and testing of the prototype is also included in this thesis.

Table of contents

List of Figures

List of Tables

Nomenclature

AC	Aerodynamic Centre
a_d	Depron sheet weight [kg/m^2]
AR	Wing Aspect Ratio
b	Wingspan
C	Wind tunnel cross-sectional area
c	Wing chord
C_D	Aircraft moment coefficient
C_{D0}	Zero-lift drag
C_{Dfin}	Fin drag coefficient
C_{Dfuse}	Fuselage drag coefficient
CG	Center of Gravity
C_L	Aircraft lift coefficient
C_{Lmax}	Maximum lift coefficient
$C_{M\,0.25}$	Aircraft pitching moment about the quarter-chord (MAC)
c_{root}	Root wing chord
D	Drag
DARPA	Defense Advanced Research Projects Agency
F	Model frontal area
f_h	Fuselage height
f_w	Fuselage width
F_x	Tangential force
F_z	Normal force
GA	Genetic Algorithm
GPS	Global Positioning System
IR	Infrared
K	Wind tunnel constant (Anatomy Wind Tunnel: K=1.237)
L	Lift
LAR	Low Aspect Ratio
LiPo	Lithium-Polymer (battery)
LLT	Lifting Line Theory
l_v	Vertical tail arm

$M_{0.25}$	Pitching moment around the quarter-chord (MAC)
MAC, $\overline{c}$	Mean Aerodynamic Chord
MAV	Micro Aerial Vehicle
m_{tow}	take-off weight
M_y	Moment around the load cell origin
p_s	Static pressure in the settling chamber of the wind tunnel
p_w	Static pressure in the test section of the wind tunnel
q_w	Dynamic pressure in the test section of the wind tunnel
R	Gas constant, for air: R=285 [J/(kg*K)]
Re	Reynolds Number (based on MAC)
S	Wing Area
S_{fin}	Fin surface area
S_{fuse}	Fuselage cross-section area
T	Ambient temperature [K]
T_{req}	Thrust required
U_∞	Freestream velocity in the wind tunnel
U_c	Corrected velocity in the wind tunnel
UAV	Unmanned Air Vehicle
V	Aircraft speed
V_{cruise}	Design cruise speed
VLM	Vortex Lattice Method
V_{min}	Calculated stall speed
V_{opt}	Calculated optimum (max. L/D) speed
V_{stall}	Design stall speed limit
α	Angle Of Attack
α_{stall}	Stall angle of attack
ε_s	Solid blockage correction
ε_t	Total blockage correction
ε_w	Wake blockage correction
ν	Air kinematic viscosity
ρ	Air Density

All dimensions are in mm unless specified.

1. Introduction

1.1 MAVs overview

Micro Aerial Vehicles (MAVs) emerged in the early 1990's and have been evolving rapidly ever since [1]. Due to their size they posed some new and quite unique challenges in the areas of aerodynamics, equipment integration and the design approach itself. As systems, they are also relatively cheap compared to normal sized aircraft and therefore attracted a great deal of attention not only from companies but also from universities around the world [2, 3, 4, 5].

MAVs are being built primarily for close reconnaissance missions, but as market research has shown [6] there are also other possible applications, both military and civilian, such as situational awareness, data relay or air sampling. As in the case of full scale UAVs, many new tasks will arise once MAVs become more popular and their capabilities are further explored. Some very futuristic concepts such as swarming of hundreds of MAVs which can relay information within their group and provide the user with large-area reconnaissance data are also currently under development. Some other ideas, which might seem even more futuristic include vehicles flying to the target as a swarm of MAVs, they then join once they have arrived at the spot into one larger vehicle to fulfill the mission. Theoretically, traveling in the form of a swarm is supposed to make them less susceptible to enemy fire. These kinds of ideas were actually proposed a long time ago by futurologists.[1]

As with any relatively new invention, MAVs are still finding their way into many new applications. The development of new, miniaturized electronic equipment such as video cameras, GPS receivers, autopilots etc. has been playing a major role in MAV progress as well. While there are many MAVs developed nowadays, only a few are really suitable and ready products for real-life operations [7, 8]. Existing vehicles are built usually as technology demonstrators or experimental planes which sometimes incorporate various performance-enhancing features [2, 3, 9] rather than designs aiming at a particular customer. Some of these concepts

---

[1] S. Lem, "Biblioteka XXI wieku" ("Library of 21st Century"), Wydawnictwo Literackie, 2003, ISBN 83-08-03531-0

have shown very promising results and may be worth further investigation in development of new designs. Nonetheless, interest in MAVs seems to be building up and most probably they will be a commonly used tool for the military within the next decade. Sooner or later, civilian applications will also emerge. One important factor which might push MAVs into use before mini UAVs in this sector is their size and weight – in the case of a malfunction their crash will not cause much damage on the ground, which seems to be one of the most important concerns for operations in the urban environment.

The number of new mission opportunities emerging for MAVs poses some new challenges in terms of their design. Sometimes changes of the mission profile which might not seem particularly major may call for a totally new aircraft or at least a serious re-design of the existing plane. This trend is likely to be more important in the near future with more extensive use of MAVs. Therefore a need for optimization methods is likely to emerge.

The main objective of this study was to present a design and optimization method for MAVs. It was assumed that the method should be robust and stable, allowing easy modifications in the future if needed. MAVs seem to be very 'adaptable' platforms – their airframe is very easy to re-design. Because of relatively small in-flight stresses posed on the airframe, once the pieces of equipment are integrated it is very easy to change the geometry of the wings with no need for major changes in the other elements of the structure. Slight changes of a mission profile might call for a slightly different battery size or motor characteristics but nevertheless this is a relatively easy task, compared to full-size aircraft where the structure is designed for tackling in-flight loads rather than handling and landing stresses.

1.2 Aim of the project

The aim of the project was to develop and demonstrate a practical method of designing an MAV. The aircraft described in this study is of a fixed wing design. A fixed wing aircraft is suitable for the above-mentioned type of mission and moreover, it is usually superior in endurance if compared to rotorcraft and ornithopters [5, 10].

The MAV was initially designed according to rules for the outdoor mission at the US-European Micro Air Vehicle Competition MAV07 [11]. Because of the lack of experimental data on some of the aerodynamic aspects of MAVs, wind tunnel tests have been carried out in the Anatomy Wind Tunnel at the Aerospace Department at The University of Glasgow, and results are presented in this thesis. Next, a code for MAV optimization has been developed using MATLAB. Finally, flight tests have been carried out to validate project's concepts. The design process is depicted as a flow chart in Fig. 1.
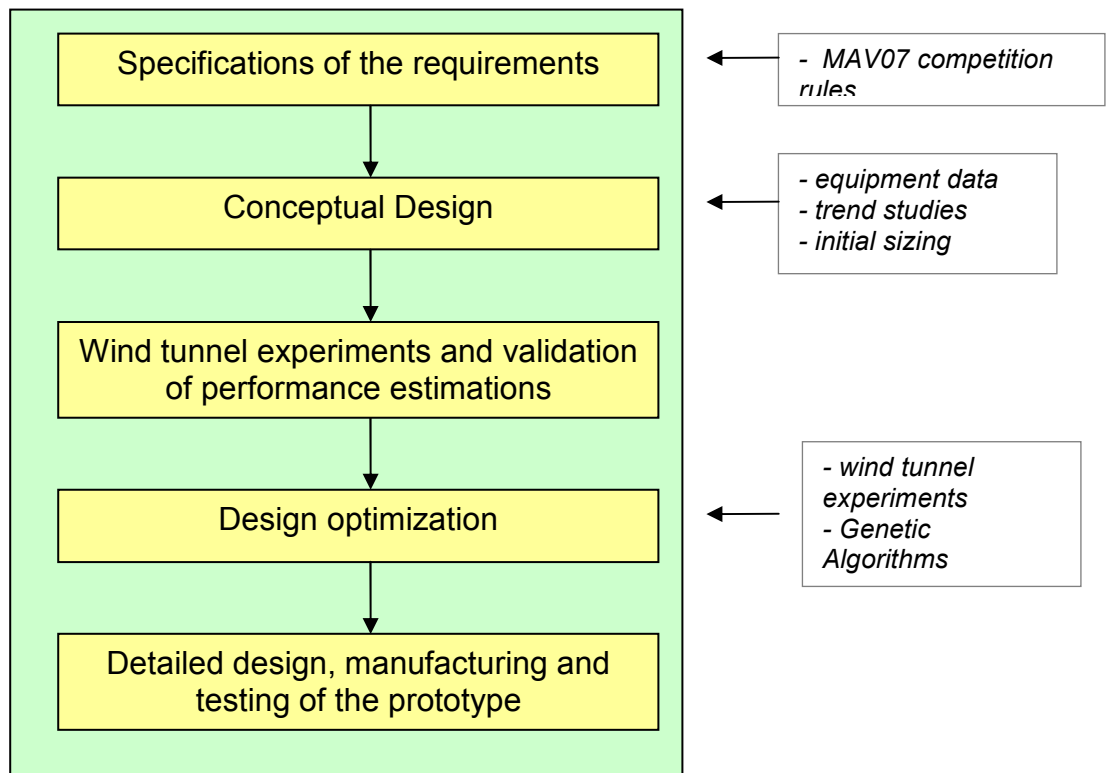
Figure 1 - Design process flow chart

2. Specification of the requirements and the mission profile

2.1 General requirements

Formulation of the mission profile and requirements is the first and one of the most important aspects of the aircraft design process. While a big part of it usually comes from the customer who specifies what is expected from the aircraft, some features must be decided at an early stage by the designer as they may later have a decisive role when it comes to making some design trade-offs. In this work, the requirements of the outdoor mission from the MAV07 [10] have been selected as the basis for the mission profile. The requirements for the vehicle are maximum dimensions of 500mm and a maximum take-off weight of 500g. The mission requirements are to fly within a 1 km radius of the launch spot and identify predefined targets at the given spot, find targets in a certain area and transmit their position using GPS coordinates, fly through an 'urban canyon' (two 15m arches made of balloons), drop a sensor dummy (a small ball) in a predefined spot and return to the launch point, see Fig. 2.
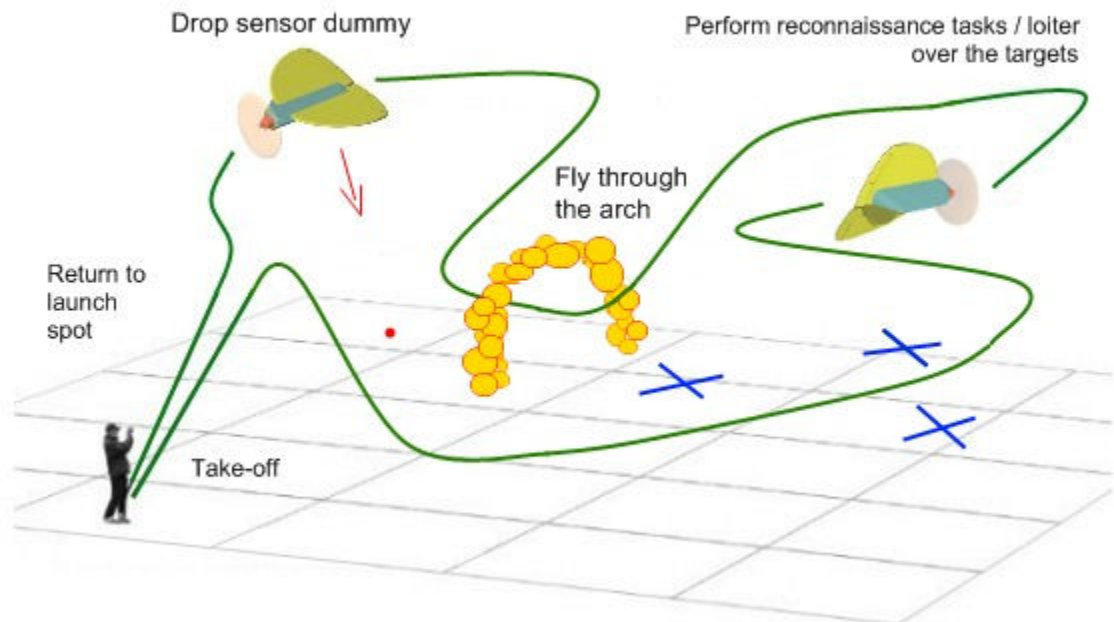
Figure 2 - Mission scheme

Apart from the mission considerations, a specification of what actually is a Micro Air Vehicle is formulated at this point, too. There have been some attempts to

categorize MAVs by their size and weight. In the early 90's DARPA (Defense Advanced Research Projects Agency) specified the maximum dimension for MAVs should not exceed 152mm (6") and the weight must be no more than 112g (4oz). Nevertheless many larger UAVs today are still referred to as MAVs. The 500mm/500g requirement at the MAV07 Competition is a good illustration that the border between micro and mini UAVs is largely subjective. In this study, MAV is defined as an unmanned aircraft small enough to be carried with all the equipment needed to control it by one person, thus making it a truly 'personal tool'.

The name of the designed MAV has been chosen to be 'BumbleBee' as the result of a comment by a fellow student on the appearance of the micro aircraft.

2.2 Flight parameters

Cruise and stall speeds are the next important set of parameters which must be chosen during the mission specification. Cruising speed will also determine the endurance which is needed to complete the mission. Cruise speed must also be sufficient to fly in atmospheric turbulence and it can not be too high since the small propulsion systems used on MAVs are usually not suitable for flying at high speeds.

In this case, cruising speed of 16m/s (~58 km/h) has been selected. Compared to some MAV designs [1, 2, 4] it may seem rather high, but if we take the atmospheric winds into account [12] it becomes clear that the cruise speed must be well above 10m/s so that winds do not restrict the operations of the MAV to good weather only. In fact, 5-10m/s winds are pretty common and in case of a rather slow aircraft it might happen that the plane is actually too slow to fly forwards. Stalling speed is selected mainly on the basis of whether the vehicle will be hand-launched or not. In this case, because portability was a major factor, a requirement for stall speed not higher than 8m/s has been made so that the aircraft can be hand-launched and will not require any special equipment such as a catapult.

Once the cruise speed is specified, vehicle endurance can be calculated. A simple mission case was to fly to the edge of the operating area, loiter and perform

mission tasks and then fly back to the launch spot. With cruise speed of 16m/s it takes one minute to fly a 1km distance, then approximately 15 minutes to perform the tasks and 1 minute to fly back. To allow for some extra time (in case of increased wind, reduced battery power at the end of the flight etc.), the design endurance was set to be 20 minutes.

Another important point was to select the way in which BumbleBee would be controlled. Usually MAVs are controlled in one of 3 ways:

- Fully autonomous
- Pilot-through-vision
- Visual contact

In this case the choice was pretty straightforward, mainly due to limited budget which did not allow for the purchase of an autopilot to make the MAV fully autonomous. Visual contact was also ruled out because it is hard to see the plane if it is more than 100m away and this would rule out operations at 1km. The only viable option was the pilot-through-vision system, which means direct control with the pilot looking at the live video transmitted from the MAV. Since this method somewhat limits the pilot's perception due to the limited field of view, a simple infrared (IR) stabilization system was to be used to reduce pilot workload.

2.3 Payload

The payload for the reconnaissance mission is a video camera for target recognition and a GPS receiver for gathering GPS data, which is to be transmitted live to the ground for determining target position. A single servomechanism for the ball dropping operation was also to be incorporated into the airframe.

All the basic design requirements are outlined in Table 1.

Table 1 - MAV design requirements

Max dimension	500 mm
Max weight	500 g
Stall speed V_{min}	8 m/s
Cruise speed V_{cruise}	16 m/s
Endurance	20 minutes
Mission radius	1 km
Control	Pilot-through-vision
Payload	Video camera, GPS receiver, video & GPS data transmitter, IR stabilization system

3. Conceptual design

The conceptual design starts usually with brainstorming many ideas, looking through the existing design and iterating the design a number of times. It is sometimes re-done even after setting the initial configurations should some unexpected problems in testing arise.

3.1 Trend studies

There are quite a few MAVs designed for reconnaissance missions and they come in whole variety of configurations, sizes and capabilities. They are outlined in Table 2 and shown in Figs. 3-12.

Table 2 - Outline of MAV designs

		Black Widow	WASP	HoverFly C	Carolo 40	Carolo 50	Dragon Slayer
Wingspan	b [mm]	152	330	~200	400	490	330
Length	l [mm]	152	-	-	-	-	-
Wing area	S [m²]	0.0195	-	-	-	-	-
Weight	W [g]	80	170	180	350	550	300
Endurance	t [min]	30	107	13.2	45	-	35
Airspeed	V [m/s]	13.4	-	15-20	20	15-20	18-40
configuration		flying wing	flying wing	flying wing	canard	classical	flying wing
planform		modified rectangular	tapered	rectangular	semi-elliptical	rectangular , T-tail	delta

		WUT MAV	MicroSTAR	Mosquito 1	BYU MAV	University of Arizona - Dragonfly	University of Arizona – var. camber
Wingspan	b [mm]	450	152	330	120	300	230
Length	l [mm]	450	-	-	-	-	-
Wing area	S [m²]	0.1	0.027	~0.086	-	~0.071	0.0387
Weight	W [g]	~200	110	250	32	-	73
Endurance	t [min]	-	25	40	-	30	-
Airspeed	V [m/s]	~10	13.4-15.6	15-20	14	25 max	10 max
configuration		flying wing	flying wing	flying wing	flying wing	flying wing	flying wing
planform		clipped delta with LEX	delta with clipped tips	inverse Zimmerman	modified rectangular	Zimmerman	mod. Zimmerman
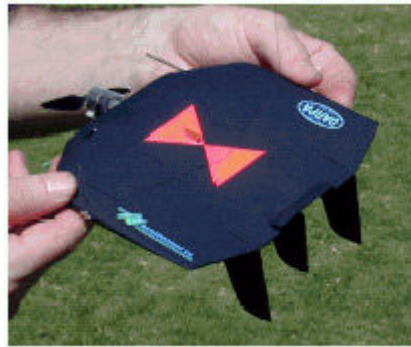
Figure 3 - Black Widow MAV (Aerovironment Inc.)

Figure 4 - WASP MAV (Aerovironment Inc.)
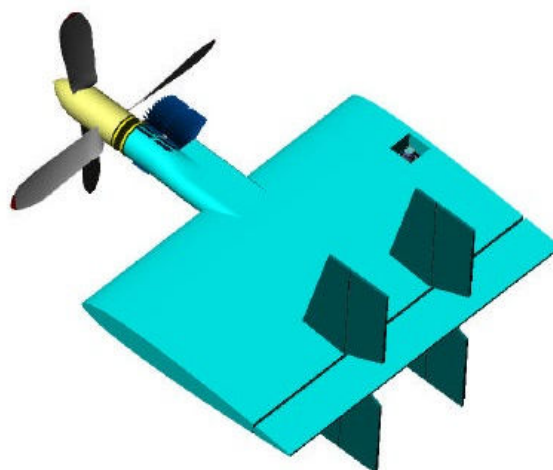
Figure 5 - HoverFly C (Aerovironment Inc.)

Figure 6 - Carolo MAV built at the Technical University of Braunschweig
(http://hp.kairaven.de/bigb/mav.html)
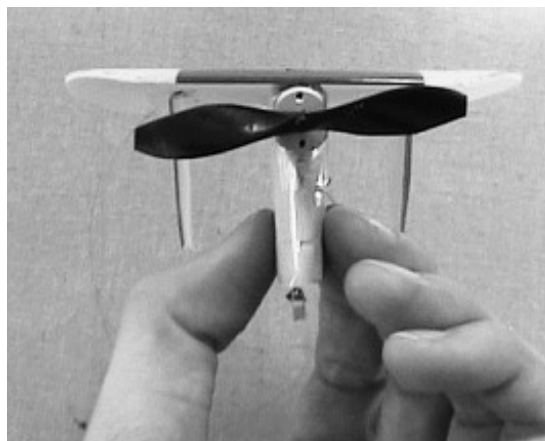
Figure 7 - Brigham-Young University MAV

(Journal of Aircraft AIAA 2003-416)

Figure 8 - Dragon Slayer MAV (http://www.miraterre.com)
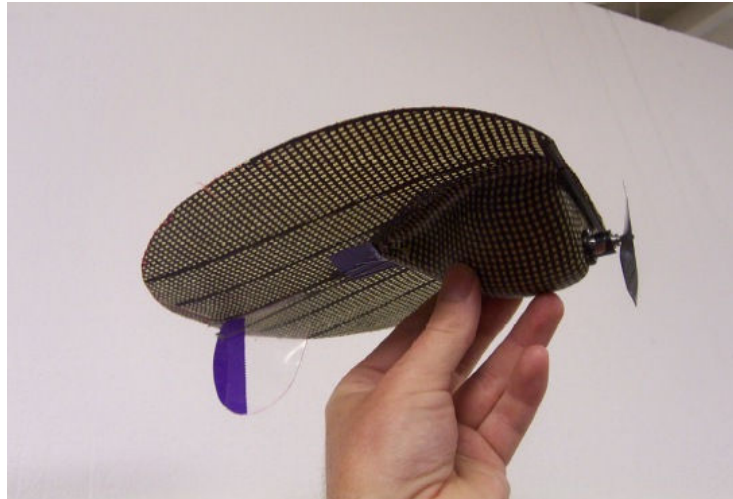
Figure 9 - University of Arizona variable camber MAV

(NASA Contractor Report NASA/CR-2004-213271)
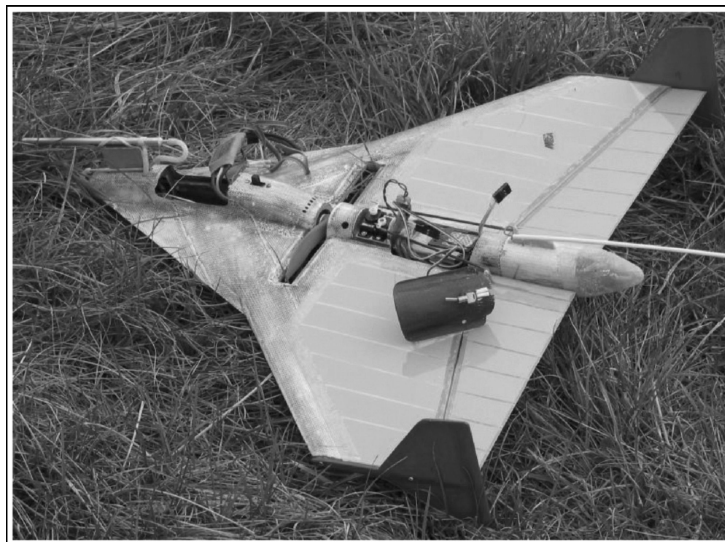
Figure 10 - MAV from Warsaw University of Technology (WUT)

(C. Galinski)

Figure 11 - IAI Mosquito 1

(http://hp.kairaven.de/bigb/mav.html)

Figure 12 - Dragonfly MAV from University of Arizona

(http://clubs.engr.arizona.edu/mav/)

MAVs used internal combustion (IC) glow engines a few years ago but nowadays all MAV use electric motors only. The advance in the design of brushless electric motors and new lightweight, high capacity Lithium-Polymer (LiPo) batteries makes them much more reliable, easier to control and more powerful with virtually no weight penalty. Hence only brushless electric motors were considered as propulsion options for the BumbleBee. Advances in miniaturizing electronic equipment also contributed to new, micro-sized servomechanisms and RC (Radio Control) receivers. Servos weighing only ~5g have torque ratings of 500g-cm and above, which is fully sufficient for relatively small control surfaces of typical fixed-wing MAVs.

It can be seen in the figures above and in Table 2 that many designs which may have quite similar performance differ significantly in the approach to the airframe structure type, aerodynamics and size. Wing planform is the most important factor of the MAV's geometry with respect to performance. Four distinct planforms are most common in UAV designs – rectangular, elliptic, Zimmerman and inverse Zimmerman. Zimmerman and inverse Zimmerman planforms are formed by 2 ellipses. They were introduced by Zimmerman whilst working on low aspect ratio wings at NACA [13]. They all have slightly different aerodynamic and geometrical characteristics. When working on an aircraft with restricted size, the position of the wing's *AC*, location of the equipment and other stability-related issues sometimes become one of major decision-driving properties.

Some of the MAVs described above have stability-augmenting devices, IR or accelerometer-based stabilization systems.

As it can be seen in the outline of the designs, the majority are built in a flying wing configuration of low aspect ratio (LAR). This has two basic advantages. Firstly, it allows the overall size of the aircraft to be kept low while having large wing area and wing chord, which is crucial for the Reynolds Number. Secondly, it makes the whole airframe more compact than in the case of classical or canard configurations thus making it less vulnerable to damage on landings and handling. Since one of the aims of the MAV design was to keep the airframe small, these two features dictated that further design should be carried out for a tailless configuration.

One problem associated with LAR wings for MAVs is the excessive drag at higher angles of attack. A huge portion of the lift they create comes from strong vortices above the wing's surface. Low *Re* accounts for relatively high drag coefficient too but this would be exacerbated even further by using a classical configuration with smaller wing chord. Usually MAV wings have a very modest amount of camber [2, 14]. In fact, the aerofoil has much less impact on the performance of a LAR wing at low Re than in classical, full size aircraft and the MAV's performance depends mostly on the wing planform and the Re [14, 15]. Because of this and the lack of available theories which give reliable results for MAV wing characteristics, a flat plate aerofoil was chosen for the conceptual design stage. This has a relatively small impact on the performance of the micro-scale aircraft.

3.2 Preliminary sizing

To have at least a rough idea of the size of the vehicle, a preliminary choice of equipment had to be made. The limiting factor was the budget for the prototype manufacturing.

The onboard equipment (payload), propulsion and control equipment were COTS (Commercial, Off-The-Shelf) elements, many of which are used in RC modelling. Because of the vast choice, only some general assumptions were made and the

final selection of these components was to be done at a later stage, with more detailed knowledge of the MAV's performance characteristics. An outline of all the component weights is presented in Table 3.

Table 3 - MAV preliminary weight breakdown

Misc (pushrods, ctrl. horns etc.)	10
Motor	25
Battery	52
Speed controller	7
RC receiver	7
Servos (3)	12
Propeller	3
Camera system	20
GPS	13
IR stabilization system	15
Camera/GPS battery	10
GPS transmitter	10
Airframe	25
TOTAL	**209**

It is worth noting that while the motor and control systems (RC receiver and servos) can be driven from a single LiPo battery, the data transmitters must be run from another power source because the motor controller usually produces electronic noise which can prevent proper functioning of the transmitters.

The weight of the airframe for rough sizing was based on previous experience with MAVs [5]. At this stage it was assumed that the MAV would be made mainly of depron foam and composite materials (glassfibre, carbonfibre or Kevlar). Airframe weight was assumed to be approximately 25g at this stage.

3.3 Wind tunnel test model size estimation

In order to later validate the method of calculating the performance, a series of wind tunnel tests were carried out. Models for these tests were designed to be roughly the size of the final MAV as this would assure similar *Re* for both tests and

the final prototype. The model wing size estimation was based on the stall speed requirement:

$$S = \frac{2mg}{\rho V_{stall}^2 C_{L\max}}$$

(1)

The value of the $C_{L\max}$ was based on polars from [14, 15] and varies from 0.8 to 1. In this case a value of ~0.95 was used for estimation of the wing area for most of the wind tunnel models. For direct comparison they were manufactured in one 'size' (b and c_{root}). Since the wind tunnel experiments were conducted for 3 different Re for each of the models, later comparison at different speeds is possible by simply interpolating between tested points.

The aspect ratio of the wings was chosen only on the basis of the root chord (230mm) and wingspan (300mm). A root chord slightly shorter than the wingspan permits extension of the fuselage in front of the leading edge thus attaining proper positioning of the Centre of Gravity (CG) while keeping the maximum dimension small.

Another problem which was encountered at this stage was lack of data concerning drag coefficients of fuselage bodies at low Re. This was essential for precise predictions of the MAV's aerodynamic characteristics and later optimization. The fuselage sizing was driven by the requirement to contain all the equipment. This was evaluated using Alibre Design Xpress, 3D CAD software [16].

The wind tunnel test models are described in detail in Chapter 4.

4. Wind tunnel testing

Seven Micro Aerial Vehicle (MAV) wings of different planform were tested at the University of Glasgow. Five configurations, made of three wing models with 2 generic fuselages, were also tested.

4.1 The Anatomy Wind Tunnel

The Anatomy Wind Tunnel at the University of Glasgow is of a closed circuit type (Figure 13). It has a 1.8 m long test section of rectangular cross-section 1.14 m wide and 0.83 m high. The wind tunnel is capable of speeds up to 29 m/s. The minimum steady flow speed is 2-3 m/s. The fan is driven by an electric motor via an electromagnetic coupling.
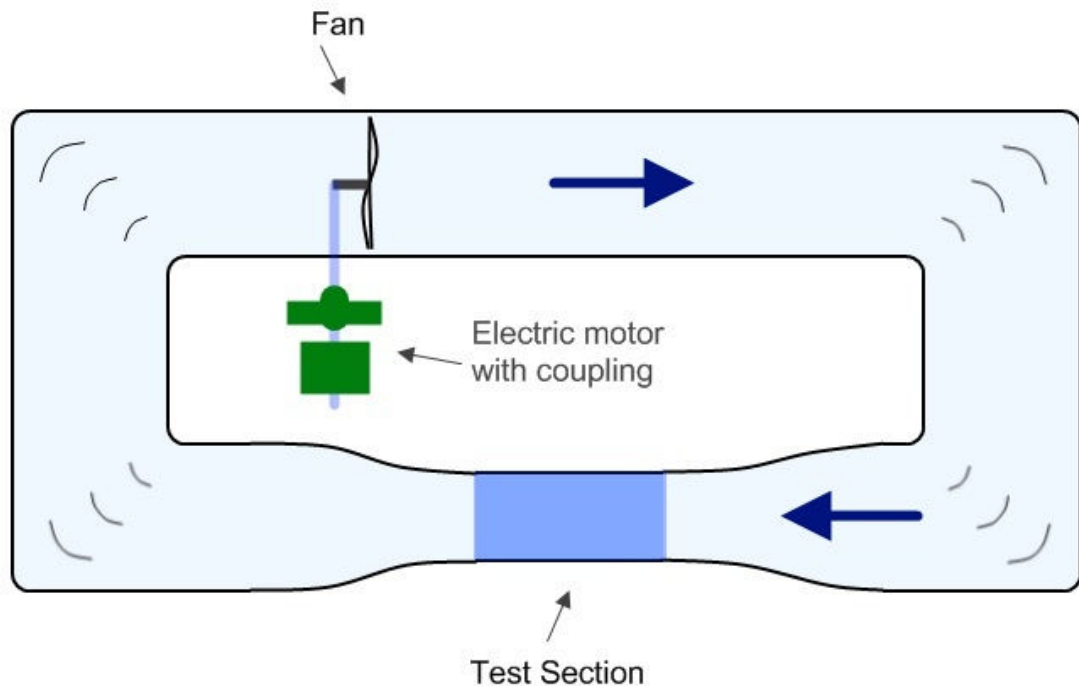
Figure 13 - Closed circuit wind tunnel scheme

4.2 Force balance and data acquisition

A six-component AMTI® FS6-100 load cell with AMTI® DigiAmp DSA-6, 16-bit analog/digital converter connected via ethernet to a PC were used to measure two forces (F_x, F_z) and one moment (M_y). The forces were measured with 0.01N and the moment with 0.01Nm resolutions. The relatively small measurement range of the load cell was used which has a load capacity of 440N on F_z, 220N on F_x and

11Nm on M_y. Experimental data was acquired using a PC with AMTI[®] NetForce 2.1 acquisition software. 100 samples were taken at each channel for a given angle of attack (α) at 100Hz sampling rate. A Bessel type 20Hz filter was used to reduce the noise on all of the data channels. Acquired data was saved into text files and the forces were later resolved into Lift, Drag and Pitching Moment. Position of the origin of the load cell coordinate system was taken from the manufacturer's load cell calibration spreadsheet.

4.3 Test stand setup

The test stand used in this experiment has been designed specifically for use with the FS6 load cell. Models were mounted to a vertical sting attached to the load cell; see Figs. 14, 15, 16. The angle of attack α was changed by pivoting the whole stand about the axis just above the wind tunnel floor. The sting and the load cell were not shrouded.

The length of the sting was chosen as a compromise between reducing the aerodynamic interference and load cell internal friction interactions (see section 4.9 for more details). The angle of attack α could be varied between -14° and +44° with 2° steps. This was done manually, securing the main arm of the test stand at each position to a plate under the wind tunnel floor with a pin. A detailed technical drawing of the test stand can be found in the Appendix (section 11.3).
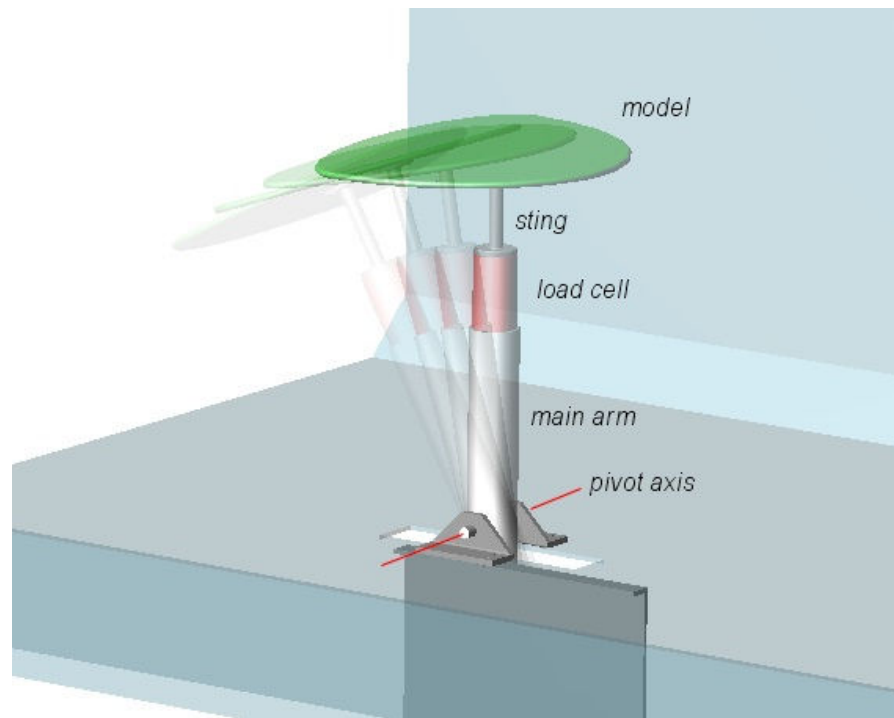
Figure 14 - Test stand design, modeled in 3D CAD system
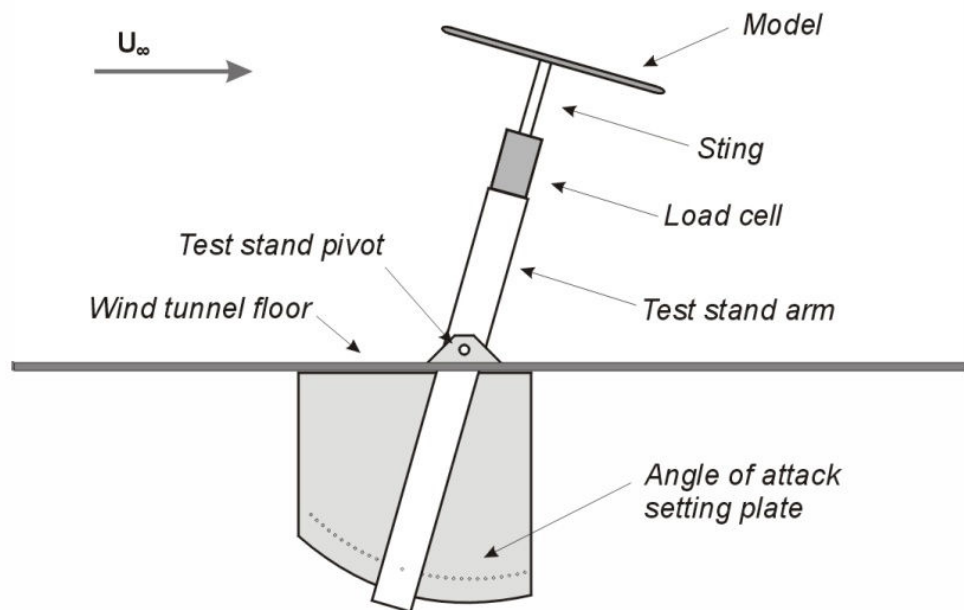
Figure 15 - Wind tunnel test rig setup
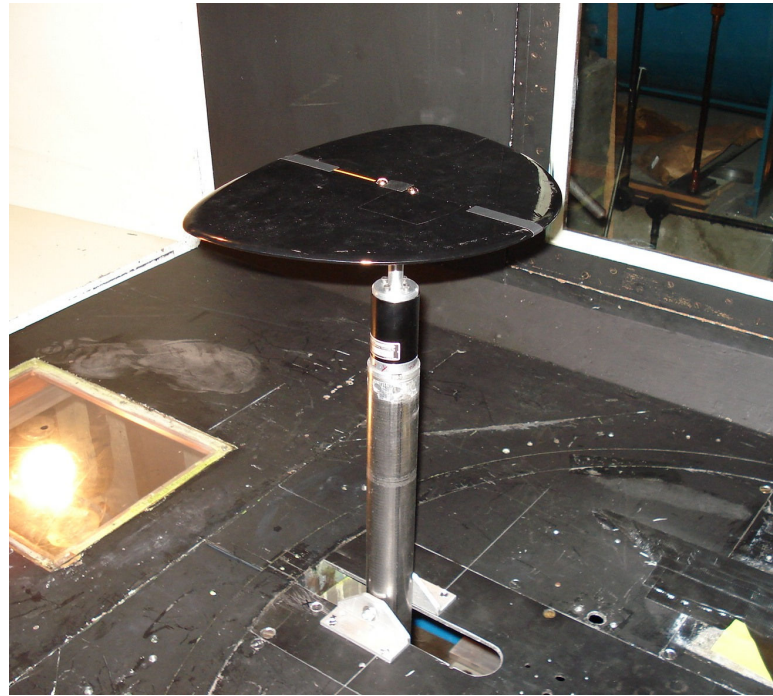
Figure 16 - Inverted Zimmerman wing model mounted to the rig in the wind tunnel

4.4 Test models

Models were 6mm thick flat plates with 2:1 elliptical edges. Details on their shape parameters and dimensions can be found in Table 4 and in Figure 17. Models were made out of 3 plies of balsa wood glued with epoxy and stiffened with strips of glassfibre composite along their centerline (Fig. 18). Black Solarfilm® (heat-shrinkable film) covering was used to achieve a smooth surface. Fuselages were made out of balsa and also covered with Solarfilm®. Some glassfibre composite plates were used as reinforcement in the area where the fuselage was attached to the sting. On the front of the fuselage a S2 brushless outrunner motor was mounted.

All the configurations were tested at three velocities: 7.72m/s, 10.81m/s and 15.44m/s which gave Reynolds numbers: 1×10^5, 1.4×10^5 and 2×10^5 at MAC (Eq. 2) for the elliptical, Zimmerman and inverse Zimmerman planforms. The remaining 3 planforms were tested at the same airflow velocities, as this saved a considerable amount of time required for testing lift, drag and moment of the sting.

Dependence between coefficients and *Re* is shown in further analysis so that the characteristics of all the planforms can be compared.

$$Re = \frac{Uc}{\nu}$$

(2)

where:

U - Airflow speed,

c - Wing chord

ν - Air kinematic viscosity.

Following models were tested (Fig. 17):

1. Elliptical
2. Zimmerman
3. Inverse Zimmerman with 0° dihedral
4. Inverse Zimmerman with 10° dihedral
5. Negative sweep
6. Rectangular
7. Morphing planform

Detailed drawings of the models can be found in the Appendix (section 11.4). Geometric parameters of the models are shown in the Table 4.

Additionally, two fuselages (called *fuse1* and *fuse2*) were tested with the Zimmerman and Inverted Zimmerman wings. Fuse1 was also tested with the Morphing wing. The fuselages had different cross-sections – fuse1 had a rectangular cross-section while Fuse 2 had a triangular cross-section. Both of them were designed as generic MAV fuselage shapes to house the same amount of equipment, which was evaluated in the Alibre Xpress 3D CAD system.
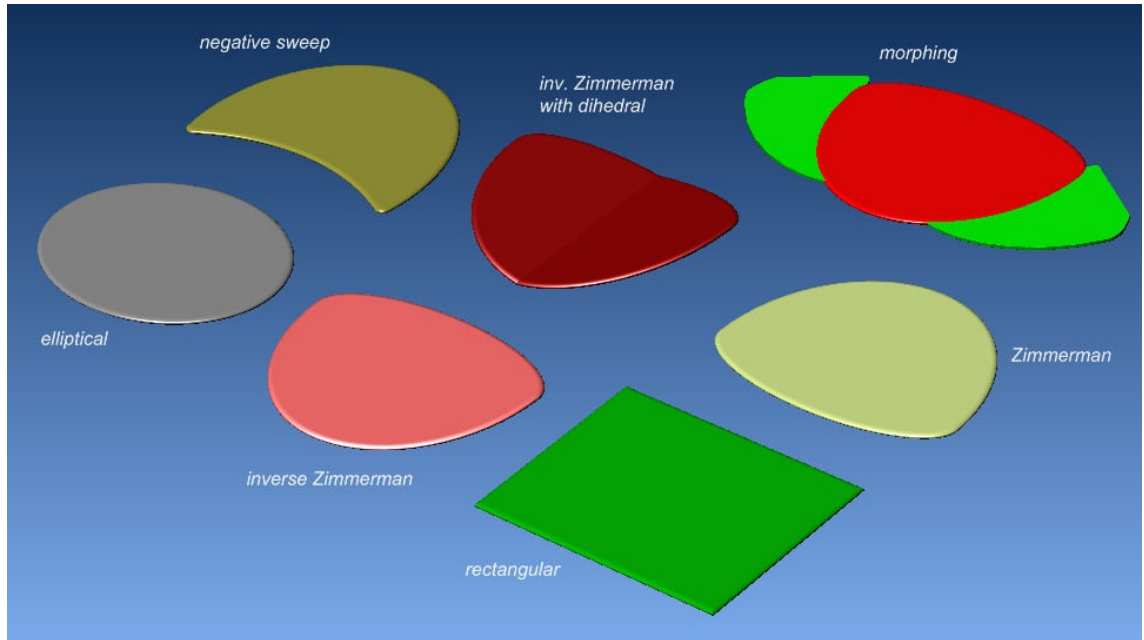
Figure 17 - Test models

Table 4 - Parameters of the wind tunnel test models

	b [mm]	MAC [mm]	S [m2]	t/c [%]	AR
Elliptical	300	195.6	0.054	3.1	1.66
Inv. Zimmerman	300	195.6	0.054	3.1	1.66
Zimmerman	300	195.6	0.054	3.1	1.66
Negative sweep	300	165.7	0.048	3.6	1.87
Rectangular	300	230.0	0.069	2.6	1.30
Morphing	520	182.4	0.086	3.3	3.15

Notes on some of the planforms:

- The Zimmerman and Inverse Zimmerman planform is formed by joining two half-ellipses [13, 14].

- The negative sweep planform is a modified Zimmerman planform formed by reversing the leading-edge half-elliptical.

- The morphing planform is based on an Inverted Zimmerman planform with additional surfaces extended on the leading/side edges. The modification is made in such a way that the surfaces can be fully confined within the planform of the main (inv. Zimmerman) wing and their deployment does not change the position of the aerodynamic centre (AC) of the wing.

Figure 18 - Wind tunnel test model manufacturing

4.5 Test Procedures and calibration

Models were tested at angles of attack from -4° to 36° except the tests for Zimmerman and Elliptical wings, which were tested up to 44° as they showed stall at relatively high α - around 40°. Before testing each model, tare measurements were taken to be later subtracted. Three tare measurements were made and later their average was taken as the tare.

Runs of the sting alone were also made and data recorded. As later analysis revealed that the lift, drag and pitching moment slopes of the sting were not smooth (due to very small aerodynamic forces), nevertheless they showed a clear trend and these forces were later subtracted from model test runs. Sting tests were done using a dummy sting – a sting without the upper plate which attaches flush with the model, as this provided more realistic representation of the sting-alone lift, drag and pitching moment. Before attaching the model to the sting the tunnel was run for approximately 15 to 20 minutes in order to cool down the load cell, which showed significant drift caused by the change of the ambient temperature. After cooling down all channels on the load cell were zeroed, the

model was attached and the data measurements were taken. The Reynolds number for each model is based on the freestream velocity which was set with model at $\alpha=0°$. However, the velocity in the wind tunnel was controlled during the experiment and did not show any changes throughout the runs. The velocity setting was based on the readout of the electronic manometer which measured the difference in static pressure between the working (test) section (p_w) and the settling chamber (p_s) of the Anatomy Wind Tunnel. These settings were calculated each day because of changing atmospheric conditions (pressure and temperature) which were monitored for possible changes. Air density ρ was calculated using the formula:

$$\rho = \frac{p}{RT} \tag{3}$$

The dynamic pressure in the test section q_w is:

$$q_w = K\left(p_s - p_w\right) \tag{4}$$

Finally, the freestream velocity in the wind tunnel test section U_∞ is:

$$U_\infty = \sqrt{\frac{2q_w}{\rho}} \tag{5}$$

4.6 Wind tunnel corrections

The lift, drag and pitching moment coefficients were corrected for tunnel blockage (solid and wake) using the method described in [17]. The least complicated method was used as the blockage was supposed to be a rather small correction. Total blockage was taken as:

$$\varepsilon_t = \varepsilon_s + \varepsilon_w \tag{6}$$

and it can be approximated by:

$$\varepsilon_t = \frac{1}{4}\frac{F}{C} \tag{7}$$

Because the image system was not used in the wind tunnel, total blockage must account for model, struts and the windshields [17]. Therefore all the components in the wind tunnel test section were taken into account for the blockage calculations. For the most critical case, which is the model with largest wing area (the Morphing planform) at highest angle of attack tested (α=36°), the blockage was 1.7%. Blockage values differed for each planform tested and therefore the blockage at the highest α was smaller for the rest of the tested models, reaching 1.2% - 1.4%. Blockage correction was applied in aerodynamic coefficient calculations:

$$U_C = U_\infty (1 + \varepsilon_t)$$

(8)

Correction for the streamline curvature was also calculated to estimate if it could have a noticeable effect on the measured values. It turned out to be considerably small (0.15% for C_L, 0.04% for C_M at the maximum values of these coefficients) and therefore could be neglected. Geometric correction of -0.6° was used for the angle of attack for all wing models and wing-fuse1 configurations. No correction was needed for wing-fuse2 configurations. The angle of attack was measured with an electronic inclinometer with 0.1° accuracy.

4.7 Force calculation

After taking the measurements of the two forces and a moment from the load cell: $F_{z\ test}$, $F_{x\ test}$ and $M_{y\ test}$, tare and sting force components were subtracted from them (F_z', Fx' and M_y') in order to have the normal force (F_z), the axial force (F_x) and the pitching moment (M_y). The lift, the drag and the pitching moment about the quarter point of the MAC were therefore calculated using equations:

$$L = -F_z \cos\alpha - F_x \sin\alpha$$

(9)

$$D = F_x \cos\alpha - F_z \sin\alpha$$

(10)

$$M_{0.25} = M_y + F_z \cdot a - F_x \cdot h$$

(11)
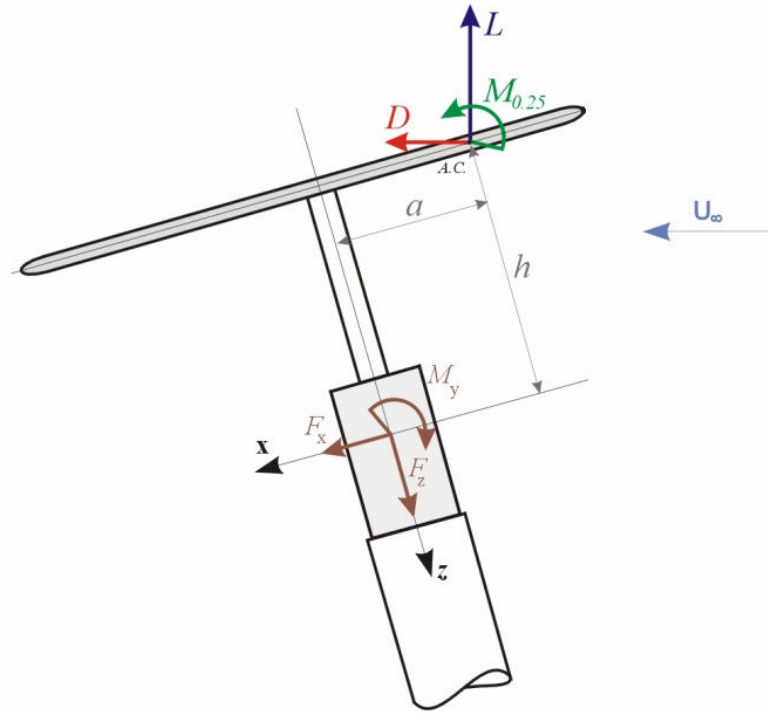
Figure 19 - Forces and moments on the test model

The force component convention is shown in Fig. 19; the moment equation is resolved around the load cell coordinate system origin. Distance *a* was different for each wing as the sting attachment point was around the CG of the model. The position of aerodynamic centre and length of the MAC for each wing was calculated using the AC Calculator by Martin Hepperle [18]. The distance *h* was constant for all but the 'Inverted Zimmerman 10 deg dihedral' wing which had greater distance from its AC to the load cell coordinate system origin because of the dihedral. Coefficients C_L, C_D and $C_{M0.25}$ were calculated using equations:

$$C_L = \frac{L}{\frac{1}{2}\rho U_\infty^2 S} \tag{12}$$

$$C_D = \frac{D}{\frac{1}{2}\rho U_\infty^2 S} \tag{13}$$

$$C_{M_{0.25}} = \frac{M_{0.25}}{\frac{1}{2}\rho U_\infty^2 S \bar{c}} \tag{14}$$

4.8 Uncertainty of measurements and repeatability

The uncertainty of angle of attack was assumed to be 0.1° - the precision of the electronic inclinometer used for measuring it on a model mounted to the sting. For C_L, C_D, $C_{M\,0.25}$ and L/D uncertainty analysis was carried out using the method [19] based on Kline and McClintock [20] which estimates the error from the specifications of the uncertainties of the primary experimental measurements. It is assumed that the result R depends on i number of parameters x_i. Uncertainty of measuring each parameter x_i can also be estimated. Uncertainty in the result R caused by a single parameter is:

$$\sigma_{R_i} = \pm \left(\frac{\partial R}{\partial x_i} \right) \sigma_{x_i} \qquad (15)$$

The uncertainty of the result R, caused by all the parameters it depends on, is given by:

$$\sigma_R = \pm \sqrt{\left(\frac{\partial R}{\partial x_1} \sigma_{x_1} \right)^2 + \left(\frac{\partial R}{\partial x_2} \sigma_{x_2} \right)^2 + ... + \left(\frac{\partial R}{\partial x_n} \sigma_{x_n} \right)^2} \qquad (16)$$

While for the lift, drag and pitching moment the uncertainty will depend on their value, the uncertainties of the remaining parameters have constant values. All of the values listed in the Table 5 were based on the uncertainties of the measuring tools used. It was assumed that the uncertainty of lift, drag and pitching moment is based on the resolution of the forces measured on the load cell.

Table 5 - Wind tunnel experimental uncertainties

σ_L	σ_D	$\sigma_{M0.25}$	σ_P	σ_S	σ_U		
					7.72 m/s	10.81 m/s	15.44 m/s
0.01/L	0.01/D	$0.01/M_{0.25}$	0.005	0.05	0.004	0.002	0.001

Because the uncertainties of lift, drag and pitching moment depended on their values at a given angle of attack, the uncertainty of each coefficient also varies. For low angles of attack where aerodynamic forces are minimal, the uncertainties are high. At angles of attack above 8°-10° (where forces are higher), the uncertainties range between 5% - 6% for C_L and C_D, 7% - 12% for C_M and 7% - 10% for L/D. A typical graph with error bars is shown in Figure 20. Uncertainties of

coefficients depended on σ_ρ, σ_S, σ_U and, depending on the coefficient: σ_L (for C_L), σ_D (for C_D) and $\sigma_{M0.25}$ (for $C_{M\ 0.25}$). Uncertainty of L/D depends on C_L and C_D uncertainties.

The repeatability of the experiments was mostly within the uncertainties of the tested values. Some more significant differences can be seen only on the lift curve slopes, around the stall which sometimes varied slightly between the runs. One specifically significant case is the Elliptical wing at *Re=100,000*, whose lift curve slope had shown a bifurcation occurring around *α=24°*. This case is described in section 4.10. A graph with data from three runs of $C_L(α)$, $C_D(α)$, and $C_{M\ 0.25}(α)$ depicting the repeatability of tests is shown on Fig. 21. The difference in the lift curves around *α=24°* is caused by a milder stall for this test run. It does not have any effect on the other parts of the polar as performance around $α_{stall}$ is not used later on in the performance analysis.
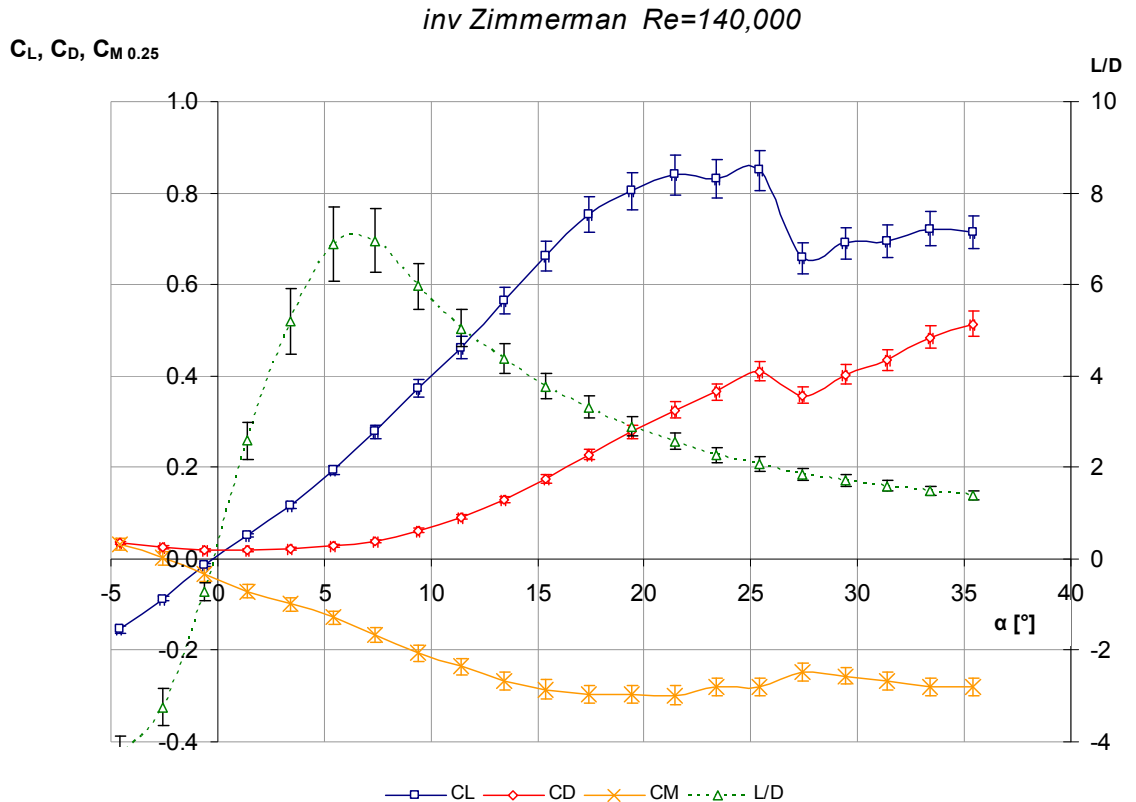
Figure 20 - Graph illustrating errors of a typical test
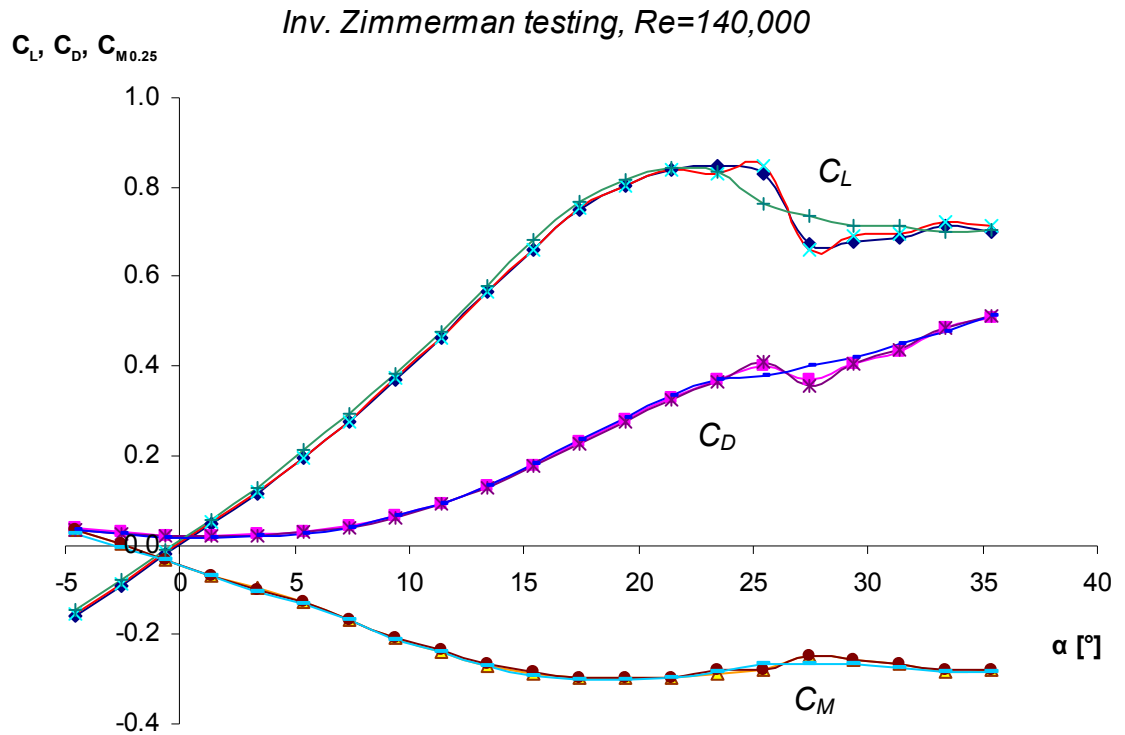
Figure 21 - Repeatability of the test runs.

4.9 Problems encountered during the tests

Some problems were encountered at the beginning of the wind tunnel testing. In the initial design the sting was mounted horizontally to the load cell. It was later discovered that this was causing internal interactions in the load cell. As a result the lift and drag slope curves were shifted. The minimum of the drag curve was placed around $α=6°$, which was rather unusual for a flat plate aerofoil. Since some interference from the sting was suspected, the whole load cell and sting were shrouded with a thin glassfibre structure. This made no significant difference to the results. Inverting the model to check if the shift is not caused by some manufacturing errors (i.e. slightly cambered wing) also did not change the situation – the drag slope curve was still shifted towards positive angles of attack. Also, minimum values of drag were 2-4 times smaller than values in published papers concerning similar MAV wing planforms. Therefore, this proved that the problem was most probably due to some mechanical interactions within the load cell itself. The repeatability of the results was also significantly worse if compared to the measurements taken with later refined design incorporating the vertical sting.

A few test runs were carried out with the model attached directly to the top of the load cell. The results showed that the minimum of the drag curve slope was around $\alpha=0°$. Neglecting the interference problems (caused by attaching the model directly to the load cell), this proved that at low α the center of gravity of both the model and the sting should be not far from the origin of the load cell coordinate system in order to avoid any mechanical interactions inside the load cell of this type. A new sting design with the model sitting directly over the load cell proved to be a solution to the problem.

Another problem which had not been resolved was the slight non-zero pitching moment coefficient at $\alpha=0°$ for all of the tests (all models). This was most probably due to some interference between the model, sting and the load cell. It appeared the same for models in normal and upside-down positions therefore was not caused by manufacturing errors. The $C_{M0.25}$ was not the most important parameter to test for the latter parts of the project, so it was decided that no further investigation of the problem would be carried out at this time.

4.10 Results

The results presented in Figs. 22 - 33 show a set of four graphs containing $C_L(\alpha)$, $C_D(\alpha)$, $C_{M\ 0.25}(\alpha)$ and $L/D(\alpha)$ for each configuration tested. Figure 34 shows the drag polars of the fuselages. Figure 35 shows comparisons of the tested configurations. Each graph shows the coefficient curves for the three Reynolds numbers. Each curve presented here is averaged from 3 runs. The only exception is the Elliptical wing planform, which had shown bifurcation of the lift curve slope at $Re=100,000$ and therefore the results presented for this configuration are the curves from separate runs in order highlight this phenomena.
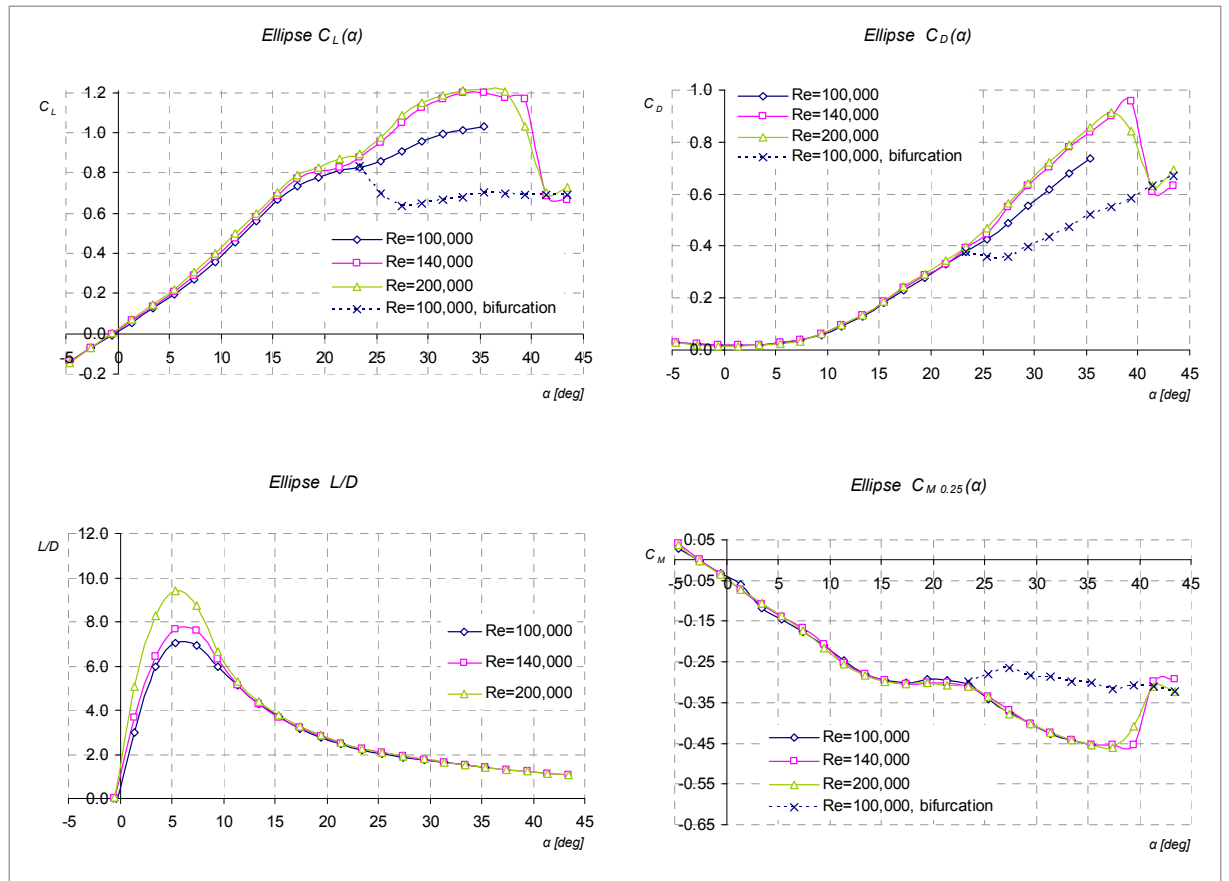
Figure 22 - Elliptical wing test results
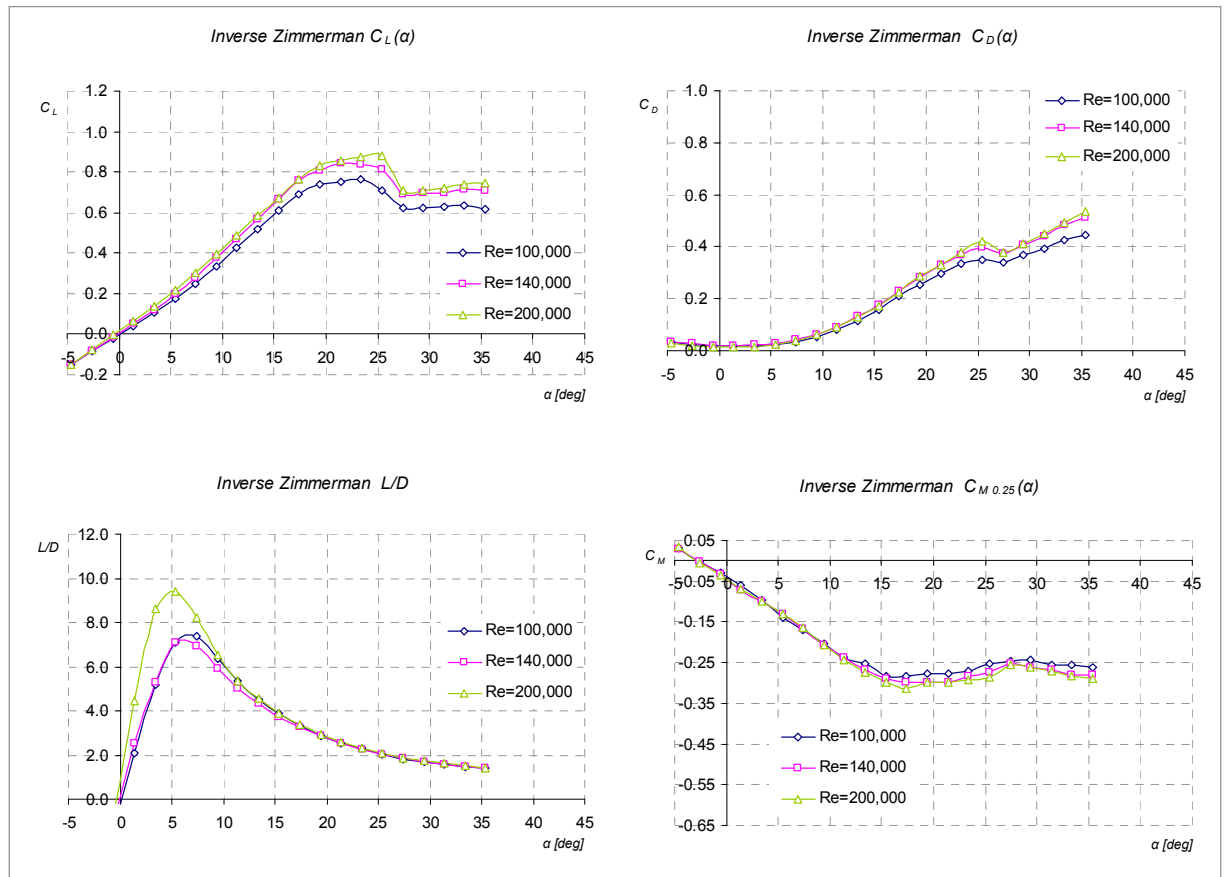
Figure 23 - Inverse Zimmerman wing test results
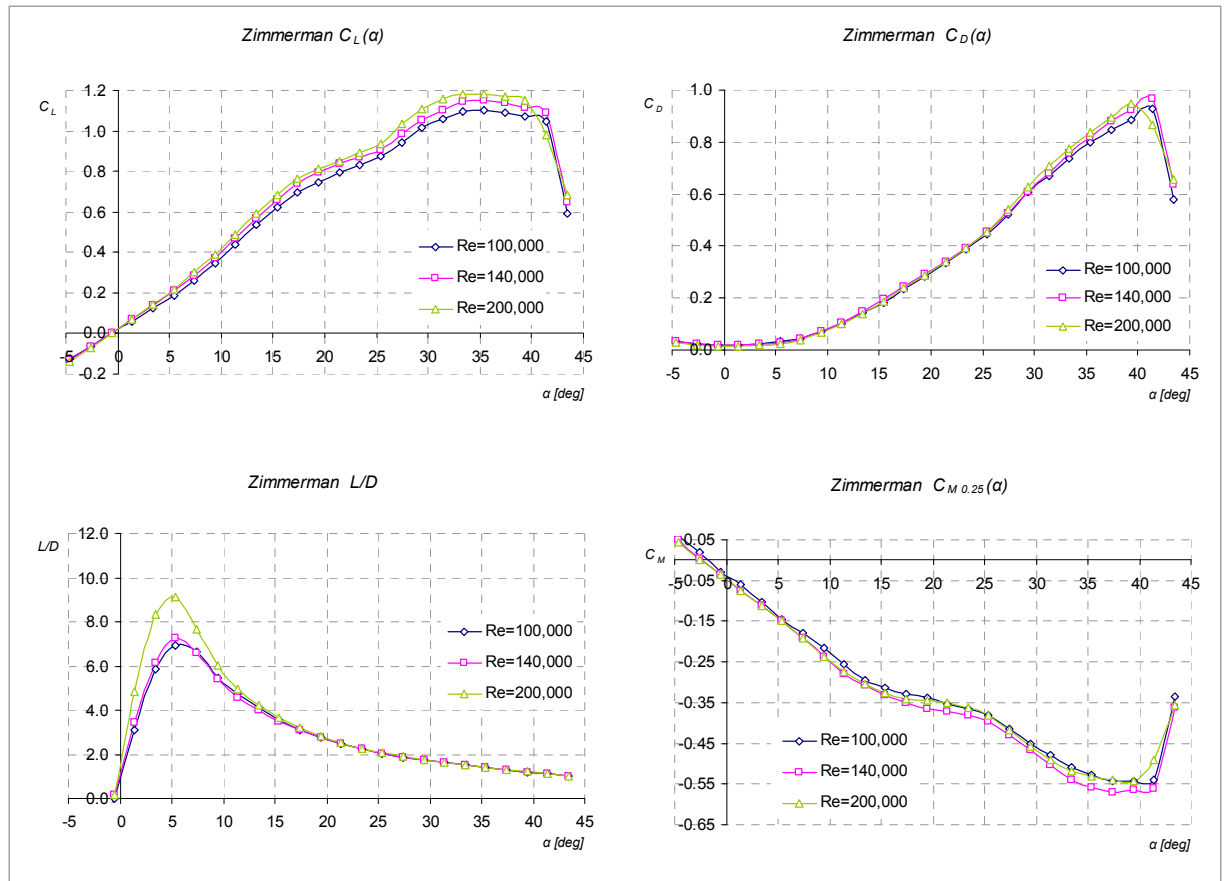
Figure 24 - Zimmerman wing test results
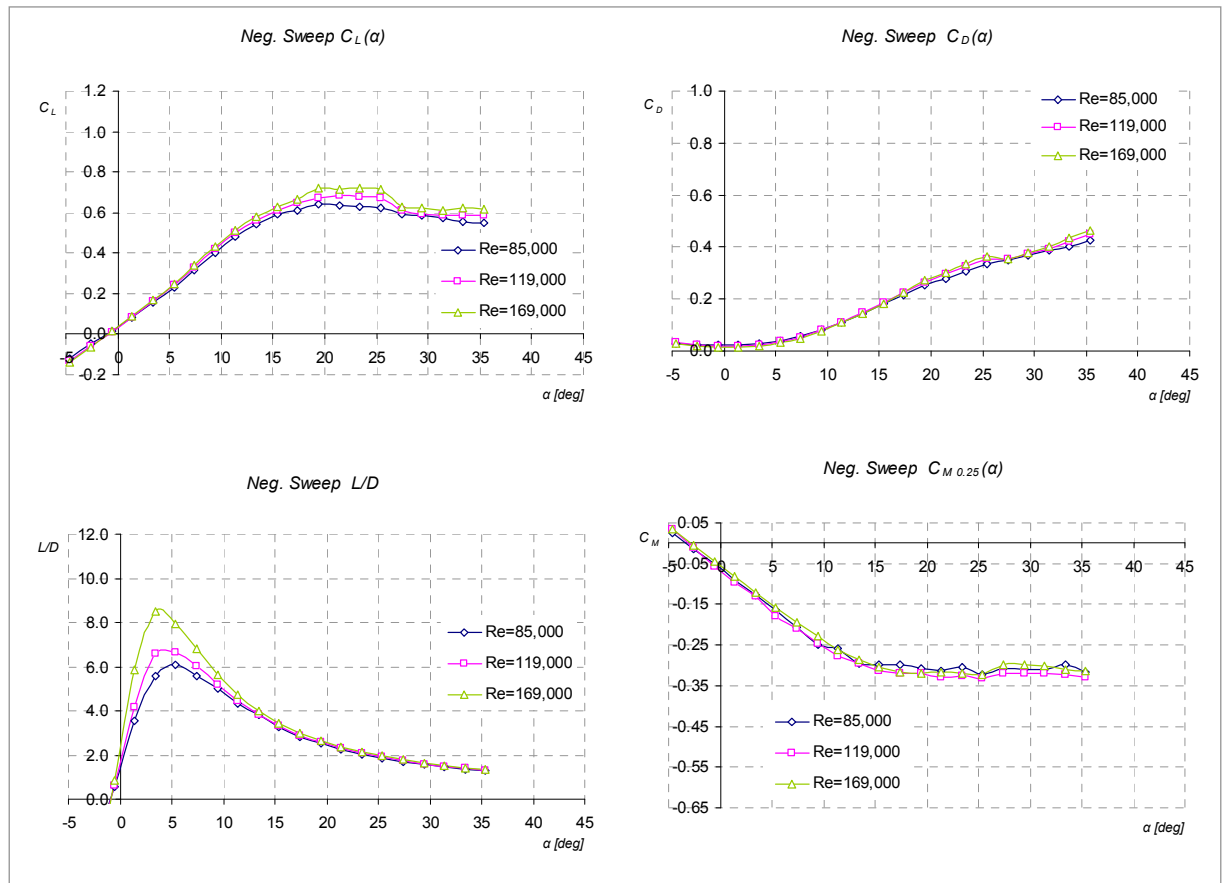
Figure 25 - Negative sweep wing test results
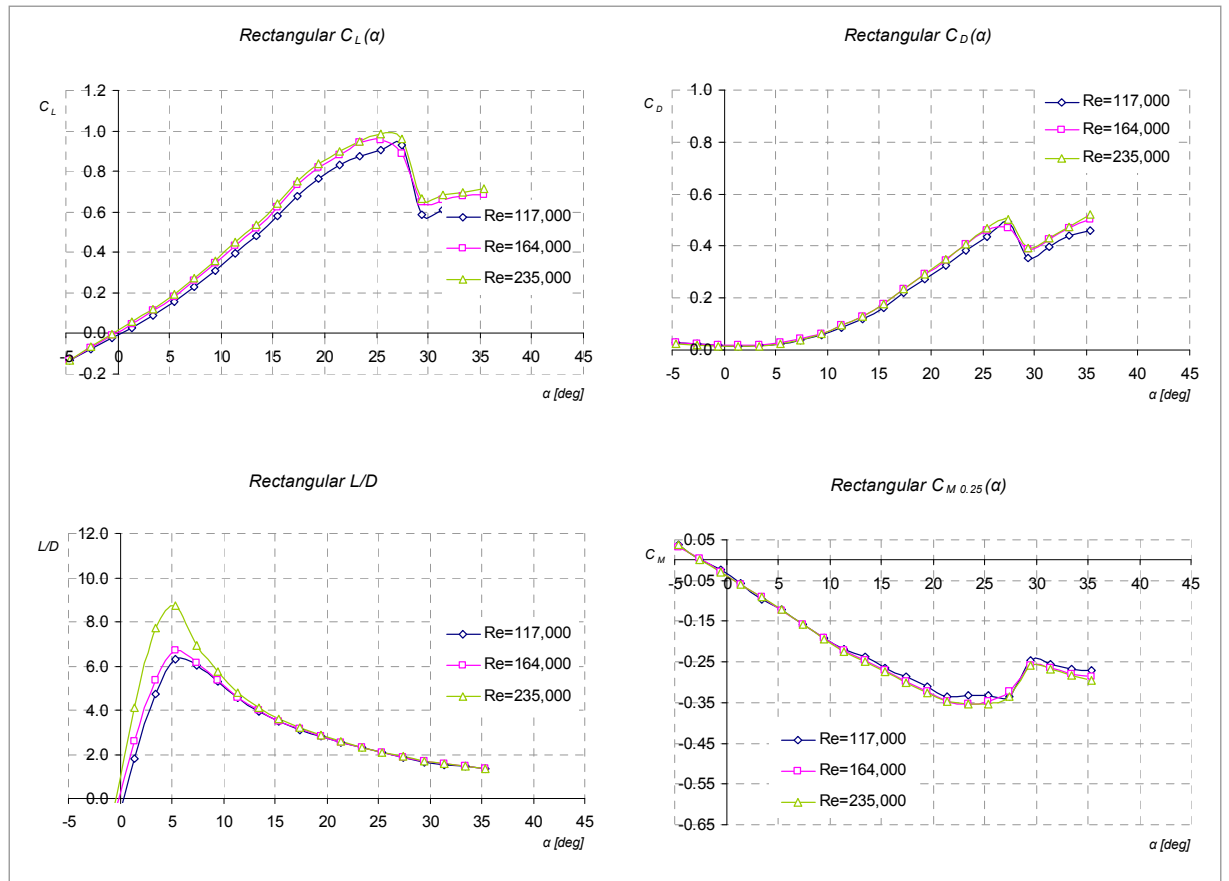
Figure 26 - Rectangular wing test results
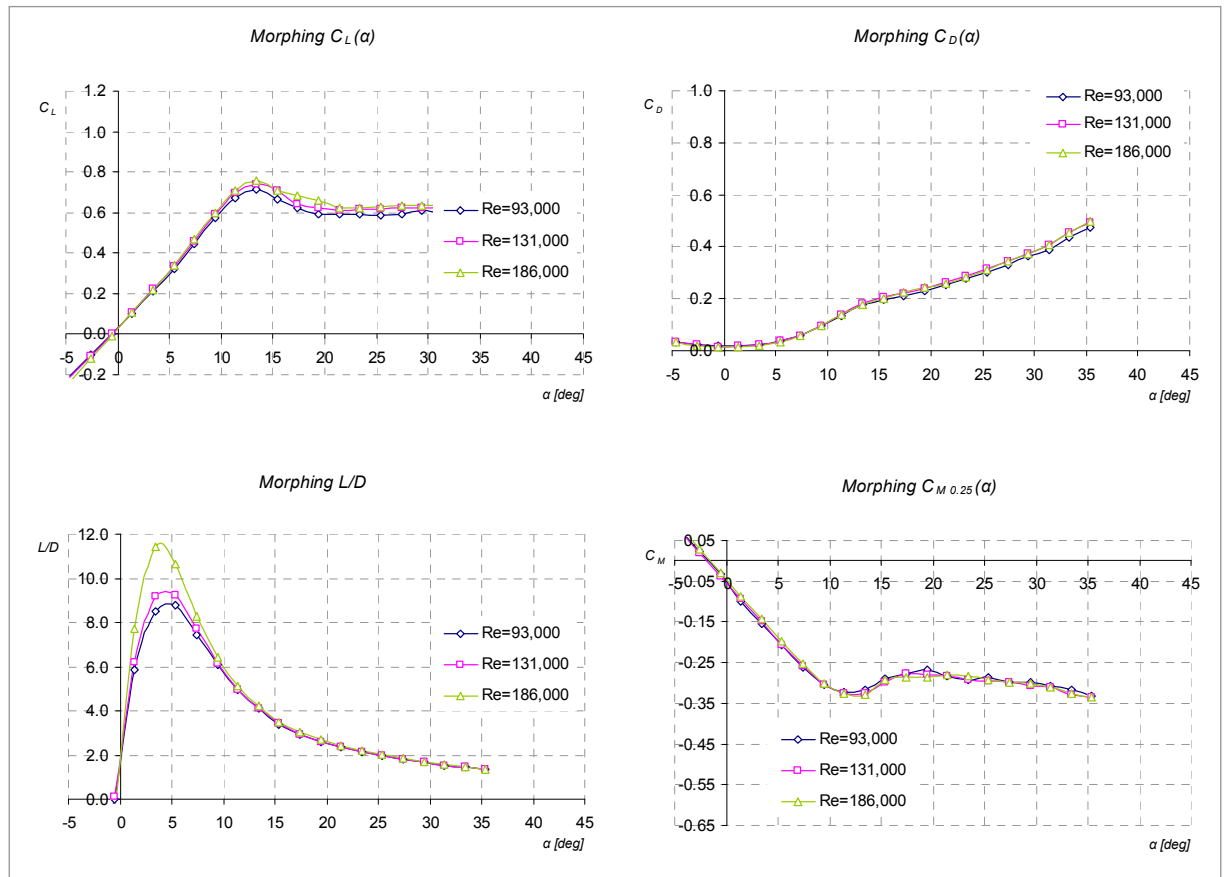
Figure 27 - Morphing wing test results
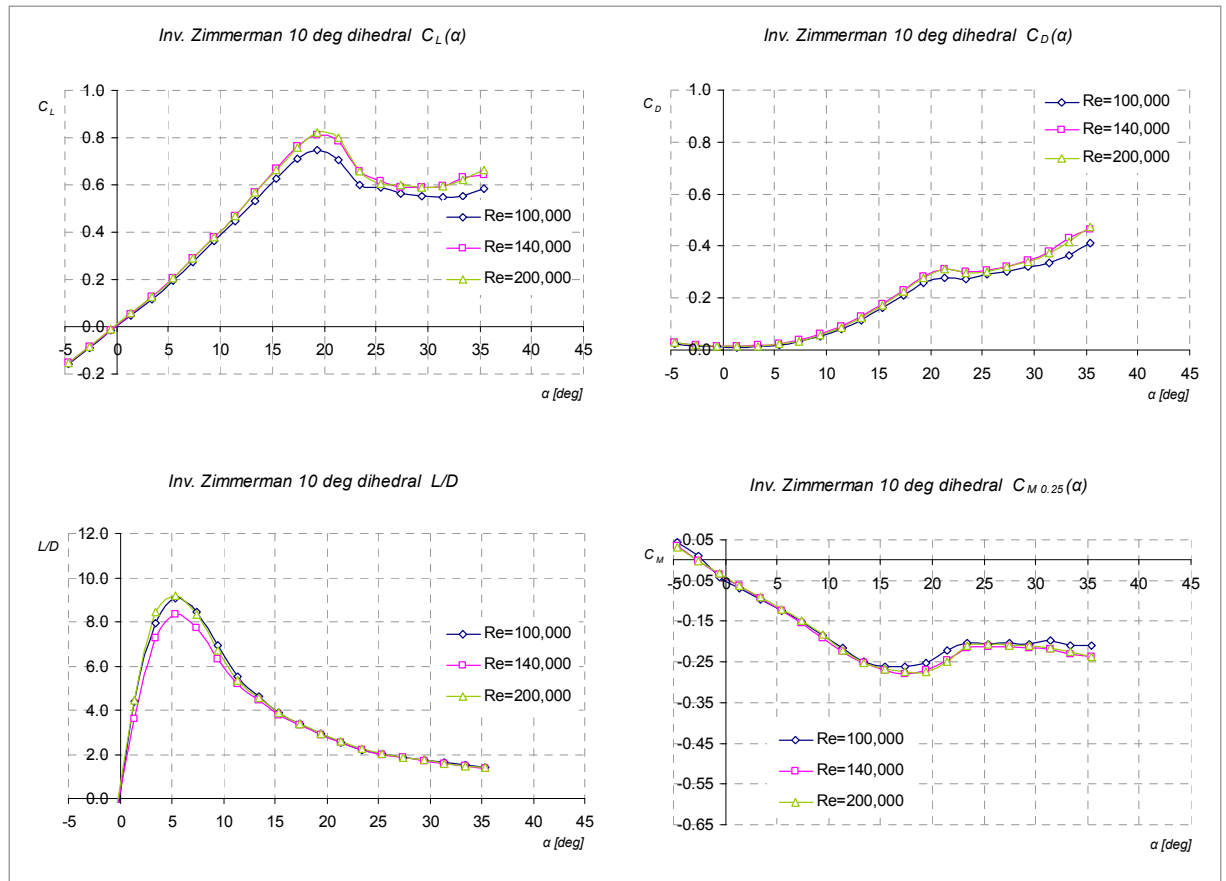
Figure 28 - Inverse Zimmerman wing with dihedral test results
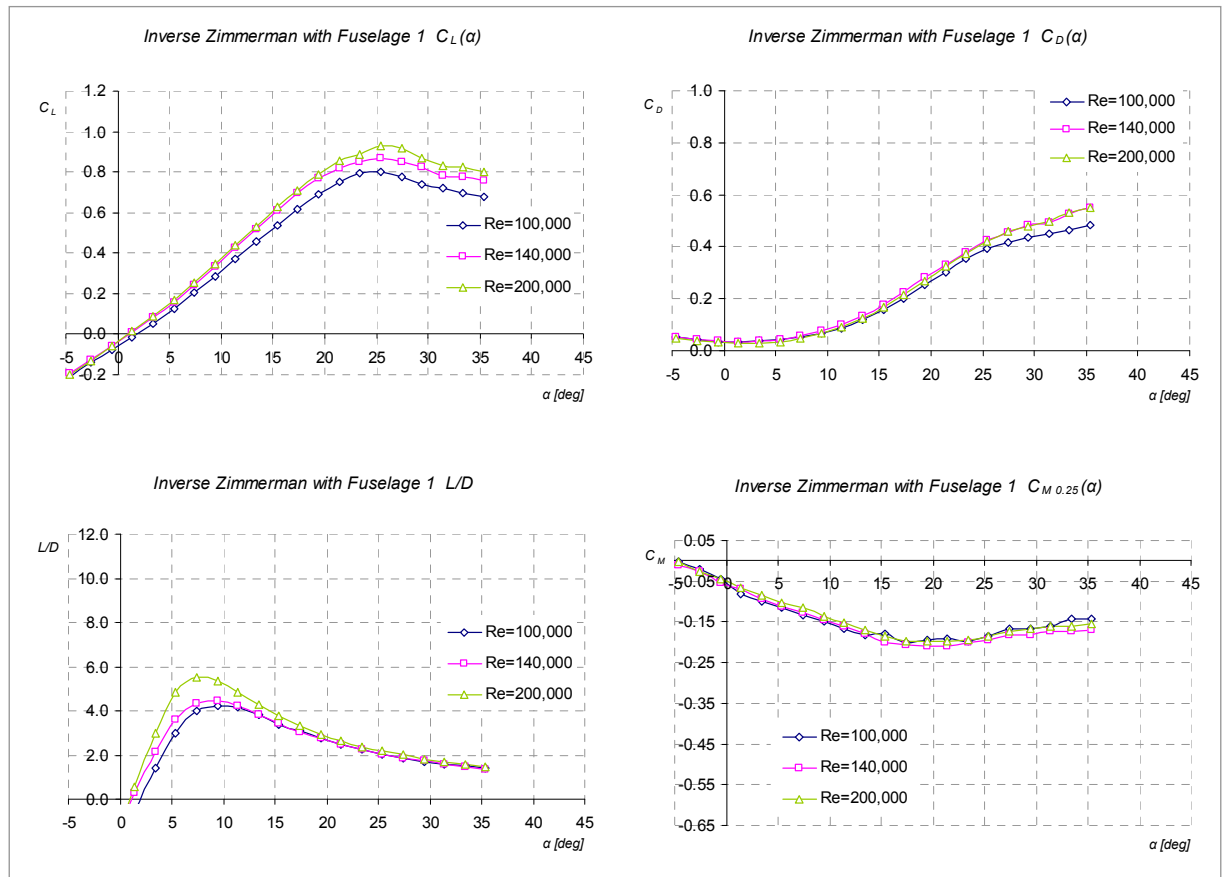
Figure 29 - Inverse Zimmerman wing with fuselage1 test results
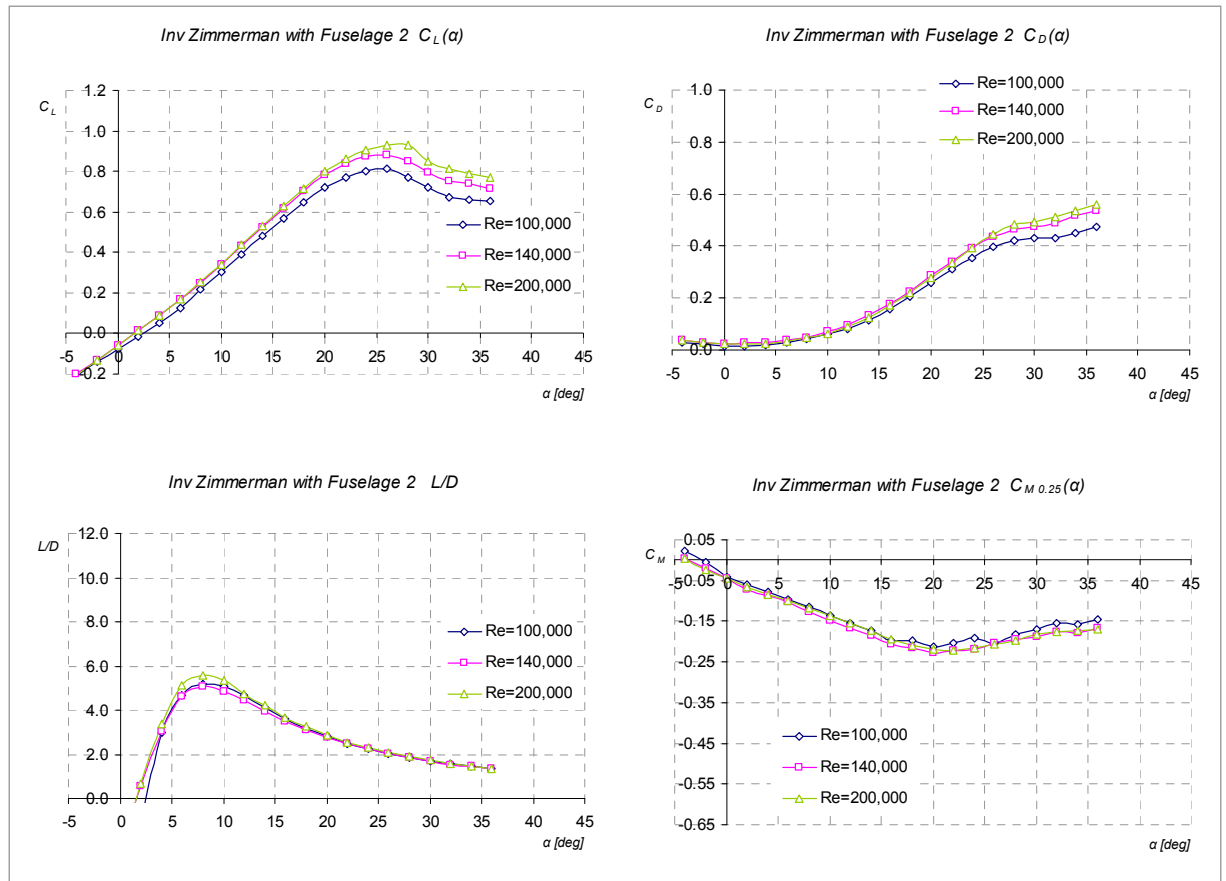
Figure 30 - Inverse Zimmerman wing with fuselage2 test results
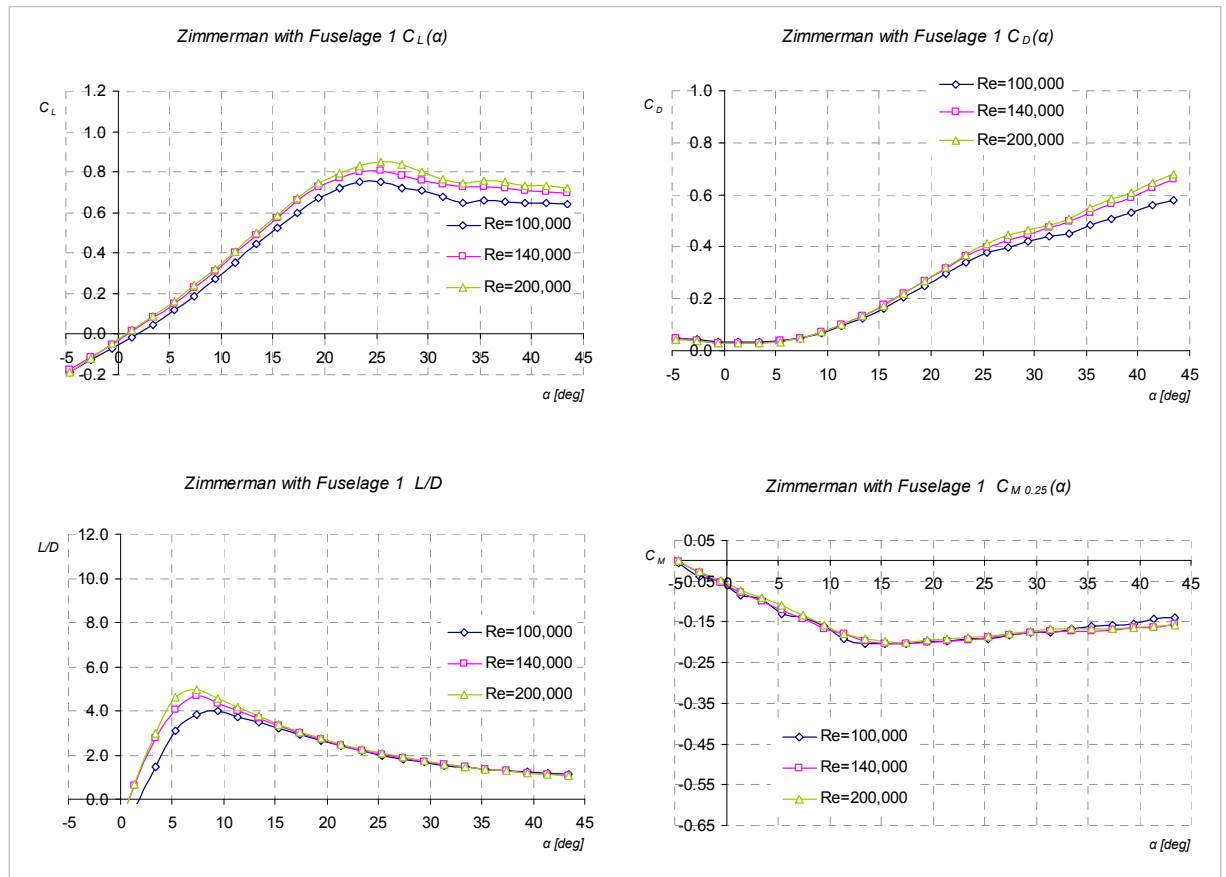
Figure 31 - Zimmerman wing with fuselage1 test results
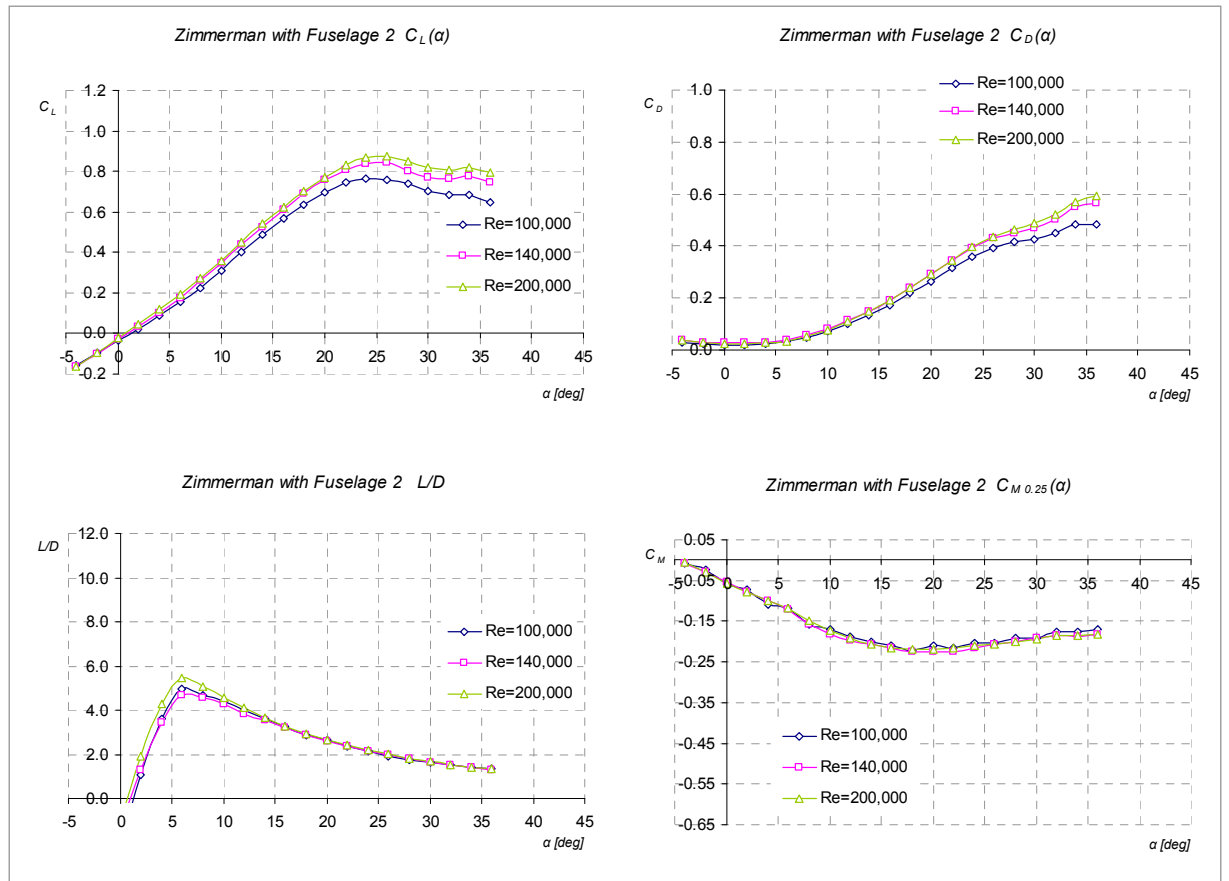
Figure 32 - Zimmerman wing with fuselage2 test results
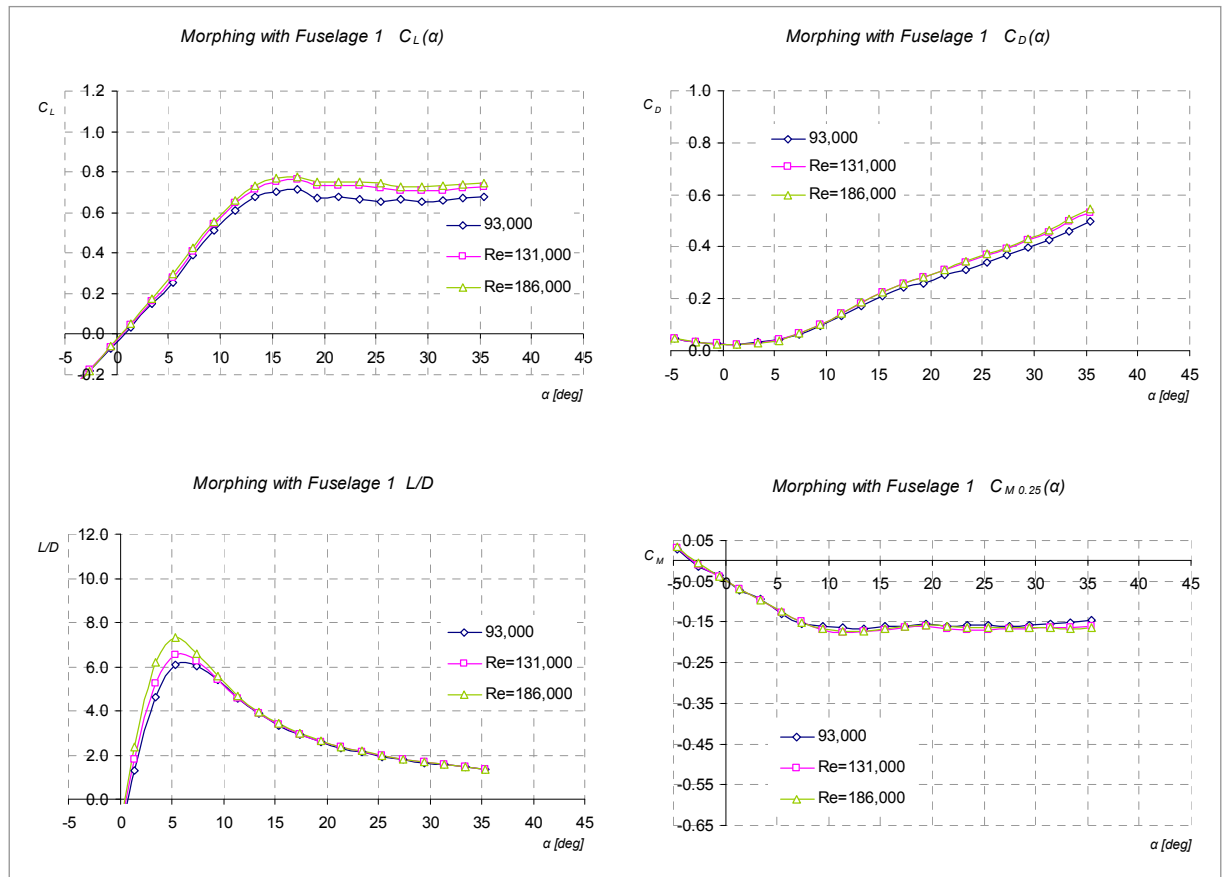
Figure 33 - Morphing wing with fuselage1 test results
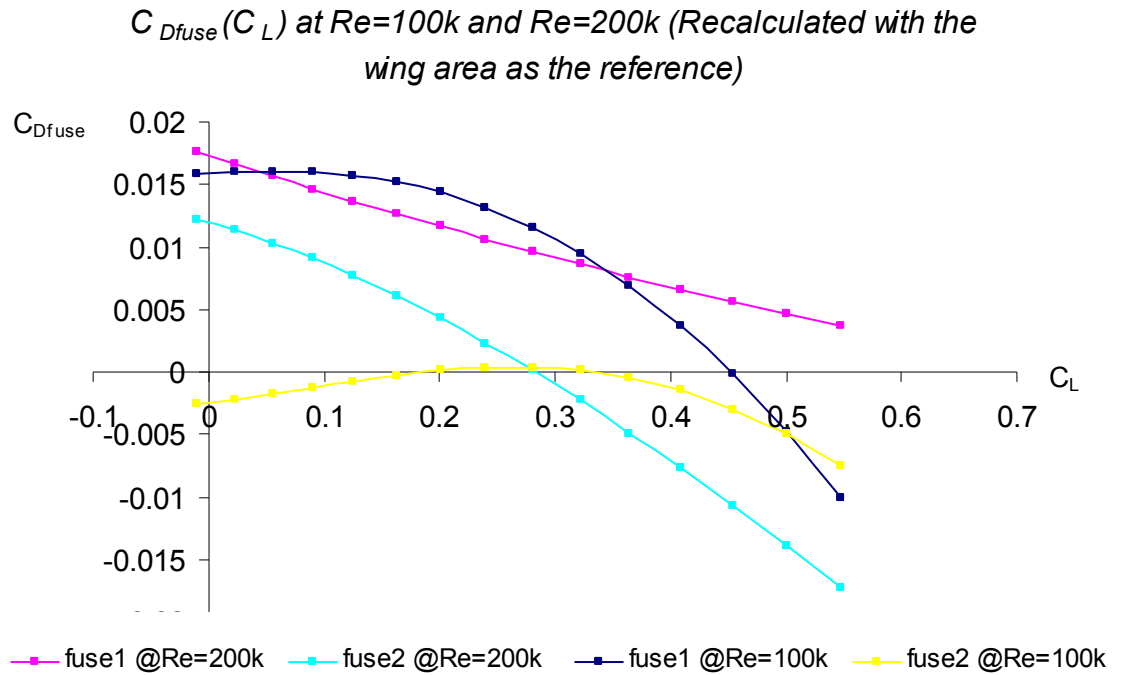
Figure 34 - Fuselage drag polars calculated as a difference from the wing+fuselage and wing only configurations
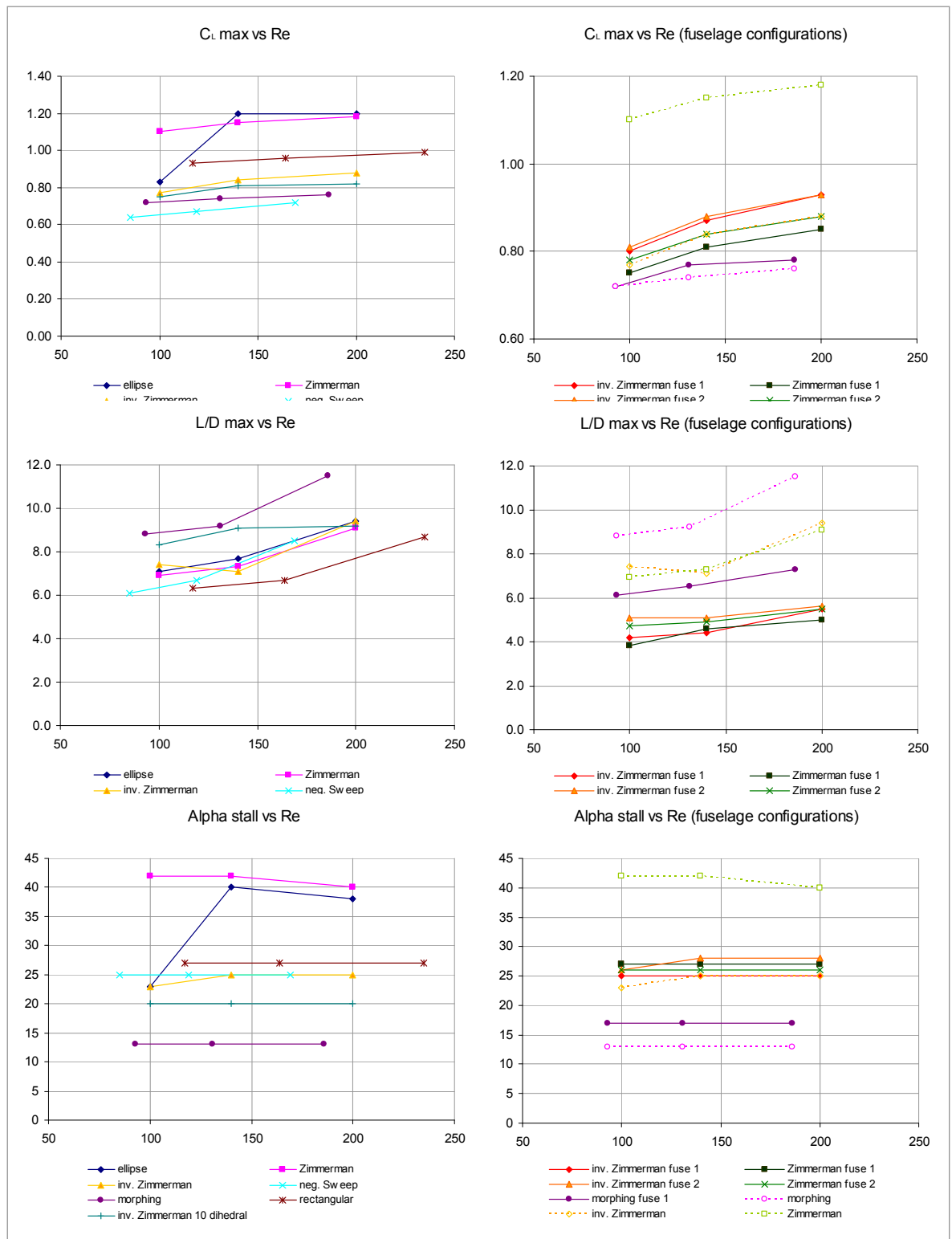
Figure 35 - Comparison of characteristics for all models

4.11 Findings, remarks and conclusions on wind tunnel testing

- As noted in [14, 15] the planform and *Re* have the most significant influence on the characteristics of the wings.

- The Elliptical and Zimmerman planforms have shown the highest C_{Lmax} of up to 1.2. This is a higher result than in [14] for similar *Re* and *AR.*

- Elliptical and Zimmerman planforms show post-stall behavior where C_L was still rising up to *α* of 36° to 40°. This was most probably due to vortical flow over the wings. This phenomenon was not present with a wing-fuselage configuration.

- The presence of the fuselage tends to increase $α_{stall}$ (if the post-stall behavior of Zimmerman wing is not taken into account). It also results in a smoother stall characteristic.

- The introduction of the dihedral increased the *L/D* (especially at lower *Re*) and reduced the $C_{M\ 0.25}$. This is in agreement with the findings of Zimmerman [13], although his experiments featured models of cambered wings with a non-linear dihedral.

- The 'negative sweep' planform performance is not satisfactory (low L/D) and therefore is not taken into account in the latter part of the project.

- The 'morphing' configuration shows a mild stall around *α=15°* with a constant value of C_L all the way to the test limit (*α=30°*). These characteristics are also shown with the presence of the fuselage. Although a detailed investigation has not been carried out, this behavior is probably caused by the vortices created at the notches on the leading edge. Tuft flow visualization has shown the presence of a strong vortex in this region of the wing.

- The 'morphing' configuration is abandoned at a later stage of the project due to mechanical complexity, which, after close investigation, turned out to be too difficult to implement in this project.

- The non-zero pitching moment coefficient at $\alpha=0°$ for all of the tests was most probably due to the interference between the model, the sting and the load cell.

- The tests of the configurations with the fuselages were inconclusive (Fig. 34). Generally the Fuse2 (triangular cross-section) had slightly better performance than Fuse1 but the polars through the range of Re were not consistent. The reference area for the drag coefficients was the frontal cross-section. The negative value of the $C_{D\,fuse}$ is caused by the way the polars were calculated. They were simply taken as the difference between the wing+fuselage configuration polars and wing only polars. Therefore negative $C_{D\,fuse}$ value was caused by the poor resolution and sensitivity of the load cell. This was especially pronounced at lower Re where the aerodynamic forces were relatively low and a very small measuring range of the load cell was used.

- The results were used later to validate the aerodynamic characteristics calculations of the low aspect ratio wings. Experimental and analytical polars proved to be in good agreement. This is described in more detail in section 5.1.

5. Performance calculation and geometry optimization

Once the wind tunnel tests were completed the validation of the results with pertinent theories could be carried out. The performance calculations were then implemented into a Genetic Algorithm (GA) to find the optimum MAV's wing geometry for given performance and mission constraints.

5.1 Theory for performance calculation

The calculation of the aerodynamic characteristics of an MAV is different from the methods used for larger aircraft. Low aspect ratio (LAR) wings and the low *Re* ($1*10^4<Re<3*10^5$) at which MAVs operate make these characteristics quite difficult to estimate. A method which has been used in [21, 22] is VLM (Vortex Lattice Method) but it did not prove to give realistic results for this study. The VLM validation tests for a rectangular plate carried out in XFLR5 [23] have shown that it significantly underpredicted the drag.

Another method, proposed by Luke [24] and used in the optimization code described in [25] also appears to underpredict drag in some cases. A numerical strip method used by Cosyn and Vierendeels [26] has good agreement with the experimental results, but requires a sophisticated CFD code and higher computational power, which is not desirable in a simple GA code, as it generates thousands of individuals and calculates their characteristics during every run.

Therefore, a method based directly on data from wind tunnel experiments, as proposed by Mueller and Torres [14, 15], was used in this project. The method was validated for higher *Re* numbers than described in the original paper using the data from wind tunnel experiments carried out at the University of Glasgow [27] which proved to be in good agreement with the analytical model, see Figs. 36, 37, 38 and 39.
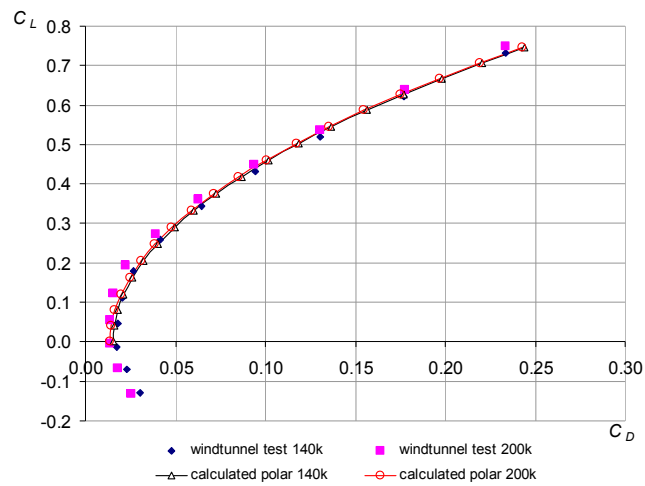
Figure 36 - Polar validation for rectangular planform wing
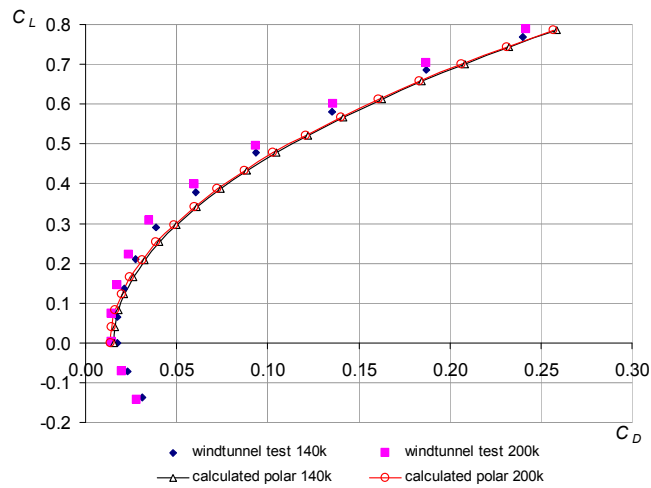
Figure 37 - Polar validation for elliptical planform wing
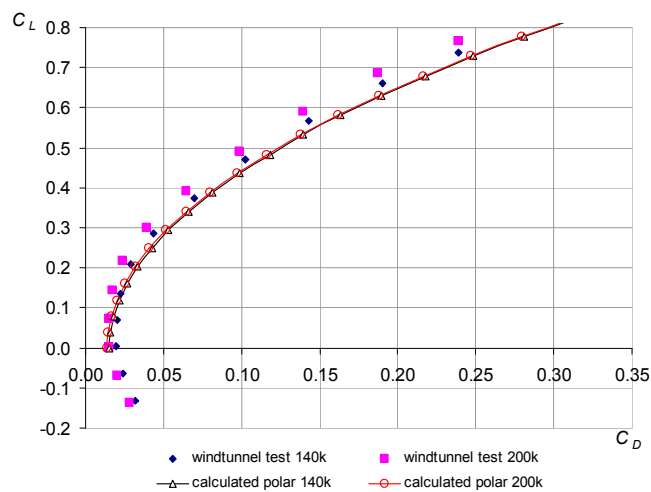
Figure 38 - Polar validation for Zimmerman planform wing
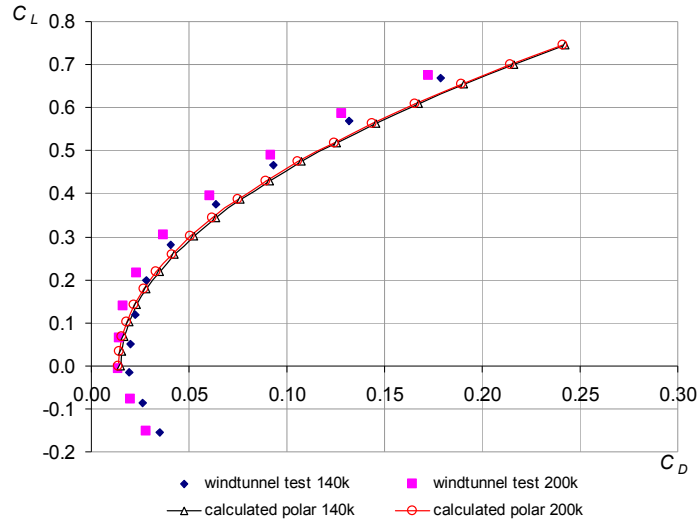
Figure 39 - Polar validation for inverse Zimmerman planform wing

In this method the wing drag coefficient is calculated from the Prandtl's Lifting Line Theory (LLT):

$$C_D = C_{D_0} + K \left[C_L \right]^2$$
(17)

In Eq. 17, *K* is the induced drag factor dependent on the wing planform and aspect ratio. C_{D0} is the drag at zero-lift. The *K* parameter is a function of *AR* and was derived from experiments in [14]. It is reproduced here in Fig. 40. These curves were also used in the optimization code. In the code the lift coefficient C_L was used as an independent variable. Currently the method implemented in the code works only for flat-plate aerofoil wings. Although there are slight discrepancies between the analytical and experimental data, the Mueller and Torres method gave by far the best agreement and therefore it was decided to use it in further calculations.

The $C_L(\alpha)$ polars were not in very good agreement with the method used by Mueller and Torres [14, 15]. The experimental lift polars had generally lower lift curve slope than the analytical ones. This was not a concern since in the calculations and optimization code the lift coefficient was used as an independent variable thus calculating $C_L(\alpha)$ polars using the leading edge suction method as in [14, 15] was not necessary. This was not further investigated in this research.
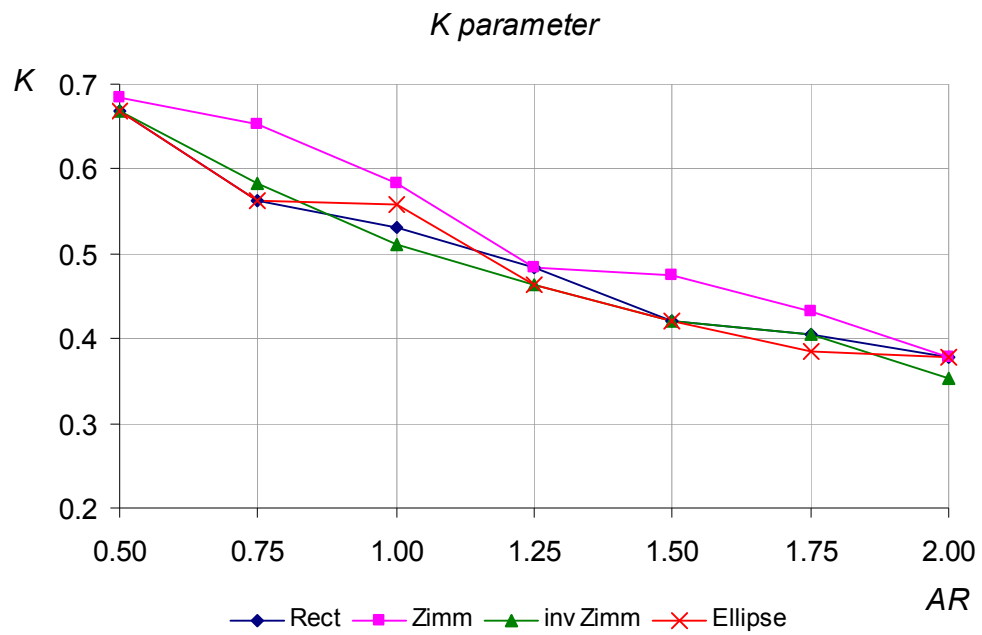
Figure 40 - *K(AR)* curves taken from [14]
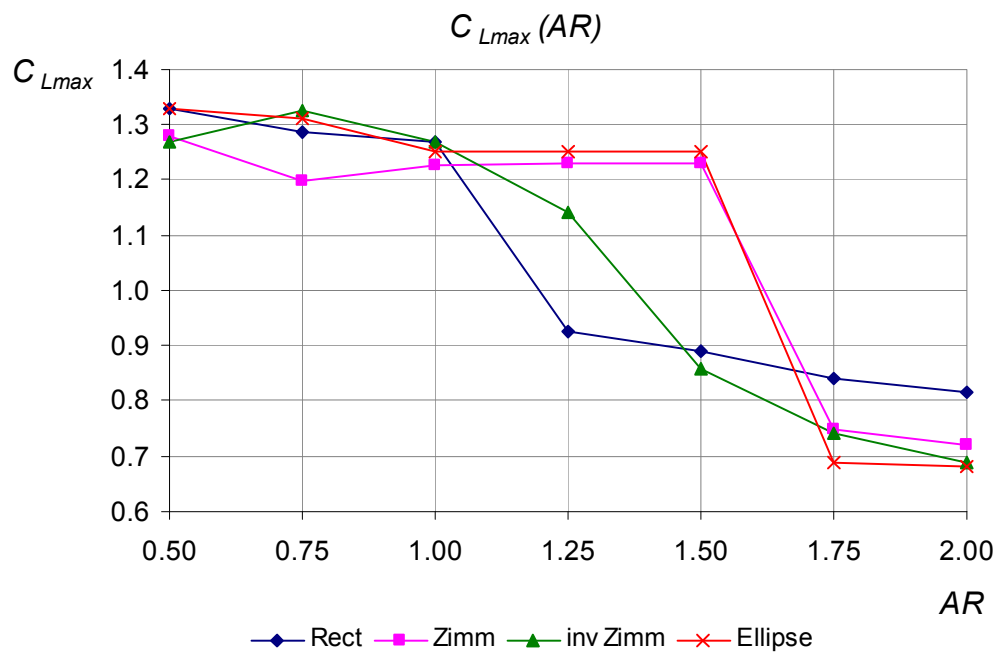
Figure 41 - C_Lmax(AR) curves taken from [14]

5.2 C_{D0} calculation

The zero-lift drag coefficient of a flat plate was calculated for a 2D case: a 3% thickness flat plate using XFLR5 aerofoil analysis module [23]. Experimental data published by Pelletier and Mueller [28] indicate that the 2D and 3D zero-lift drag coefficients (compared for cambered wings) have similar values and thus 2D data can be used for a 3D case. Figure 2 illustrates the comparison of flat and cambered plate C_{D0} as a function of *Re* and flat plate C_{D0} from different sources. Although results from numerical simulation have higher values than measured in [28], they are still in good agreement with the results of experiments carried out by the author [27] (Fig. 42).
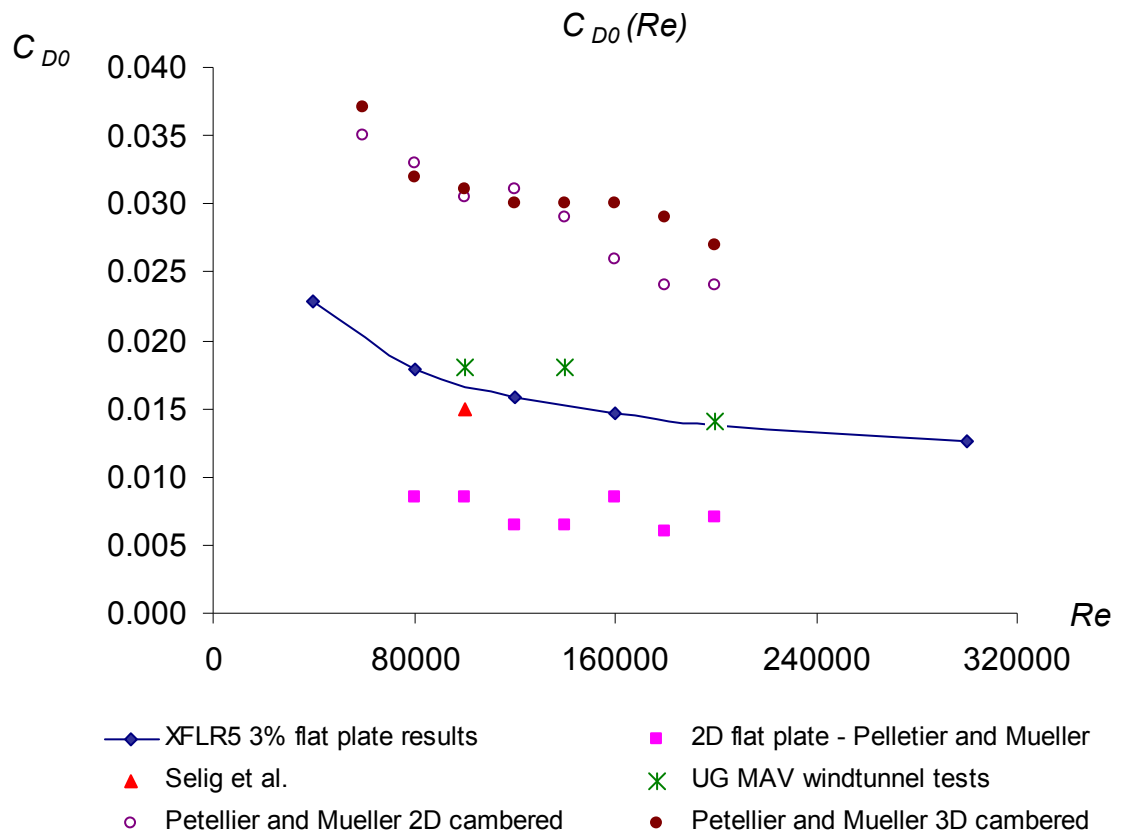
Figure 42 - C_{D0} graph

5.3 Fuselage and fin drag

Fuselage drag was evaluated for two typical fuselage shapes. As described in section 4.11, drag polars for lower *Re* numbers were inconsistent. It was decided that the polar of a rectangular fuselage at Re=200,000 will be used to simulate

additional parasite drag with fuselage cross-section taken as the reference area. The fuselage length is assumed to be the same as the wing root chord. The fuselage polar derived from wind tunnel testing which was used in the code is shown in Fig. 43.
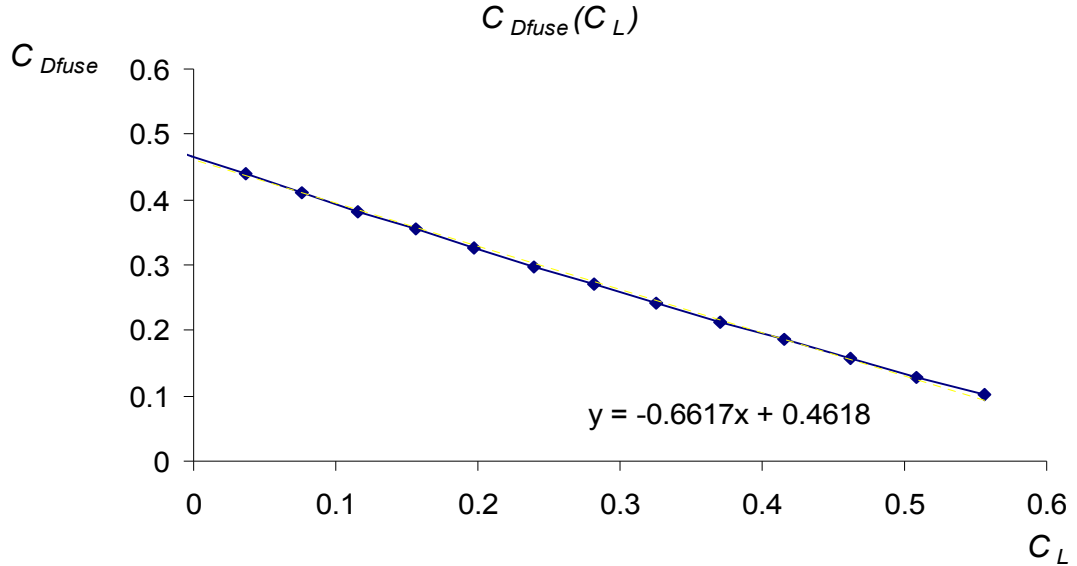
Figure 43 - Fuselage drag polar used in the optimization code

For calculation of the fin drag a coefficient for a flat plate zero-lift drag is used. The fin surface calculation for a given design is based on the vertical-stabilizer volume coefficient value (0.06) suggested by Cosyn and Vierendeels [29]. This is also consistent with the vertical fin volume coefficient used in the authors' previous MAV design [5]. This complete aerodynamic model has been implemented in the optimization code. The main draw-back of using the described aerodynamic model is that currently there is no possibility of modelling a cambered wing. This might be possible in the future with some additional wind-tunnel or CFD testing. Nevertheless, the parameters which are most important for a LAR wing performance are the planform, aspect ratio and the *Re* [14, 15] and therefore using a flat-plate aerofoil in the modelling is not significantly detrimental to the method.

5.4 Optimization overview

As a part of this research the optimization of the MAV was carried out. It was thought to be a simple and robust tool that can help the designer with the selection of MAV geometry parameters based on the initial mission and performance

requirements. This is a far less complex optimization method (Fig. 44) than the one presented in [25, 30] and some tasks such as selecting the propulsion system, correct position of the centre of gravity, housing of the equipment etc. are left to the designer. This approach, although simple and requiring some level of expertise in MAVs, is more 'fool-proof' and provides good insight into the aircraft design process. Although some codes have additional design constraints within the optimization like CG position or static stability margin, the realistic formulation of these can be very difficult. Hence it is better if left for evaluation by the designer than the computer code. MAVs are a very specific type of aircraft and some equipment components can be placed in rather 'unusual' places (embedded in the wing, fins) or even be used as part of the airframe structure [31]. Tasks such as propulsion selection can be done easily even without having special expertise with help of available software like MotoCalc [32]. The designer's creativity is virtually unlimited and can lead to very surprising ideas whereas computer can only be as good as its code permits.
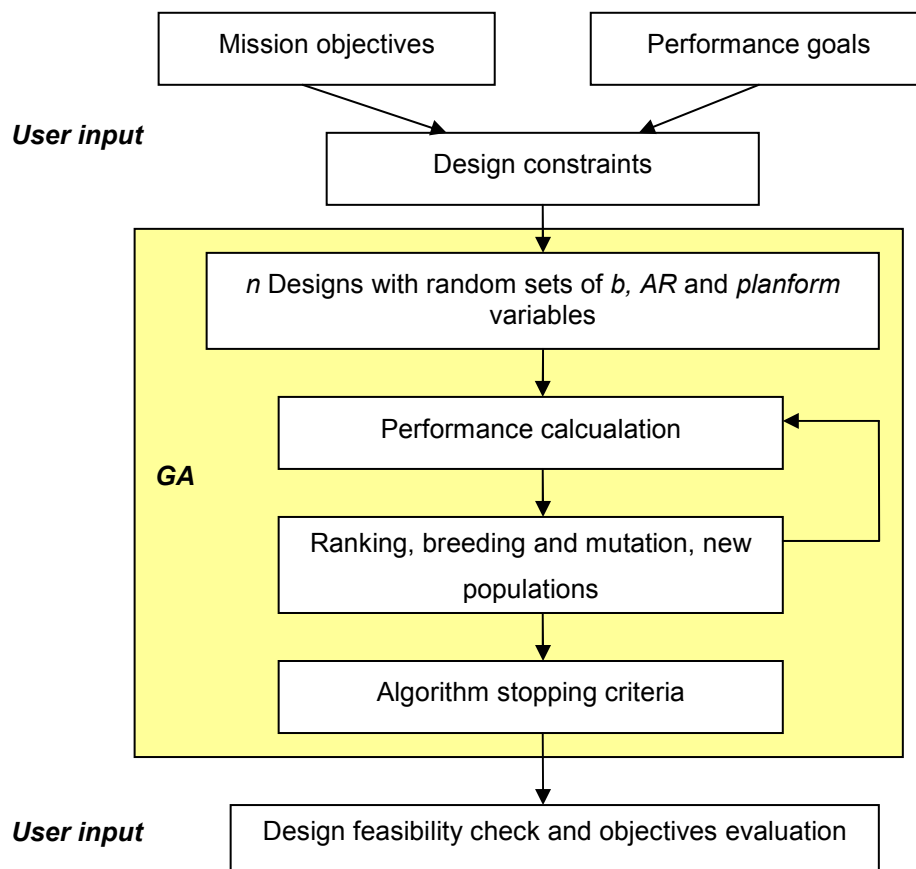
Figure 44 - Optimization procedure flow chart

Genetic algorithms were first mentioned in the 1960s and since then have been applied to a number of optimization problems, including aircraft design optimization [30]. These algorithms try to mimic Darwin's theory of evolution. After initial generation of a random population of parametric designs consisting of *n* individuals, each of them is evaluated for their *'fitness'. Fitness* is a function measuring how a certain individual fulfills the requirements of the design. The part of the population with the highest *fitness* is most likely to 'reproduce', which means that their parameters will be mixed to produce a new generation of individuals. This process is repeated until the population becomes uniform in fitness and can no longer be improved thus representing an optimal design. During the process some of the individuals are mutated to produce random sets of design parameters which assure that the code will eventually find the global rather than a local optimum. Methods of reproduction can vary as well as stopping criteria and individuals' evaluation. More detail on GA and their implementation in aircraft design can be found in [30].

Optimization using GAs has been successfully used in other similar projects [21, 25, 30, 33, 34]. One interesting feature is that GAs can optimize designs in respect to both continuous and discrete variables. This is especially useful for this project as the performance calculation model mentioned above is based on experimentally-derived induced drag factor *K* for each of the planforms – as a result, the planform will be a discrete design parameter. The code for the optimization has been developed in MATLAB® and uses its standard GA toolbox.

5.5 Optimization code description

The code was designed to optimize the wing geometry of the MAV as this has the most significant impact on its performance. The fuselage geometry is assumed to be determined by the user for the housing of all the components and its cross-section is later used by the code to calculate the fuselage drag. The code has 3 independent variables:

- Wingspan *(b)*
- Aspect Ratio *(AR)*
- Wing planform type *(planform)*

On the initiation of the code a panel appears to input all the required data (Figure 45).

Figure 45 - Input panel of the optimization code

The wingspan and aspect ratio are continuous variables whereas the planform type is a discrete variable. The code features four planform types: elliptical, Zimmerman, inverse Zimmerman and Rectangular. The optimization is aimed at finding the best wing geometry within the constraint set specified by the user:

- Minimum and maximum wingspan
- Minimum and maximum aspect ratio
- Maximum allowable stall speed
- Design cruise speed
- Fuselage width and height
- Equipment weight

The user may also narrow down the selection range of the planforms and select the population size of each generation. With all the initial data input the code uses MATLAB GA toolbox to generate a random population of designs and calculates performance of each of them. With known performance, fitness can be calculated, and based on its value the code generates the next generation of designs. The scheme of calculating the performance of the MAV designs is presented below. The source code from the m-files can be found in the Appendix (section 11.1).

With randomly generated geometry parameters (*b, AR, planform*) the *S* and *S$_{fuse}$* may be calculated:

$$S = \frac{b^2}{AR} \tag{18}$$

$$S_{fuse} = f_h f_w \tag{19}$$

The m_{tow} (Eq. 20) is calculated by the code as a sum of the user-specified equipment weight (that is propulsion, control and payload) and structure weight which is automatically estimated. The structure weight estimation is based on the aircraft surface and the assumption that the MAV is made of depron foam reinforced with composite. This is a purely empirical equation based on author's previous experience with MAV design [5] and proved to work well with this code. The a_d is the density of a 6mm depron foam sheet (0.26kg/m^2) and the coefficients of 1.5 and 2 are empirically derived factors for the weight of a depron structure reinforced with composite material. The fuselage is assumed to have the length of the root chord.

$$m_{tow} = m_{equipment} + 1.5 S a_d + 2 \cdot (2 S_{fuse} + 2 c_{root} f_h + c_{root} f_w) a_d \tag{20}$$

The planform is prescribed to the individual (randomly or as the effect of breeding/mutation). The $K(AR)$ characteristics were implemented into the code and are interpolated from the curves (Fig. 40). Similarly, $C_{Lmax}(AR)$ curves taken from [14] (Fig. 41) were implemented in the code for finding the C_{Lmax} of the given configuration and calculation of the stall speed:

$$V_{min} = \sqrt{\frac{2 m_{tow} g}{\rho S C_{L\max}}} \tag{21}$$

The C_L is treated as an independent variable. For the C_L range from 0 to C_{Lmax} with step of 0.005 the value of level flight airspeed V is calculated. Then for each V, Re of the wing is calculated so that the flat plate C_{D0} can be calculated using the function derived from the $C_{D0}(Re)$ curve (Figure 42):

$$C_{D0} = 0.5268 \, \mathrm{Re}^{-0.2982} \tag{22}$$

At this point the parasite drag of the fuselage and fin can be calculated. Fuselage drag coefficient is expressed as a function interpolated from the curve which was derived from the wind tunnel tests (Fig. 43):

$$C_{Dfuse} = -0.6617 C_L + 0.4618 \qquad (23)$$

The fin drag coefficient is assumed to be the same as the flat plate for given *Re*. Firstly, the fin surface, S_{fin}, is calculated on the assumption that the vertical tail volume coefficient, C_{vt}, for fixed wing, tailless MAVs has a value of ~0.06 (Eq. 24).

$$S_v = \frac{C_{vt} \bar{c} S}{l_v} \qquad (24)$$

The vertical tail arm is the distance from the wing AC to the tail AC. The tail AC is assumed to be *0.1$\bar{c}$* in front of the root chord's trailing edge. The fin is modeled as a square planform; therefore its *Re* is given by:

$$\mathrm{Re}_{fin} = \frac{V \sqrt{S_{fin}}}{\nu} \qquad (25)$$

All the drag components are now known and therefore the $C_L(C_D)$ characteristic can be calculated (Eq. 26). Both drag coefficients are normalized to values with the wing area taken as a reference area:

$$C_D = C_{D_0} + K(C_L)^2 + C_{Dfuse}\left(\frac{S_{fuse}}{S}\right) + C_{Dfin}\left(\frac{S_{fin}}{S}\right) \qquad (26)$$

With the $C_L(C_D)$ characteristic known, the maximum value of *L/D* can be found. The fitness function *FF* (Eq. 27), upon which individuals are rated, is designed to maximize the *L/D* at the given design cruise speed while keeping the stall speed under the specified limit. This provides the best range (and thus best operating radius) under the given mission and design constraints.

$$FF = -\left(L/D\right)_{max} + A \cdot \left|V_{opt} - V_{cruise}\right| + B \cdot stall\_cond^{2} \qquad (27)$$

$$stall\_cond = \begin{cases} 0 & if \quad V_{min} \leq V_{stall} \\ V_{min} - V_{stall} & if \quad V_{min} > V_{stall} \end{cases} \qquad (28)$$

where:

V_{min} – stall speed calculated from the particular individual,

V_{stall} – maximum design stall speed limit,

V_{opt} – optimum (L/D_{max}) speed of the particular individual,

V_{cruise} – design cruise speed,

A, B – empirically selected coefficients for a desired balance between the terms. In the final version of the code *A=0.5* and *B=1.*

The default GA toolbox in MATLAB is designed to minimize the given fitness function, hence the minus sign in front of the *L/D* term in (Eq. 27).
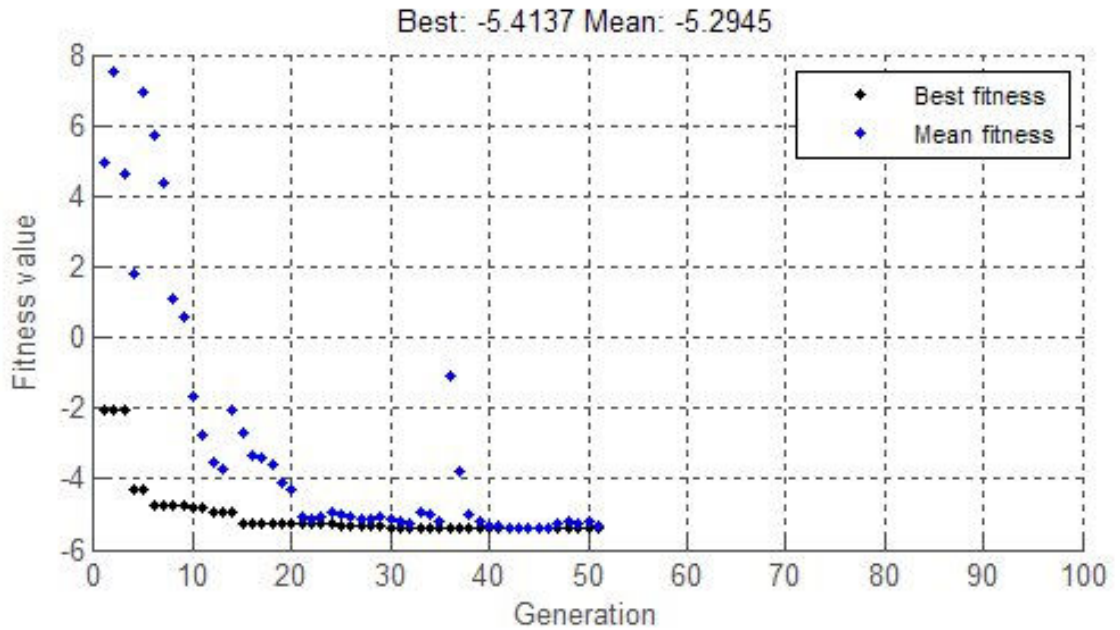
Figure 46 - GA convergence plot

While the code runs, convergence is displayed showing how the *FF* value varies with generations (Fig. 46). After finding the optimal design, its parameters and performance are displayed (Fig. 49) and written to an MS Excel file.

Because the GA optimization gives a different result each time it is executed, it is important to select the number of individuals in each generation so that good repeatability is achieved for minimal computational time. In this case a reasonable time of around 5 minutes has been achieved on a workstation with AMD® Opteron 1200 CPU with each generation consisting of 100 individuals. On slower computers computational times are similar (around 6 minutes). It takes about 50-60 generations for the code to converge to a solution (to a point at which no more improvement occurs).

6. Detailed design and prototype manufacturing

6.1 Detailed design

With the main geometry parameters set, the next step was to carry out the detailed design and manufacturing of the prototype. Fitting of the components inside the fuselage was also done before while estimating the fuselage cross-section (Figure 48, section 5). Now with fixed wing geometry a precise fit of the equipment inside the fuselage was done. Next, precise evaluation of the fuselage position with respect to the wing was carried out. This was important so that no ballast would have to be added later in order to achieve proper CG position. Final re-evaluation of the equipment was done as the actual components were bought at this stage and some corrections had to be made. Nevertheless, with the optimization code the recalculation of the optimal geometry was fast and straightforward. The final weight breakdown is shown in the Table 6 and Fig. 47.

Table 6 - Bumble Bee's final weight breakdown

	m [g]
misc	10
motor	20
battery	62
speed controler	10
reciver	14
servos (3)	15
propeller	4
camera system	50
GPS	13
IR stabilization system	22
camera battery	10
additional electronic equipment (GPS datalink)	30
Airframe	45
TOTAL	**305**
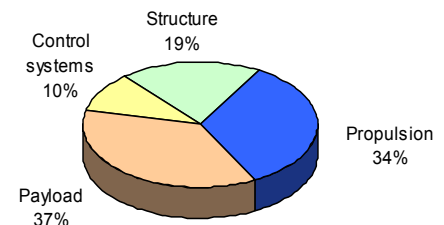
Figure 47 - BumbleBee MAV weight breakdown

The optimization code found the best solution to be a configuration with an elliptical wing, *b=381*mm and *AR=1.61* and the *L/D$_{max}$* of 5.74. A configuration with the inverse Zimmerman planform wing was also investigated. It was found that with the *L/D$_{max}$* of 5.66 (thus ~1.5% less than the configuration with an elliptical wing and at practically the same *m$_{tow}$*) it has a smaller wingspan of 376mm.
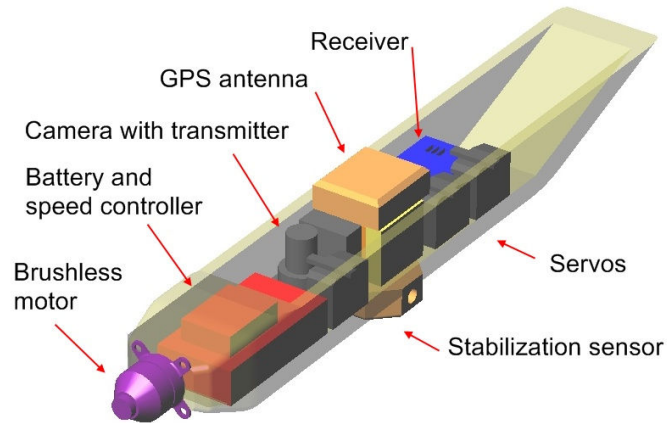
Figure 48 - Fuselage model investigated for housing the equipment

Further analysis showed that because of the difference in position of the aerodynamic centre, the inverse Zimmerman configuration MAV can be also ~15mm shorter. The position of the AC was evaluated using the A.C. Calculator software by Martin Hepperle [35]. Based on predictions carried out in MotoCalc [32] both configurations would achieve 20+ minute endurance with the chosen propulsion system. Therefore it was decided to carry on with the Bumble-Bee MAV design in the configuration with the inverse Zimmerman wing planform. Final performance, calculated as the output of the optimization code, is shown in Fig. 49.
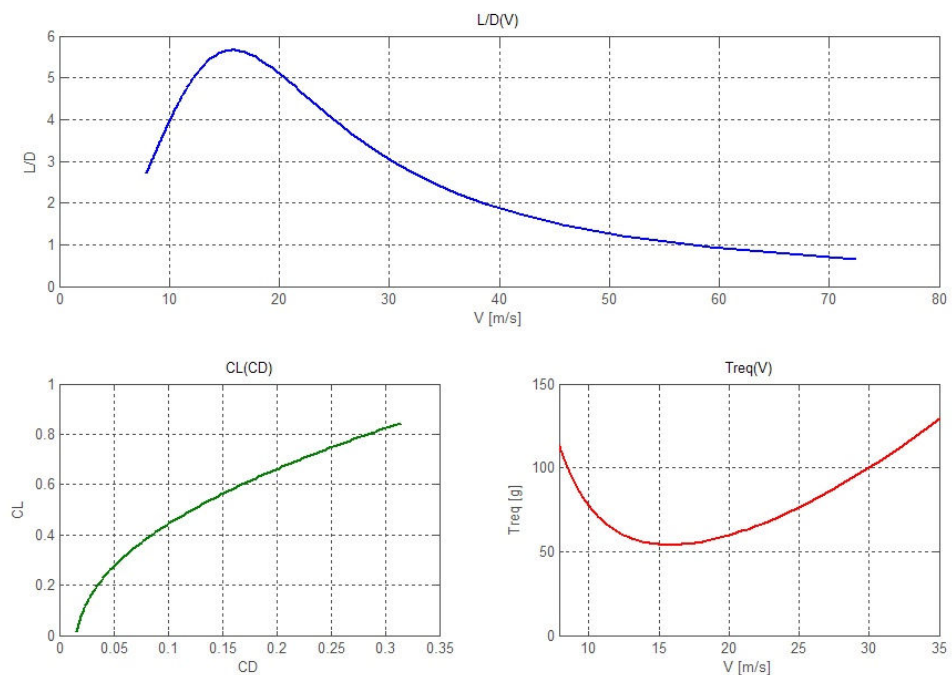
Figure 49 - BumbleBee performance graphs (final prototype configuration)

The final propulsion system selected for BumbleBee consisted of a Hacker A10-9L brushless electric motor, 1320mAh LiPo battery and a Hacker X7 10A speed controller with a generic 6x4 propeller. Performance of this propulsion set was evaluated in MotoCalc. The analyses have shown that this propulsion system would allow for 23 minutes of flight at the 85% throttle setting which provides thrust required for level flight at design cruise velocity. In level flight engine thrust must be equal to the drag of the MAV:

$$T_{req} = D \tag{29}$$

hence the thrust required is:

$$T_{req} = \frac{m_{tow}}{L/D} \tag{30}$$

In Eq. 29 the thrust is expressed in the units of m_{tow}. In the graph derived from the MotoCalc software (Fig. 50) it is shown in grams.
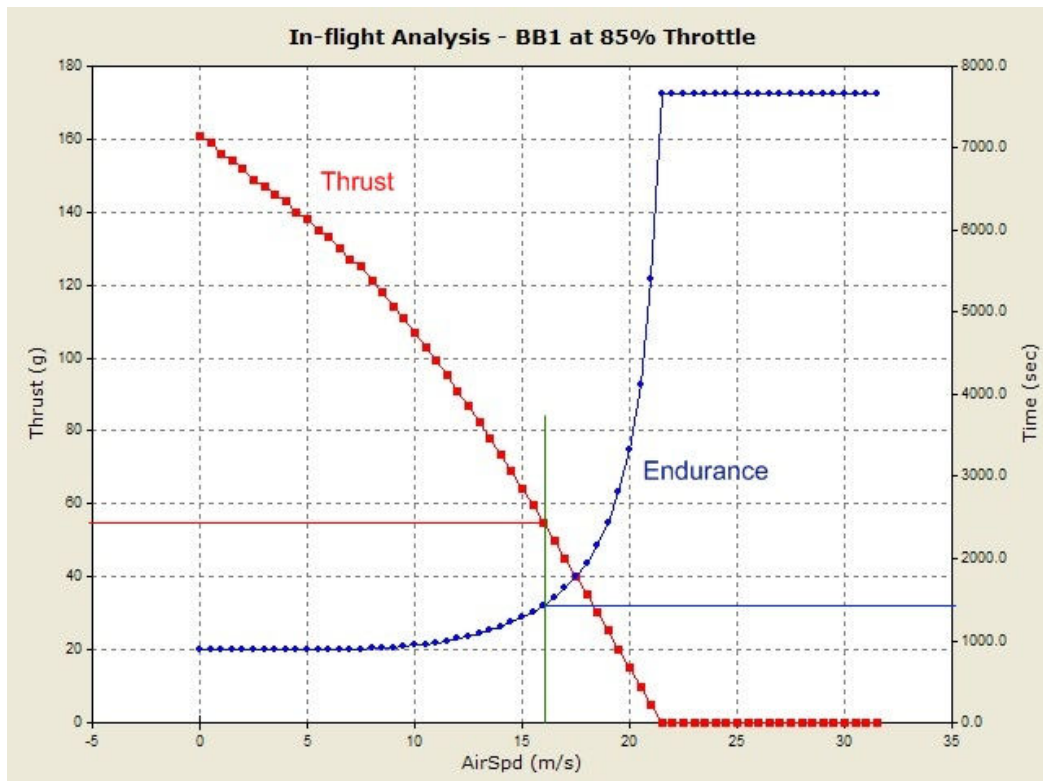
Figure 50 - MotoCalc performance graph of the final propulsion system

The task of evaluation of space inside the fuselage and 'virtual fitting' of the equipment components were carried out in Alibre Xpress® 3D parametric CAD (Fig. 51, 52) which saved a considerable amount of time compared to performing them in a 2D CAD environment. All the equipment elements were given certain density so that they were simulated as a uniform body of a given shape and weight. Although this was a simplification it did not have any significant negative impact on the manufacturing of the MAV prototype.
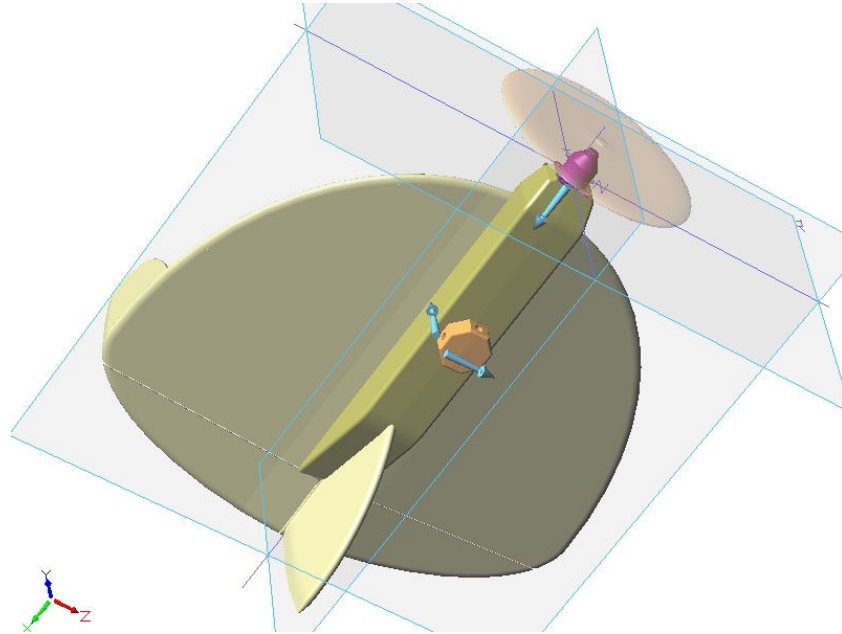
Figure 51 - BumbleBee design in Alibre Xpress® CAD
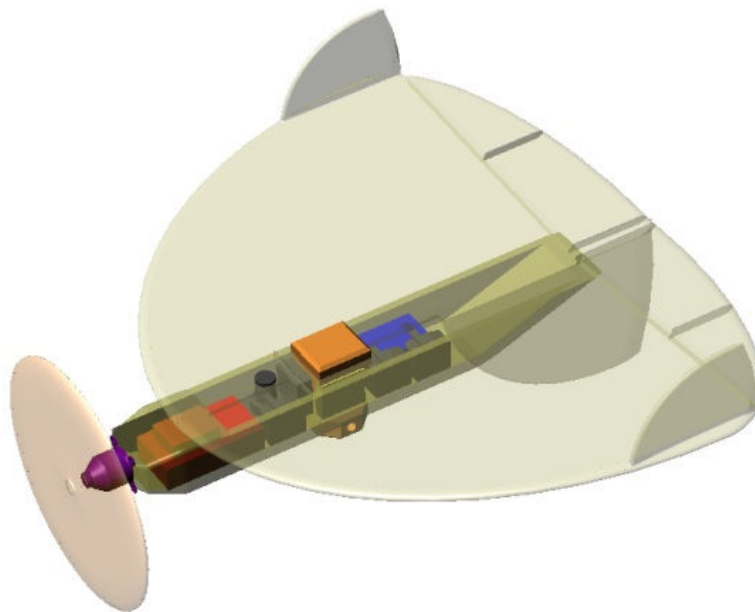
Figure 52 - Final BumbleBee design modeled in Alibre Xpress®

Rearrangement of equipment is always possible and some elements such as wiring were hard to simulate during this analysis due to the limited assembly part count in Alibre Xpress. The flight ready MAV with all the pieces of equipment fitted, had a CG position 2mm from the calculated point, but a slight shift of the LiPo battery pack solved this problem and placed the CG exactly at 15% of MAC. Final parameters of the BumbleBee are given in Table 7. A 3-view drawing of the MAV can be found in the Appendix (section 11.2).

Table 7 - Final parameters of the BumbleBee prototype

Wingspan	376 mm
Aspect Ratio	1.52
Wing area	0.093 m^2
Weight	305 g
Endurance*	23.5 min
L/D$_{max}$	5.66
Wing planform	Inverted Zimmerman

calculated value

The manufacturing was to be done using typical RC modeling techniques, mainly 6mm depron foam and Kevlar composite reinforcement. Firstly, the depron structure was made and then the reinforcement made of Kevlar/epoxy composite was added at the leading edges, the front section of the fuselage (inside and outside), along the bottom of the fuselage (Fig. 55), on the fin and at the fuselage-fin attachment (Fig. 56). A glassfibre/epoxy external wingspar (on top and bottom of the wing) was added to the wing along the maximum wingspan for stiffness. Winglets and top hatch were also made of two layers of Kevlar/glass (Fig. 54). The winglets were then inserted into two tight notches cut on the wings so they could be detached for transport. The Kevlar cloth used was 61g/m^2, the glass cloth was 50g/m^2. Use of Kevlar was dictated mainly because of its high strength/weight ratio and ease of application. Carbon elements were not used as it was found that occasionally they may cause interference and reduce the range of the RC system.
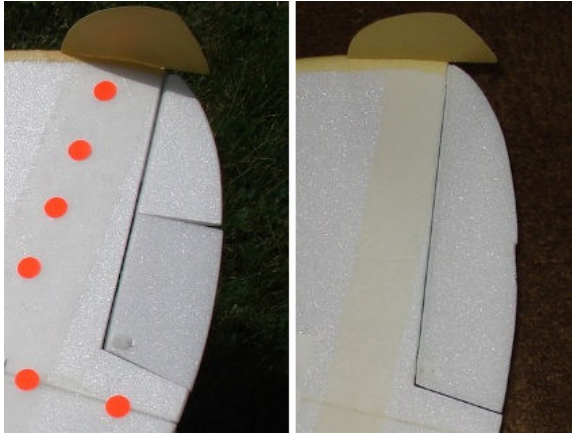
Figure 53 - Control surfaces on the 1st (right photo) and the 2nd (left photo) prototype

Figure 55 - Front fuselage detail with Kevlar reinforcement

Figure 54 - Winglet detail
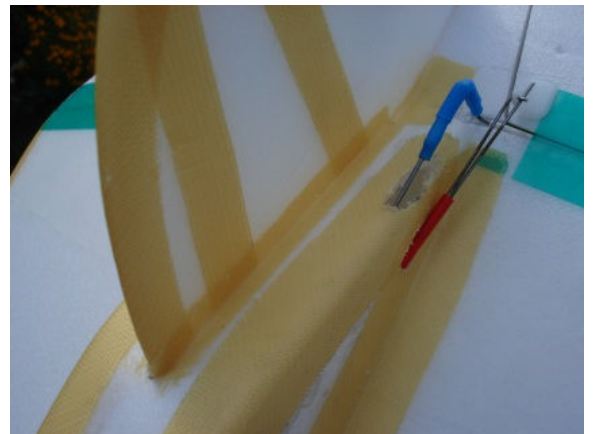
Figure 56 - Fin-fuselage joint detail

The control surfaces were attached to the servos with 1mm steel pushrods. Initially four control surfaces were used (two ailerons and two elevators – Fig. 53) as needed by the stabilization system. Since it was found later that the stabilization system was not necessary (see section 7.1), the second prototype had only two elevons with an aileron-elevator mixing function programmed in the transmitter. This system was less complicated and of smaller weight. It also proved to have better control characteristics in flight (see section 7.1). The finished prototype weighed 308g; 3g more than designed. The orange dots on the wings seen in Fig. 57 and Fig. 58 were added for top/bottom recognition but proved to be too small to be seen from a distance. For future reference, a single coloured top or bottom surface of the MAV would be better suited to the purpose.

The electric motor was attached using two bolts to a 1.5mm Kevlar former which was glued to the reinforced front fuselage with epoxy. The propeller was attached to the motor using a 'prop saver' system (Fig. 55). It allowed for belly-landings without any damage to the propeller.
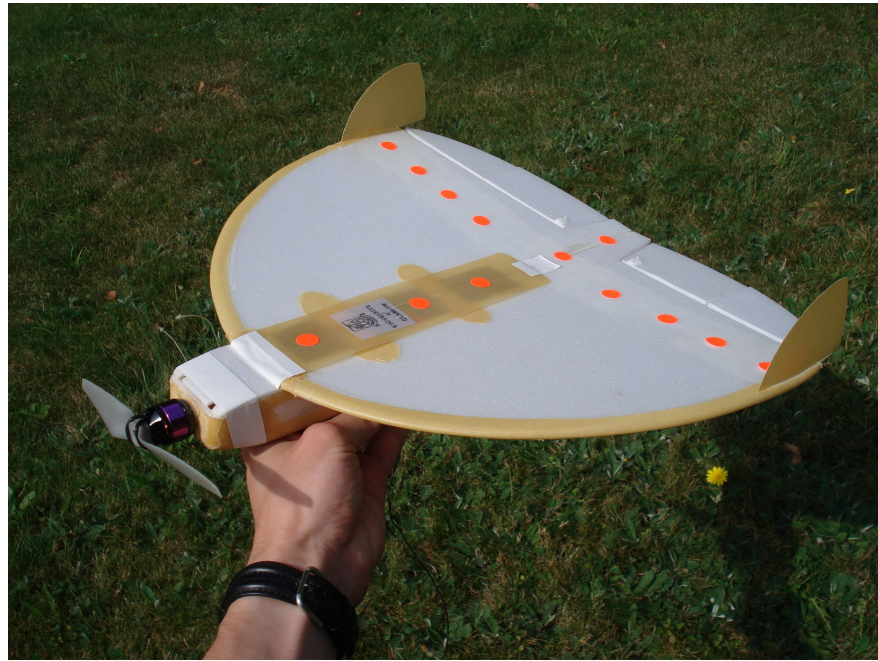
Figure 57 - The BumbleBee MAV

Figure 58 - The BumbleBee MAV – control surfaces

7. Flight testing

The last stage of the project was flight testing of the prototype with an on-board camera and GPS so that the performance could be evaluated later on. Although the GPS gives only position in time relative to earth and only very rough estimation of performance can be made, given the project budget it was the only feasible option. In the future a more advanced system with an airspeed sensor (such as Pitot tube) could be applied to verify the performance in greater detail. All the flight testing has been carried out by the author.

7.1 First test flights and assessment of handling qualities

Generally the tailless configuration is relatively tricky to fly unless properly trimmed and balanced. Therefore the first series of flight tests was carried out without the GPS, IR stabilization system and camera onboard to reduce the wing loading. This has a positive influence on the aircraft performance, especially stall speed and climb rate, which in effect allows the pilot to handle a critical situation should one arise. These flights were aimed at finding the correct CG position, electric motor inclination and allowing the pilot to become familiar with the handling qualities.

Flights were successful. They had shown very gentle stall characteristics which were expected based on previous experience [5]. The hand launch presented no problems and a simple hand-toss was sufficient to launch the MAV, which immediately continued into a 20°-30° climb. No CG adjustments were necessary and only slight increase of negative inclination of the motor was needed as the MAV had a tendency to pitch-up when full power was applied. After this minor correction the plane handling was good and did not require any special attention. The control surfaces divided into elevator and ailerons (section 6) were much less effective at low speeds. This was not a problem in roll axis but the elevator did not provide enough control authority for a flare during landing. After a few flights it was confirmed that it is better to land the MAV at slightly higher speed but at a shallower angle. The structure of the BumbleBee was robust enough and these landings did not cause any damage.

The longitudinal and lateral stability was good. In general, handling qualities were much better than initially anticipated. The author's previous experience with MAVs [5] had shown fair handling at best, and although it was not a problem for an experienced RC pilot, attention had to be kept throughout all the maneuvers. In the case of BumbleBee the addition of dihedral positively affected the aircraft, resulting in much better handling than the DART MAV [5]. In total 15 flight sorties were carried out. A video from first flight is recorded on the CD attached to this thesis.

When testing video and GPS it was found out that the extra battery runs out extremely quickly. After careful examination, it turned out that the camera draws much more current than originally anticipated and therefore requires a larger battery. On the other hand, the stability characteristics proved better than originally anticipated and the IR stabilization was not needed and instead a higher-capacity battery could be used. In this way the m_{tow} could be kept unchanged and no major redesign was necessary. Given the limited time for testing the prototype, it was decided to hold this configuration.

Figure 59 - BumbleBee in flight

Before flying with the valuable equipment, 10 test flights were carried out with ballast (Fig. 60), firstly simulating half and later the full additional weight of the extra battery, camera and GPS systems. As expected, with ~25% (half ballast) and ~50% (full ballast) increase of the wing loading the MAV was flying faster and the stall and landing speeds also became higher. Still, the fully ballasted MAV presented no problems with the hand launch although the initial climb-out was considerably shallower (around 10°) until the BumbleBee gathered more airspeed.

While performing a gentle turn, during one of the flights with ballast the MAV entered a shallow dive from which it could not be brought out of, as it did not respond to elevator commands. It hit the ground at high speed which resulted in a cracked fuselage. A careful examination of the equipment after the crash revealed that a jammed elevator servo was the direct cause. After this incident a second prototype was built (section 6), this time with elevons instead of split ailerons and elevator control surfaces as the stabilization system was no longer to be used (see section 6.1). Apart from this, no major changes were made.

Figure 60 - Ballast (half equipment weight) attached to the MAV's belly.

The second prototype had all the good handling characteristics with significantly increased elevator control authority, which resulted in ability to land at lower speeds. Although the net control surface area was the same as before, both roll and pitch control authority was much better at lower speeds. In order not to increase the aircraft control input sensitivity at cruise, an EXPO function in the RC transmitter was used. This allowed non-linear servo response to the pilot's inputs,

i.e. less deflection for small and medium inputs while still allowing full deflection of the control surface at the full travel of the transmitter's stick.

7.2 Flight tests with on-board equipment

After the initial test flights, which allowed the author to fine-tune the MAV and become familiar with its handling, the GPS and camera equipment was mounted to finally test and assess the feasibility of the system.

One shortcoming, noticed during the test flights, was the range of the RC system. This was mainly due to the transmitter used (Hitec Optic 6). The same configuration tested with a different transmitter (Graupner MC-20) showed a considerably better range and tests indicated that coverage of over 1km could be achieved.

The camera system worked excellently and the frame rate/resolution was only restricted by the power of the PC used for grabbing the images. Three different camera positions were evaluated: directed down-front, directed to the front on top of the MAV and directed to the front on the side of the MAV. The first (1 in Fig. 61) gave the best view of the patrolled area but did not always provide (depending on angle of attack) a view of the horizon and therefore could not have been used in a system controlled with the 'pilot-through-vision' method as the camera could not be installed in the bottom of the fuselage at an angle giving better view on the horizon due to fuselage volume and CG constraints. The camera looking from the top (2 in Fig. 61) of the MAV did not provide sufficient ground coverage. The forward looking camera mounted on the side of the fuselage (looking through a prism, 3 in the Fig. 61 and Fig. 62) proved to be the best solution as it gave both a good view of the horizon for the pilot and sufficient view of the earth for reconnaissance. Screenshots from the camera's live images are shown in Figs. 63, 64 and 65.
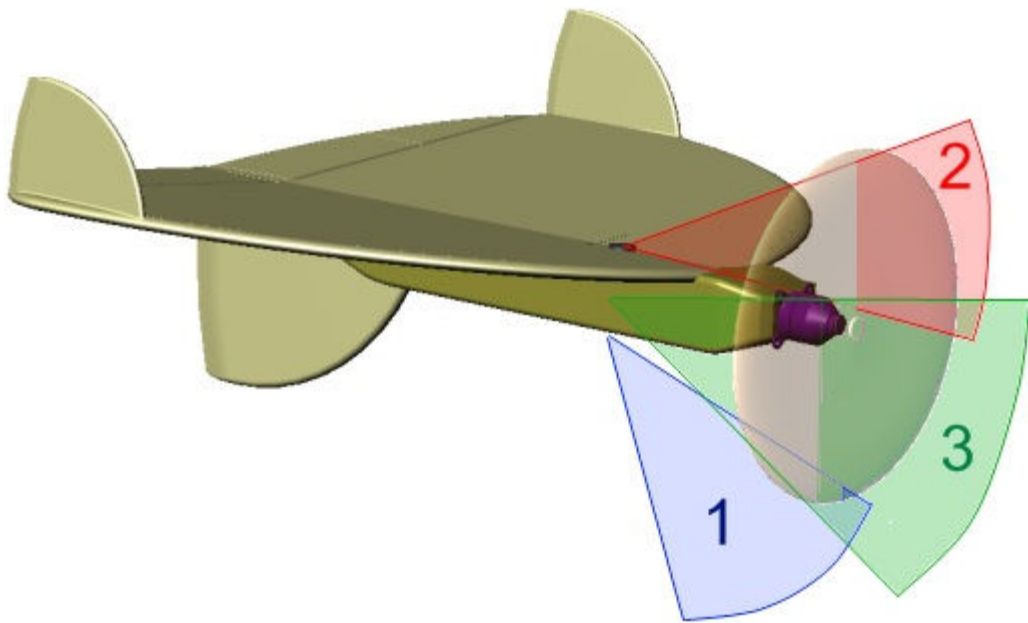
Figure 61 - Camera positions with marked forward fields of view. Belly-mounted, down-looking camera (1), top-mounted, forward looking camera (2) and side-mounted, forward looking camera which proved to be the best solution (3).
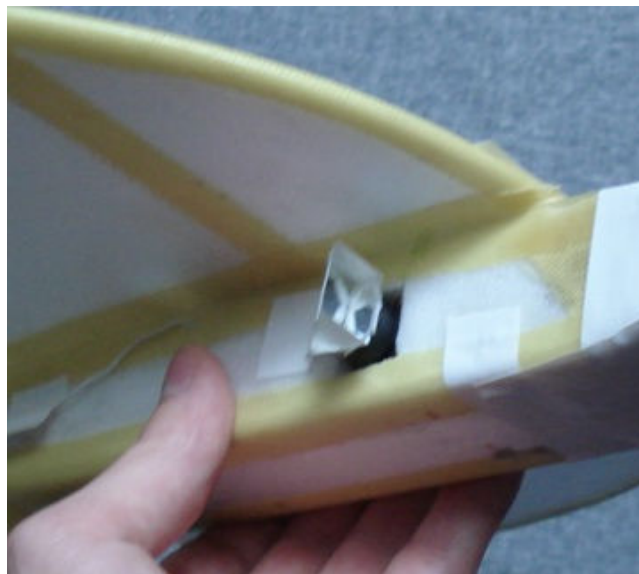
Figure 62 - Side-mounted forward-looking camera with prism installed on the MAV

Figure 63 - View from belly-mounted camera (1 in Figure 61)

Figure 64 - View from the camera mounted on top (2 in Figure 61)

Figure 65 - View from the side-mounted, forward-looking camera (3 in Figure 61)

The GPS system revealed some problems connected mainly with the software supplied with the receiver (VisualGPS[©]). Because of this, the author was able to record only a few flights. Rough estimation of the cruise speed has been carried out based on the GPS flight log (Fig. 66). Sample segments were chosen at which the MAV flew in opposite directions. The MAV was flying at roughly the same throttle setting throughout the whole flight so the average speeds at which MAV flew in opposite directions can be taken as an approximated V_c. Although this method provides only rough estimation, it is the best that could be extracted from the flight logs. The V_c was estimated to be 15.4m/s which is close to designed 16m/s. The maximum flight time logged during the test was 19 minutes. This is slightly less than the calculated endurance (23 minutes), mainly because of the extended video system antenna, camera prism and slightly larger fuselage cross-section, due to the extended additional battery. Nevertheless, the cruise speed and endurance are quite close to the initial design parameters, which prove that the design and optimization method is applicable to a real-life design case.
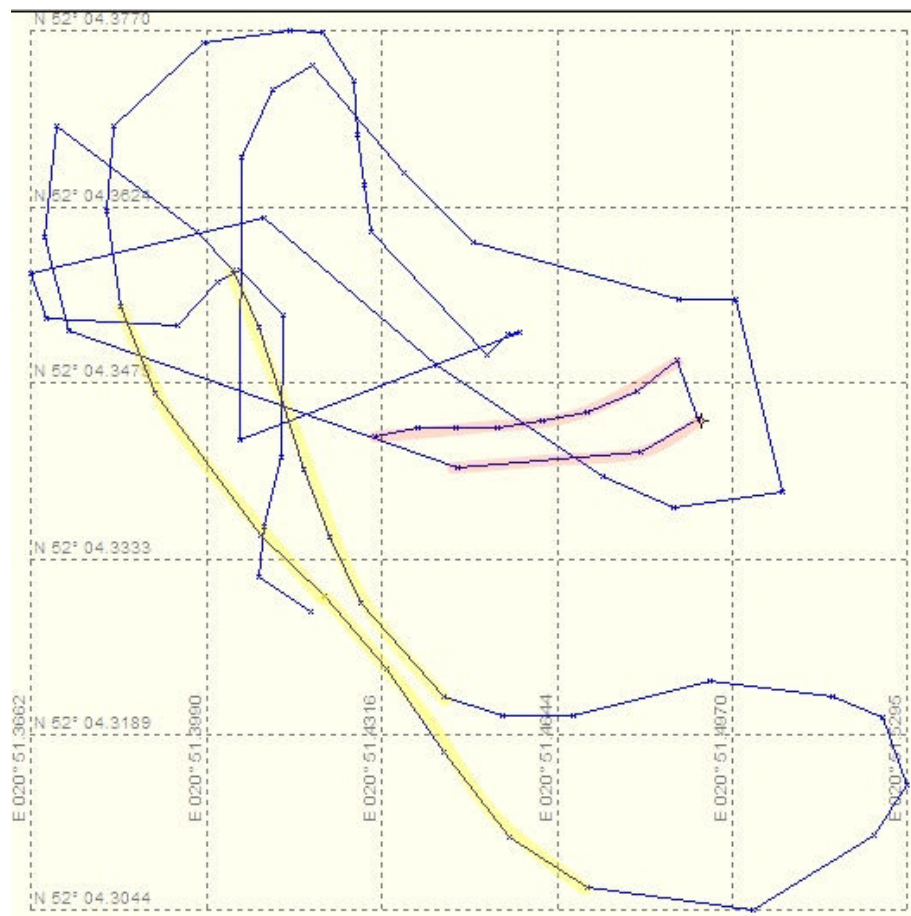

Figure 66 - Screen capture from the GPS flight log

8. Conclusions

The aim of the project was to develop and demonstrate a practical method of designing an MAV. Micro aircraft present a number of unique challenges such as aerodynamics and systems integration and thus require a different design approach from those applied to standard-sized aircraft. The aerodynamic theory used to predict performance of MAVs still needs to be investigated in greater detail as it does not allow the designer to predict the performance with sufficient accuracy in some cases. The wind tunnel tests, which were carried out as a part of the project, have shown sufficient agreement with the theory from [14, 15] and also provided valuable data on the drag contribution of the fuselage of the micro aircraft. The influence of the dihedral on the *L/D* of the MAV have also been investigated and analyzed. Special wing planforms tested in the wind tunnel proved to have rather poor performance (negative sweep) or to be rather complicated as a practical application (morphing wing). Nevertheless, the interesting stall characteristics of the latter (sections 4.10 and 4.11) might be worth investigating in the future. Some minor problems with the rig-model interaction which resulted in a pitching moment coefficient offset might also be investigated, although they were not essential in this study as only the $C_L(C_D)$ polars were used to validate the modeling of the aerodynamic characteristics.

The validation of the analytical performance calculations against the wind tunnel experiment results has shown that the Mueller and Torres method is by far the best method available for fixed wing MAVs designed in flying wing configuration. Slight differences at higher C_L values for all but the rectangular planforms were probably due to simplistic simulation of the Re effect on wing performance. The differences in the lift curve slope between the experiments and theory did not have any impact on the accurate simulation of the drag polars. Nevertheless this might be further investigated in order to provide a robust and experimentally-backed performance estimation method for MAVs.

The geometry optimization code developed for this project proved to work very well. Genetic Algorithms are well suited for this application. The implementation of

the performance calculation method with experimentally derived fuselage and fin drag polars also proved to work well and gave realistic, results which were later confirmed by the prototype test results. As some of the project details changed during the completion stages (need for a larger battery and a heavier camera system), the optimization code again proved its value, allowing for fast and easy redesign. Use of MotoCalc software helped with the propulsion performance estimation a great deal. While the propulsion system might have been modeled into the optimization code, in reality it would be very hard to obtain realistic results because of unknown detailed characteristics of various propellers which are used with these applications. Exact modeling of the electric motor would also be very difficult if it was to produce realistic results. Therefore, using cheap and widely available software helped to speed up and ease the whole design process. Extensive use of 3D CAD also contributed to the design process of both wind tunnel test rig and the prototype as well. The modeling of the BumbleBee in CAD allowed the investigation of the arrangement of the equipment inside the fuselage in detail and assured the proper position of the CG.

The GPS receiver with downlink allowed estimation of the performance of the MAV prototype. The cruise speed differed from the initial design and calculated values by less than 5%, which is considerable result. The endurance was also not far from the predictions although its calculation can be refined in the future, especially with more detailed fuselage and protuberance drag estimations. The flight properties and stability were excellent – as a result the flight stabilization system was not needed. Flights in 'pilot-through-vision' mode were carried out with no significant problems. A faster computer for processing the image and GPS data should be used in the future as it would allow for a higher quality video image. Although lacking the range of control, the prototype was a successful conclusion of the project. The problems with range are most probably due to the RC transmitter; in the future a different transmitter may be used if the budget allows.

This project has shown the feasibility of the presented design method. The rapid optimization of the MAV's geometry within given constraints has proven to be an extremely effective method of designing a micro-sized aircraft.

9. References

[1] Grasmeyer, J.M. - Keennon, M.T: *Development of the Black Widow Micro Air Vehicle,* AIAA-2001-0127

[2] Null, W., Shkarayev, S., "Effect of Camber on the Aerodynamics of Adaptive-Wing Micro Air Vehicles", *AIAA Journal of Aircraft,* Vol.42, No.6, November-December 2005

[3] Abdulrahim, M., Cocquyt, J. B., "Development of Mission-Capable Flexible-Wing Micro Air Vehicles", *53rd Southeastern Regional Student Conference* 4–5 April 2002 Huntsville, Alabama

[4] Galinski, C., "Gust Resistant Fixed Wing Micro Air Vehicle", *AIAA Journal of Aircraft,* Vol.43, No.5, September–October 2006

[5] Marek, P., Smrcek, L.; "Development of DART MAV - Fixed Wing Hover-Capable Micro Air Vehicle", *Advanced Engineering Design Conference*, Prague, Czech Republic, June 2006.

[6] MacRae, A.: *BEng Final Year Project Interim Report,* University of Glasgow, 2005.

[7] http://www.defense-update.com/products/t/TACMAV.htm

[8] Wilson, S.B.: *SBIR Success Story for DARPA Tech 2002AeroVironment Inc. Program Overview,* DarpaTech 2002 Symposium presentation

[9] Green, W.E. – Oh, P. Y.: *A MAV That Flies Like an Airplane and Hovers Like a Helicopter,* Proceedings of the 2005 IEEE/ASME International Conference on Advanced Intelligent Mechatronics, Monterey, California, USA, 24-28 July, 2005

[10] Bohorquez, F. et al. *Design, Analysis and Performance of a Rotary Wing MAV,* Smart Structures Laboratory, Alfred Gessow Rotorcraft Center, Department of Aerospace Engineering, University of Maryland

[11] MAV 07 – 3rd US-European Micro Air Vehicle Competition; www.mav07.org

[12] Watkins, S., et al., "Atmospheric Winds and Their Implications for Microair Vehicles", *AIAA Journal,* Vol.44, No.11, November2006

[13] Zimmerman, C.H., "Aerodynamic Characteristics of Several Airfoils of Low Aspect Ratio", *NACA Technical Note No. 539,* Washington, 1935.

[14] Torres, G.E., Mueller, T. J., "Low-Aspect-Ratio Wing Aerodynamics at Low Reynolds Numbers", *AIAA Journal*, Vol. 42, No. 5, 2004

[15] Mueller, T.J., "Fixed and Flapping Wing Aerodynamics for Micro Air Vehicle Applications", AIAA, Virginia, 2001, Chapters 1, 7.

[16] Alibre Design Xpress, freeware 3D parametric CAD software. www.alibre.com

[17] Jewel B. Barlow, William H. Rae, Jr., Alan Pope, "Low Speed Wind Tunnel Testing", New York, N.Y. Wiley, 1999, 3rd edition.

[18] http://www.mh-aerotools.de/airfoils/index.htm (visited 09.2006 -12.2007)

[19] http://engr.smu.edu/me/2142/uncert/uncert.htm (visited 09.2006 -12.2007)

[20] Kline, S. J., and F. A. McClintock: "Describing Uncertainties in Single-Sample Experiments", Mech. Eng., p. 3, January 1953

[21] T.T.H. Ng, G.S.B. Leng; "Application of genetic algorithms to conceptual design of a micro-air vehicle", Engineering Applications of Artificial Intelligence 15 (2002) 439-445.

[22] Rais-Rohani, M., Hicks, G.R., "Multidisciplinary design and prototype development of a micro air vehicle", AIAA Journal of Aircraft, 1999, 36(1) 227-234

[23] XFLR5 – freeware analysis tool for airfoils, wings and planes operating at low Reynolds Numbers. http://xflr5.sourceforge.net/xflr5.htm

[24] Luke, M., Bowman, W.J., "Predicting Drag Polars for fixed wing Micro Aerial Vehicles", AIAA 3rd Unmanned Unlimited" Technical Conference, Workshop and Exhibit, September 2004, Chicago, Illinois, AIAA 2004-6330

[25] Lundström, D., Krus, P., "Micro Aerial Vehicle design optimization using mixed discrete and continuous variables", 11th AIAA/ISSMO Multidisciplinary Analysis and Optimization Conference, 6 - 8 September 2006, Portsmouth, Virginia.

[26] Cosyn, P., Vierendeels, J., "Numerical Investigation of Low Aspect Ratio Wings at Low Reynolds Numbers", 23rd AIAA Applied Aerodynamics Conference, 6-9 June 2005, Toronto, Ontario, Canada

[27] Marek. P., "Design and wind tunnel testing of a Micro Air Vehicle", student introductory report, University of Glasgow 2007.

[28] Pelletier, A., Mueller, T. J., "Low Reynolds Number Aerodynamics of Low-Aspect-Ratio, Thin/Flat/Cambered-Plate Wings", AIAA Journal of Aircraft, Vol. 37, No. 5, 2000

[29] Cosyn, P., Vierendeels, J., "Design of a Fixed Wing Micro Air Vehicles", 20th Bristol UAV Systems Conference, April 2005

[30] Raymer, D., "Enhancing Aircraft Design Using Multidisciplinary Optimization", PhD Thesis, Royal Institute of Technology, 2002.

[31] http://www.tms.org/pubs/journals/JOM/0503/Thomas-0503.html (visited 12.2007)

[32] MotoCalc 8.05; Software for electric RC model performance calculation by Capable Computing Inc., 1996-2007; www.motocalc.com

[33] Neufeld, D. J., Chung, J., "Unmanned Aerial Vehicle Conceptual Design Using a Genetic Algorithm and Data Mining", Infotech@Aerospace, 26 - 29 September 2005, Arlington, Virginia

[34] Obayashi, S., "Multidisciplinary Design Optimization of Aircraft Wing Planform Based on Evolutionary Algorithms", Proceedings of the IEEE International Conference on Systems, Man, and Cybernetics, San Diego, CA, 1998.

[35] Hepperle, M. *A.C. Calculator*, freeware software for Aerodynamic Centre calculation; www.mh-aerotools.de

10. Bibliography

Raymer, D. P., "Aircraft Design: A Conceptual Approach", 2nd edition, AIAA, Washington, D.C., 1992.

Barlow, J. B., Rae, W. H., Pope, A.,"Low-speed wind tunnel testing", 3rd edition. Wiley, New York, 1999

Mueller, T.J., "Fixed and Flapping Wing Aerodynamics for Micro Air Vehicle Applications", AIAA, Virginia, 2001.

McCormick, B.W., "Aerodynamics, aeronautics and flight mechanics", 2nd edition, Wiley, New York, 1995.

11. Appendix

11.1 Optimization source code

- GA function:

```
function [x,FVAL,REASON,OUTPUT,POPULATION,SCORES] = mavga


%   |---------------------------|
%   |--- RUN GENETIC ALGORITHM ---|
%   |---------------------------|


prompt = {'enter min wingspan [mm]','enter max wingspan [mm]','enter min aspect ratio',...
    'enter max aspect ratio','enter component mass Mcomp in [g]','enter fuselage height in
[mm]',...
    'enter fuselage width in [mm]','enter max allowable stall speed [m/s]',...
    'enter design cruise speed [m/s]','enter lower limit for planform range',...
    'enter upper limit for planform range','enter population size'};
dlg_title = 'Input for MAV GA optimization';
num_lines = 1;
def = {'200','400','1','2','200','30','46','8','16','0','3.9999','250'};
C = inputdlg(prompt,dlg_title,num_lines,def);


lb1 = 0.001*str2double(C(1,1));
ub1 = 0.001*str2double(C(2,1));
lb2 = str2double(C(3,1));
ub2 = str2double(C(4,1));
Mcomp = 0.001*str2double(C(5,1));
fh = 0.001*str2double(C(6,1));
fw = 0.001*str2double(C(7,1));
Vstall = str2double(C(8,1));
Vcruise = str2double(C(9,1));
lb3 = str2double(C(10,1));
ub3 = str2double(C(11,1));
popsize = str2double(C(12,1));


%%Fitness function
fitnessFunction = @(x) my_fun5(x,Mcomp,Vcruise,Vstall,fh,fw)
nvars = 3;
%Linear inequality constraints
Aineq = [];
Bineq = [];
%Linear equality constraints
Aeq = [];
Beq = [];
%Bounds
LB = [lb1 lb2 lb3];
UB = [ub1 ub2 ub3];
```

```matlab
%Nonlinear constraints
nonlconFunction = [];
%Start with default options
options = gaoptimset;
%%Modify some parameters
options = gaoptimset(options,'PopulationSize' ,popsize);
options = gaoptimset(options,'StallTimeLimit' ,300);
options = gaoptimset(options,'MutationFcn' ,{ @mutationgaussian 1  1  });
options = gaoptimset(options,'Display' ,'off');
options = gaoptimset(options,'PlotFcns' ,{ @gaplotbestf @gaplotbestindiv });
%%Run GA
[x,FVAL,REASON,OUTPUT,POPULATION,SCORES]                              =
ga(fitnessFunction,nvars,Aineq,Bineq,Aeq,Beq,LB,UB,nonlconFunction,options);
%show final set of variables
x


%   |----------------------------------------|
%   |--- PERFORMANCE CALCULATION AND DISPLAY ---|
%   |----------------------------------------|


[z,V,CL,CD,LD,Treqg]=my_fun5(x,Mcomp,Vcruise,Vstall,fh,fw);


figure
subplot(2,2,1:2); plot(V,LD)
grid on
axis([0 40 0 8])
title('L/D(V)')
xlabel('V [m/s]')
ylabel('L/D')


subplot(2,2,3); plot(CD,CL)
grid on
title('CL(CD)')
xlabel('CD')
ylabel('CL')


subplot(2,2,4); plot(V,Treqg)
grid on
axis([0 40 0 200])
title('Treq(V)')
xlabel('V [m/s]')
ylabel('Treq [g]')


P = [V,CL,CD,LD,Treqg];
desc  = {'V  [m/s]','CL','CD','LD','Treg  [g]','b  [m]','AR','planform','Mcomp  [kg]','fh
[m]','fw [m]'};
para = [x(1),x(2),x(3),Mcomp,fh,fw];
xlswrite ('MAVmavga', P, 1, 'A2');
xlswrite ('MAVmavga', desc, 1, 'A1');
xlswrite ('MAVmavga', para, 1, 'F2');
end
```

- *Performance calculation function:*

```
function [z,V,CL,CD,LD,Treqg] = my_fun5(x,Mcomp,Vcruise,Vstall,fh,fw)
nvars = 3;     % Number of variables

%design variables - x(1)-wingspan (b), x(2)-aspect ratio (AR),
%x(3)-planform

%ALL VARIABLES MUST BE IN "SI" UNITS
% S - wing area
% c - root chord
% K - induced drag factor
% WS - wing loading
% Vcruise - design cruise speed [m/s]
% Vstall - max. allowed design Vstall [m/s]

Sfuse = fh*fw;
S = x(1)^2/x(2);

%K and CLmax curves as functions of Aspect Ratio (AR) taken from Torres &
%Mueller AIAA JA Vol.42 No. 5 May 2004

planform = fix(x(3));

if planform==0;
     disp('rectangular planform');
      c = S/x(1);
      mac = c;
    ARrng = 0.5:0.25:2;
    Krng = [0.668 0.563 0.532 0.484 0.421 0.405 0.379];
    CLmaxrng = [1.330 1.285 1.270 0.925 0.890 0.840 0.815];
    ARi = 0.5:.01:2;
    K = interp1(ARrng,Krng,x(2),'cubic');
    CLmax = interp1(ARrng, CLmaxrng, x(2), 'cubic');
    lvt = 0.65*c;

    elseif planform==1;
     disp('elliptical planform');
     c = 4*S/(pi()*x(1));
     mac = c*0.85;
    ARrng = 0.5:0.25:2;
    Krng = [0.668 0.563 0.558 0.463 0.421 0.384 0.379];
    CLmaxrng = [1.330 1.310 1.250 1.250 1.250 0.690 0.680];
    ARi = 0.5:.01:2;
    K = interp1(ARrng,Krng,x(2),'cubic');
    CLmax = interp1(ARrng, CLmaxrng, x(2), 'cubic');
    lvt = 0.61*c;

elseif planform==2;
     disp('Zimmerman planform');
```

```
    c = 4*S/(pi()*x(1));
    mac = c*0.85;
    ARrng = 0.5:0.25:2;
    Krng = [0.684 0.653 0.584 0.484 0.474 0.432 0.379];
    CLmaxrng = [1.280 1.200 1.225 1.230 1.230 0.750 0.720];
    ARi = 0.5:.01:2;
    K = interp1(ARrng,Krng,x(2),'cubic');
    CLmax = interp1(ARrng, CLmaxrng, x(2), 'cubic');
    lvt = 0.65*c;

elseif planform==3;
    disp('inverse Zimmerman planform');
    c = 4*S/(pi()*x(1));
    mac = c*0.85;
    ARrng = 0.5:0.25:2;
    Krng = [0.668 0.584 0.511 0.463 0.421 0.405 0.353];
    CLmaxrng = [1.270 1.325 1.270 1.140 0.860 0.740 0.690];
    ARi = 0.5:.01:2;
    K = interp1(ARrng,Krng,x(2),'cubic');
    CLmax = interp1(ARrng, CLmaxrng, x(2), 'cubic');
    lvt = 0.577*c;
end


%MAV weight calculation
%assumptions: fuselage length is equal to root chord. Airframe is made of
%foam of area-density "ad" in kg/m2. All the coefficients for weight
%multiplying are purely empirical. (DART MAV)

aw = 0.26;
Mwing = S*aw*1.5
Mfuse = (2*Sfuse + 2*fh*c + fw*c)*aw*2
M = Mcomp + Mfuse + Mwing
WS = 9.80665*M/S;

%vector with Cl range
CL = [0.01:0.005:CLmax]';

% rho - air density
% V for each CL:
rho = 1.225;
V = sqrt(2*WS./(rho*CL));

%Reynolds number based on root chord
%kinematic viscosity for ISA (15 deg C)
Re = mac*V./(1.47e-5);

%calculating parasite drag - based on XFoil results for flat plate
format long
Cd0 = 0.5268*Re.^-0.2982;
format
```

```matlab
%vertical tail - surface area Svt based on paper by Cosyn - Cvt (vertical
%tail volume coefficient for MAVs should be in the range of 0.05 to 0.06
%Assumption that the vertical stabilizer is ~square is used to determine
%it's CDvt0
%lvt is calculated as the ACvt is located at 10%c in front of the the
%trailing edge of the wing
Svt = 0.06*mac*S/lvt

%cvt - vertical tail chord
cvt = sqrt(Svt);
Revt = cvt*V./(1.47e-5);
Cdvt = 0.5268*Revt.^-0.2982;

%CD=Cd0 (parasite drag) + KCL^2 (induced drag) + Cdfuse (fuselage drag)
CD = Cd0+K*CL.^2+(-0.6617*CL+0.4618)*(Sfuse/S)+Cdvt*Svt/S;

%LD - lift to drag ratio (L/D)
%LDmax - maximum L/D of current MAV
LD = CL./CD;

%indx multiplier must be the same as step in CL vector (line ~81)
[LDmax,indx] = max(LD);
LDmax
CLopt = indx*0.005;

%Vopt - optimum airspeed (@CLopt thus @best L/D)(do not confuse with Vcruise
%which is design cruise speed)
%Vmin - minimum (stall) airspeed at CLmax (do not cofuse with Vstall which
%is design max allowable stall speed)
Vopt = sqrt(2*WS/(CLopt*rho))
Vmin = sqrt(2*WS/(CLmax*rho))

%Treq - thrust required for level flight
Treq = 0.5*rho.*V.^2.*CD*S;
Treqg = Treq./9.81*1000;

%stall penalty
if Vmin>Vstall;
    stall_cond = Vmin-Vstall;
else
    stall_cond = 0;
end

%fitness function
z = -LDmax + 0.5*abs(Vcruise-Vopt) + stall_cond^2;

end
```
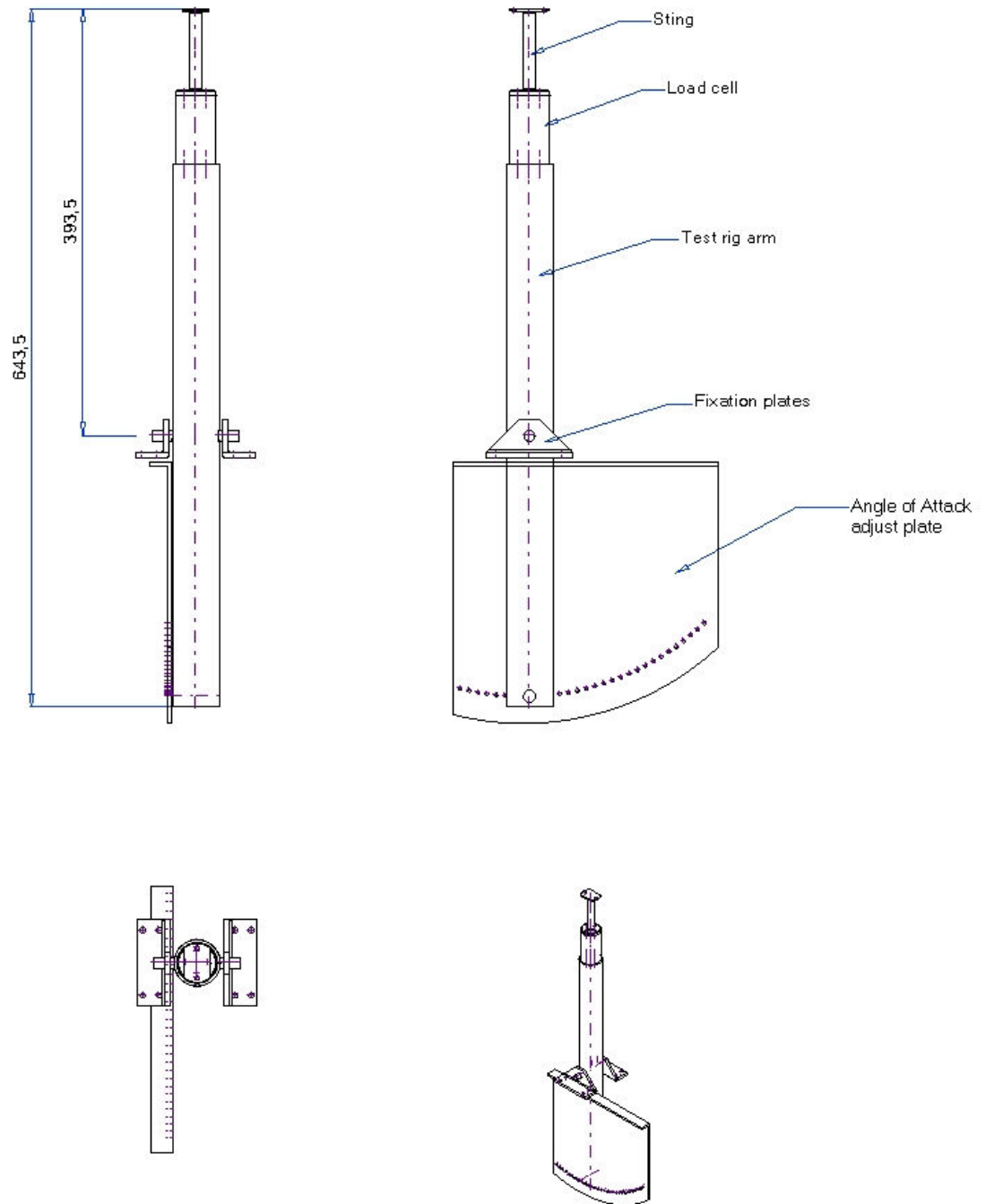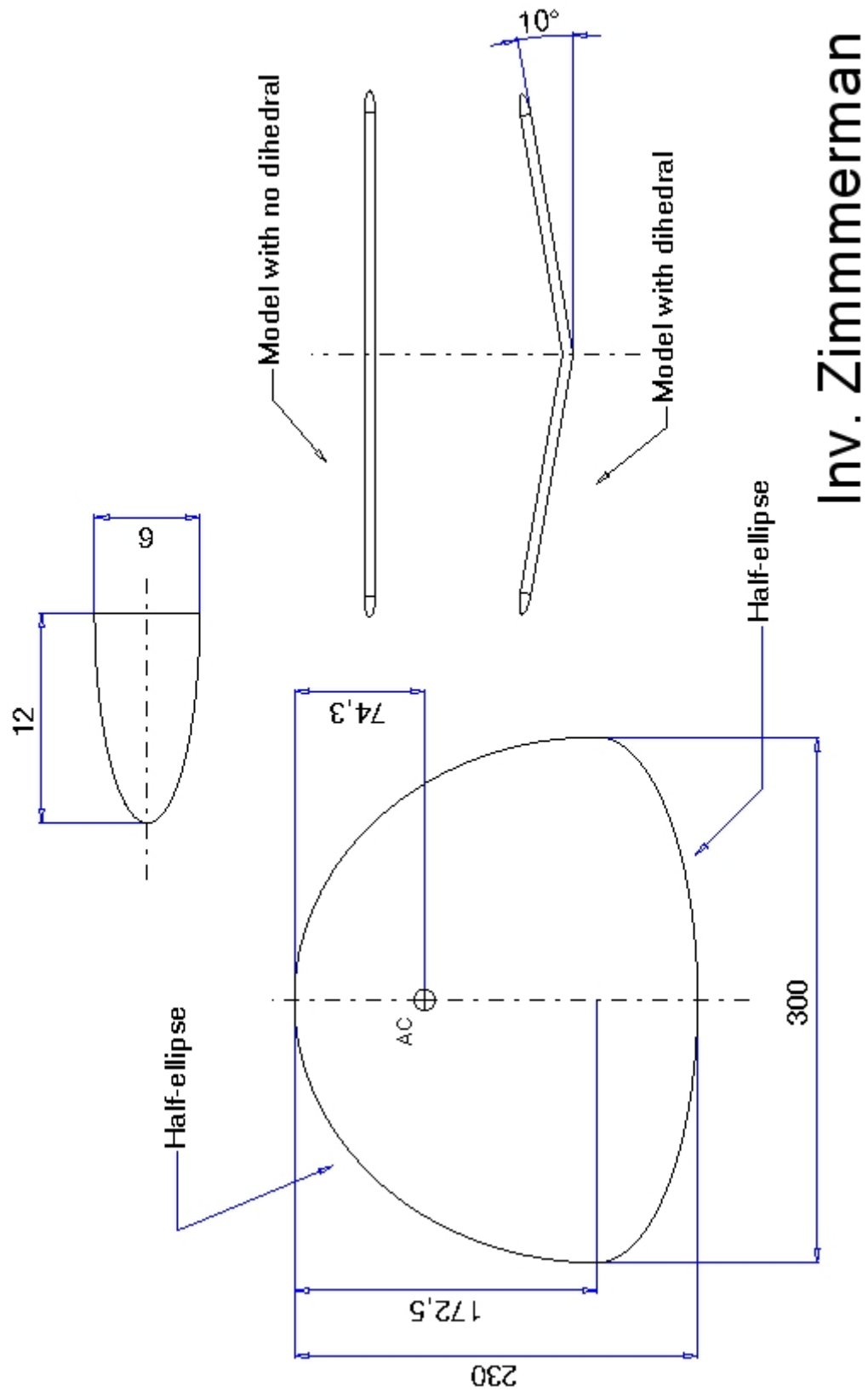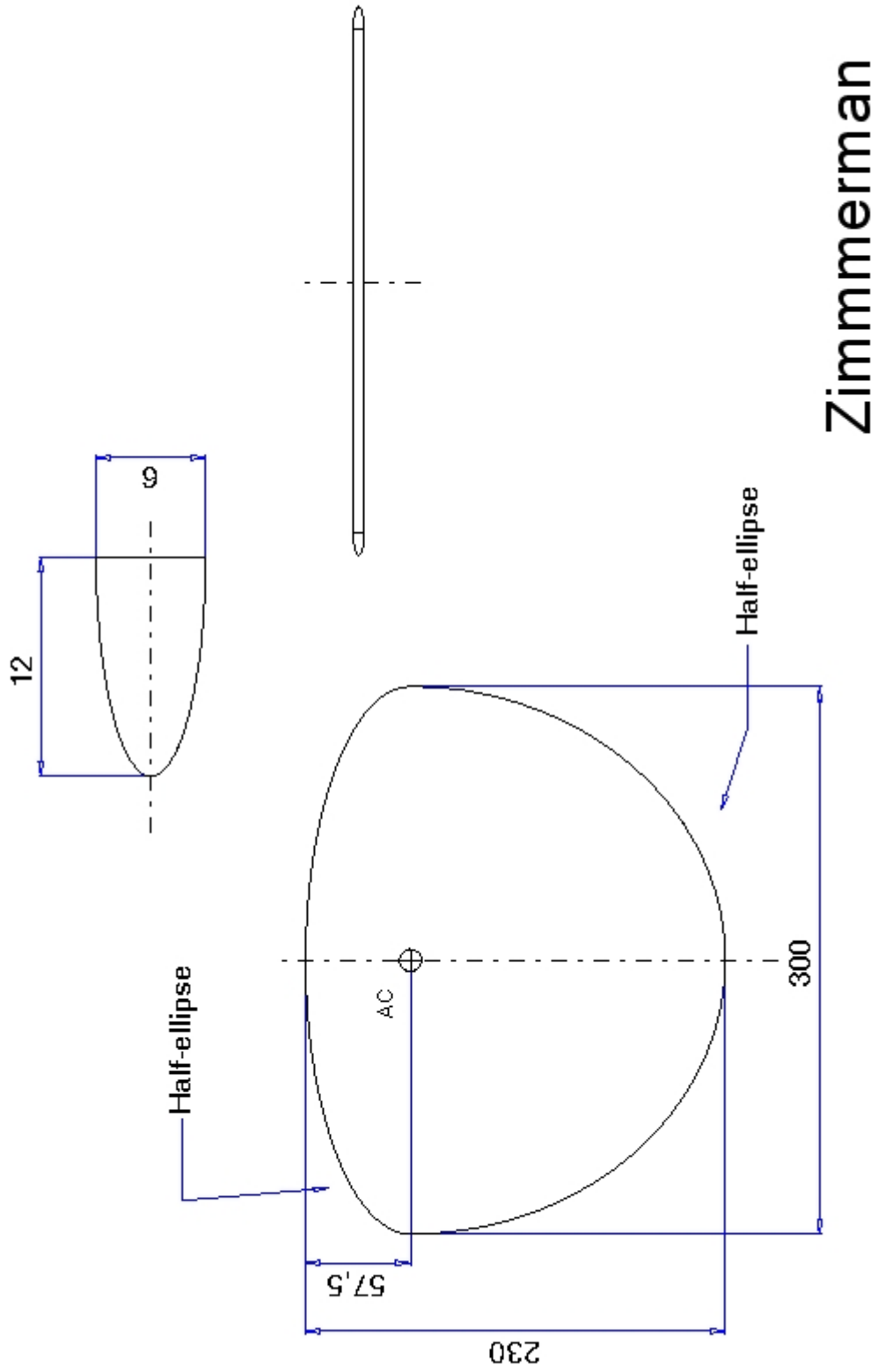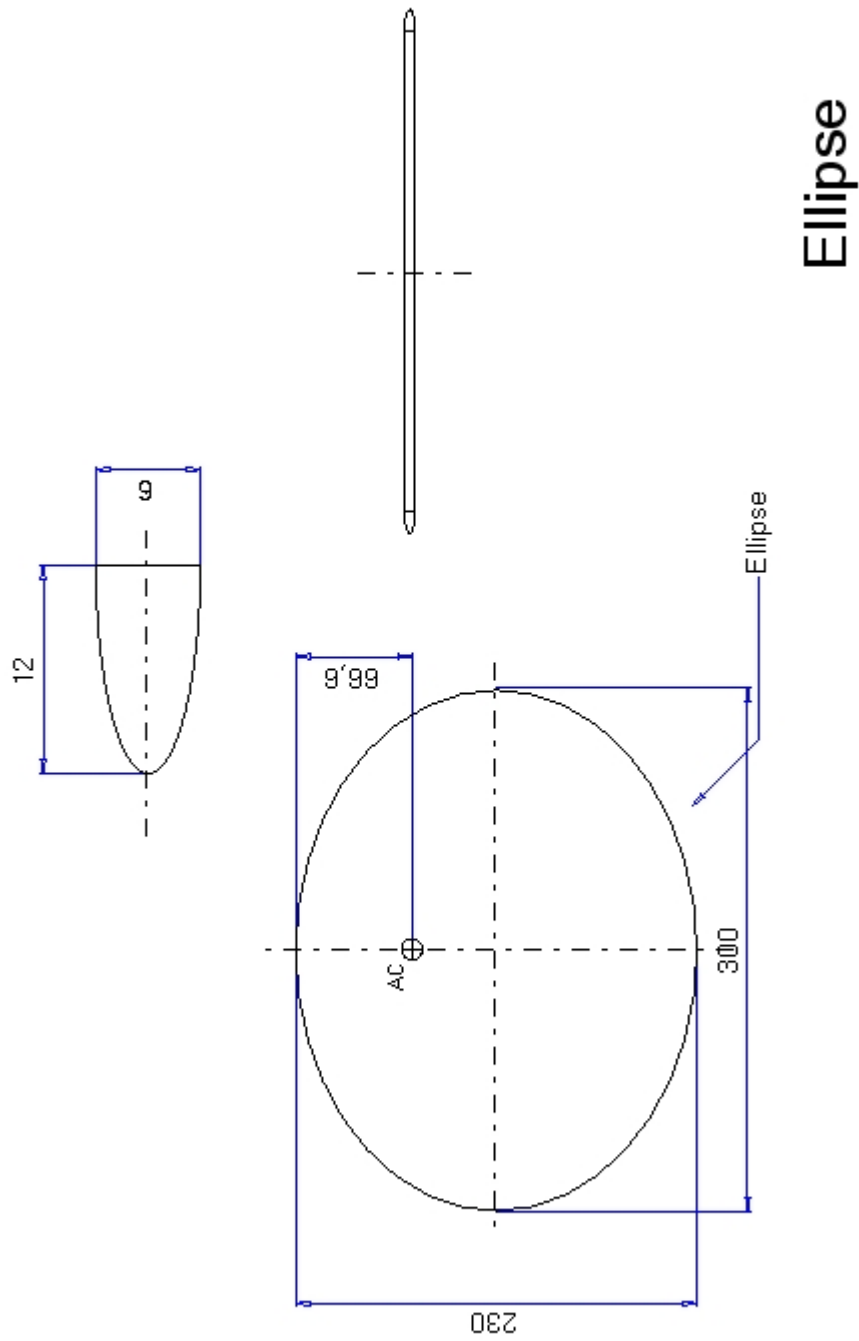
11.2 Prototype 3-view drawing
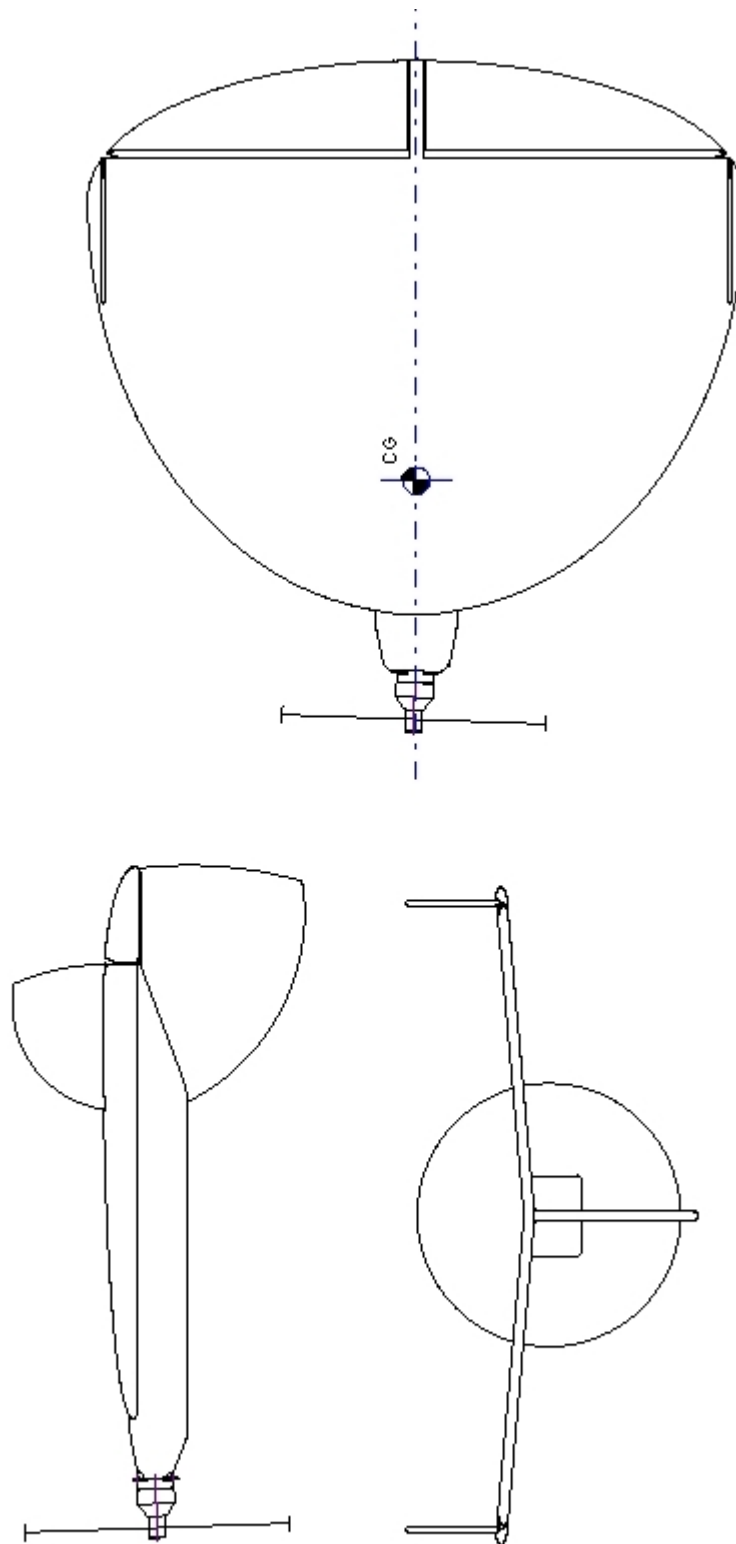
11.3 Test rig drawing

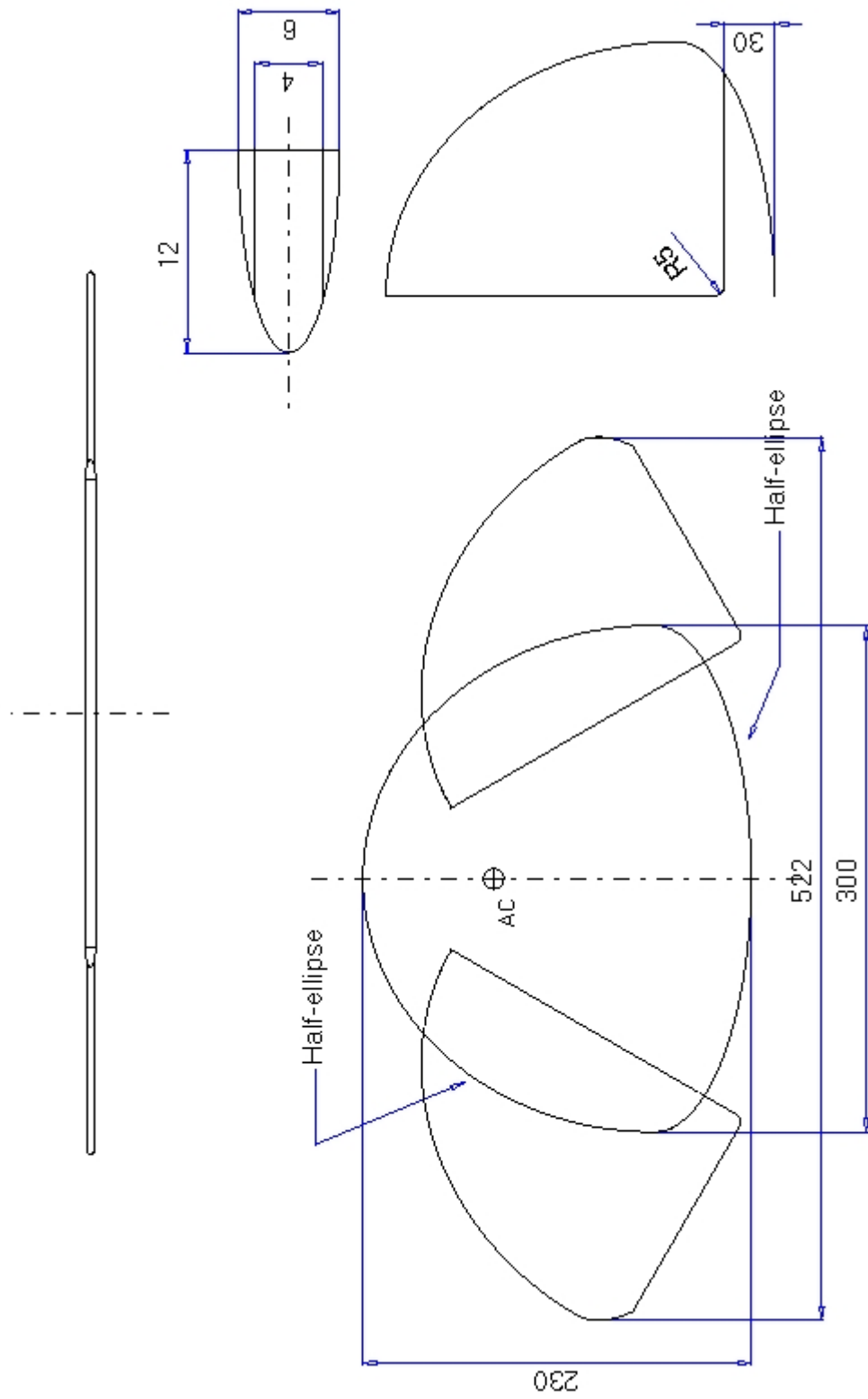## 11.4 Wind tunnel model drawings

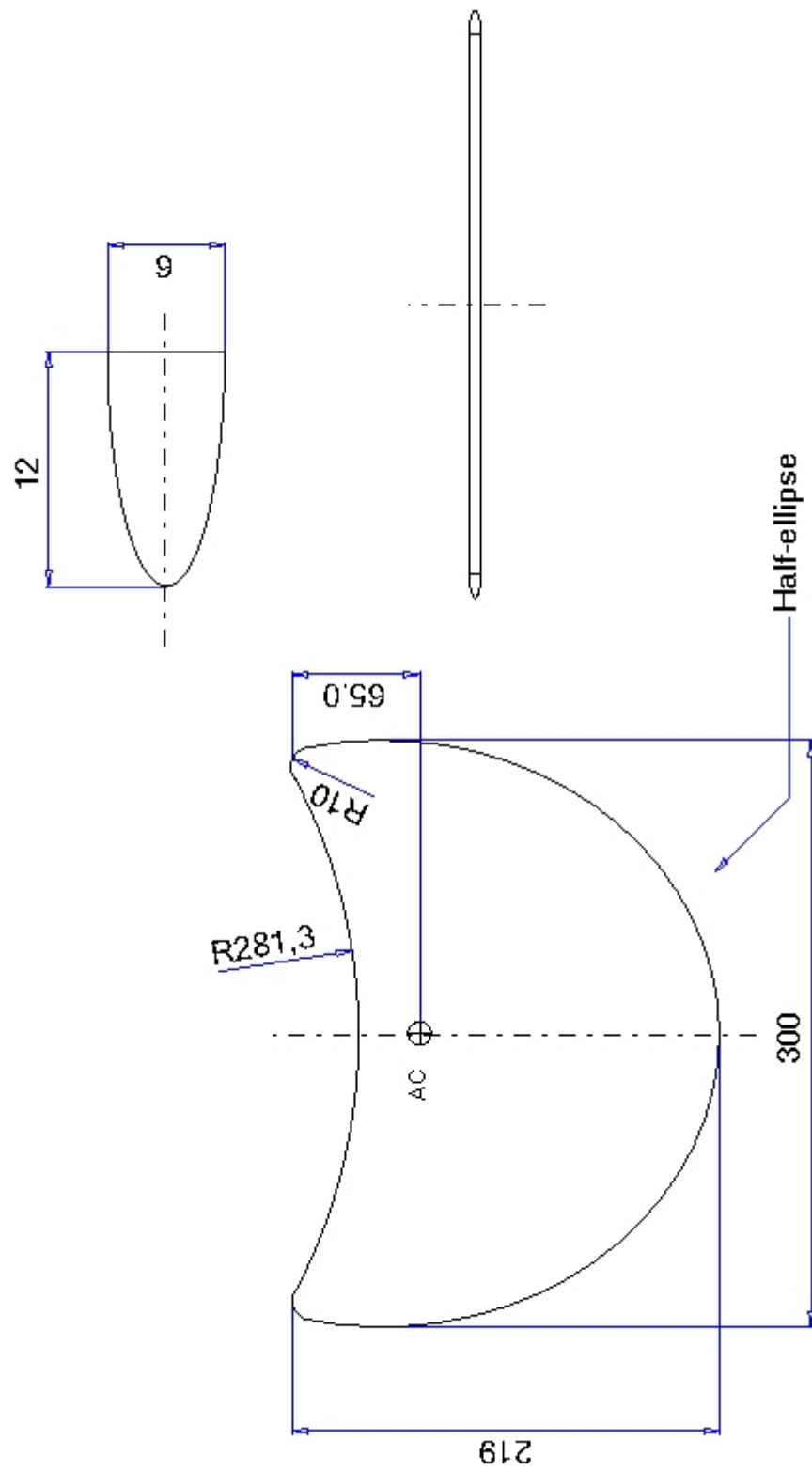Zimmmerman

Ellipse

Morphing

Neg. Sweep

Rectangular

9

12

57,5

AC

300

230

Fuselage 1

Fuselage 2